

LONG WAVELENGTH ASTROPHYSICS

by

Liam Dean Connor

A thesis submitted in conformity with the requirements
for the degree of Doctor of Philosophy
Graduate Department of Astronomy and Astrophysics
University of Toronto

© Copyright 2016 by Liam Dean Connor

Abstract

Long wavelength astrophysics

Liam Dean Connor

Doctor of Philosophy

Graduate Department of Astronomy and Astrophysics

University of Toronto

2016

Acknowledgements

The research presented in this thesis sample the work I have done over the last five years, which has ranged from what felt like mathematical musings to software development to on-site hardware work. This is because both of my supervisors, Ue-Li Pen and Keith Vanderlinde, possess end-to-end expertise, with firm understanding of the physics in which we are interested as well as the steps required to make such measurements come to fruition; needless to say this thesis would not have been possible without them. A similarly insightful supervisory figure was Richard Shaw, whose ease with signal processing, statistics, and computing was greatly appreciated in my first few years of graduate school.

On the CHIME team, I was lucky enough to work closely with such world-class experimental cosmologists as Mark Halpern and Gary Hinshaw. Tom Landecker was an irreplaceable source of knowledge and wisdom during my many visits to DRAO, acting as the token radio astronomer in a large radio astronomy project. I would also thank my thesis committee, including Barth Netterfield and Mike Reid.

Contents

1	The Canadian Hydrogen Intensity Mapping Experiment	1
1.1	Chapter Overview	1
1.2	Introduction	2
1.3	CHIME Science	2
1.3.1	21 cm Cosmology	2
1.3.2	Pulsar	7
1.3.3	FRB Survey	8
1.4	Instrument	11
1.4.1	Clover-feeds	12
1.4.2	Amplifiers	13
1.4.3	Correlator	14
1.4.4	Beams	15
1.5	Conclusion	18
2	Beamforming	19
2.1	Chapter Overview	19
2.2	Introduction	20
2.3	Theory and Implementation	20
2.3.1	Geometric phase	21
2.4	Pathfinder beamformer	24

2.4.1	Instrumental phases	24
2.4.2	First coherent light	28
2.5	FRB VLBI search	32
2.5.1	Motivation	32
2.5.2	Implementation	33
2.5.3	ARO FRB search	34
2.5.4	Results	34
2.5.5	False positives	35
2.6	Conclusion	36
3	Non-cosmological but Extragalactic Fast Radio Bursts	39
3.1	Chapter Overview	39
3.2	Introduction	39
3.3	Introduction	39
3.4	Supernova Remants	41
3.4.1	Event Rates	42
3.4.2	Young SNR Pulsars	45
3.5	Predictions	47
3.6	Conclusions	51
3.7	Acknowledgements	52
4	Fast Radio Burst Statistics	53
4.1	Chapter Overview	53
4.2	Introduction	55
4.3	Rethinking the constraints on repetition	55
4.3.1	Flicker noise	56
4.3.2	FRBs 110220 and 140514	58
4.3.3	Repetition and total number of sources	60

4.4	FRB 110523 and sub-L-band statistics	61
4.4.1	Implications for the flux distribution	63
4.4.2	How to discuss event rate	64
4.4.3	Burst rate	64
4.4.4	Implications for other surveys	66
4.4.5	All-sky daily rate	69
4.5	Latitudinal dependence	72
4.6	Is the distribution Euclidean?	75
4.7	Methodology	76
4.7.1	Likelihood for the observed signal-to-noise ratios	76
4.7.2	Likelihood for the number of observed FRBs	77
4.7.3	Posterior	79
4.8	Data and results	80
4.9	Conclusions	81
4.10	Conclusions	84
5	Pulse Microstructure	86
5.1	Chapter Overview	86
5.2	Introduction	86
5.3	Theory and Implementation	87
5.4	B0329+54 Individual Pulses	87
5.4.1	Observations	87
5.4.2	Data analysis	87
5.4.3	First coherent light	87
5.5	FRB VLBI search	90
5.5.1	Motivation	92
5.5.2	Implementation	92
5.5.3	Results	93

5.6 Conclusion	94
6 Conclusions and Outlook	96
Bibliography	97

List of Tables

1.1 CHIME Parameters	11
--------------------------------	----

3.1	This table summarizes a number of FRB models by classifying them as cosmological, extragalactic but non-cosmological, Galactic, and terrestrial. The seven columns are potential observables of FRBs and each row gives their consequence for a given model (Blitzars (Falcke & Rezzolla, 2014), compact object mergers (Mickaliger et al., 2012; Totani, 2013), exploding primordial blackholes (Barrau et al., 2014), bursts from magnetars (Lyubarsky, 2014), edge-on disk galaxies (Xu & Han, 2015), circumnuclear magnetars (Pen & Connor, 2015a), supernova remnant pulsars, stellar flares (Loeb et al., 2014), and terrestrial RFI (Hippke et al., 2015).). For the latter, we subdivide the RFI into planar RFI (2D) coming from the earth’s surface, and 3D RFI coming from objects like satellites. Since scintillation only affects unresolved images, cosmological sources that are not scattered near the source will not scintillate in our Galaxy, while non-cosmological sources whose screens are intrinsic will. For Faraday rotation and scintillation we assume the RM and SM comes from the same place as the DM, e.g. the IGM for cosmological sources, though such models could introduce a more local Faraday effect or a scattering screen. Even though all models have to explain the observed $375\text{--}1600 \text{ pc cm}^{-3}$, some models predict a wider range of DM. For instance, in the circumnuclear magnetar or edge-on disk disk scenarios there ought to be bursts at relatively low DM that simply have not been identified as FRBs. In our supernova remnant model DMs should be very large early in the pulsar’s life, though this window is short and therefore such high DM bursts would be rare. . .	46
4.1	Parameters assumed for the FRB surveys. See Sect. 4.7.2 for the meaning of the symbols.	81
4.2	Parameters of each individual FRB used in our calculation. The signal-to-noise ratios s are taken from the FRBcat website ¹ (Petroff et al., 2016).	82

Chapter 1

The Canadian Hydrogen Intensity Mapping Experiment

1.1 Chapter Overview

In this chapter we will introduce in detail the Canadian Hydrogen Intensity Mapping Experiment (CHIME). We will discuss the experiment for which it was originally built, namely CHIME cosmology and the attempt at mapping out the Universe’s hydrogen in order to do large-scale structure (LSS) and learn about dark energy. The science goals of the time-variable back-ends will then be introduced, with an emphasis on CHIME FRB, whose objectives are most relevant to this thesis. Finally, we will describe the instrumentation that unifies these three projects. We will discuss the early data analysis and instrumental characterization of the Pathfinder, including the pervasiveness of a standing-wave between our reflector and the focal line, and the mis-pointing of our beams due to a $\sim 2^\circ$ azimuthal rotation of our cylinders.

1.2 Introduction

CHIME is a Canadian collaboration between the University of British Columbia (UBC), the University of Toronto (UofT), McGill University, and the Dominion Radio Astrophysical Observatory (DRAO). Located at DRAO — Canada’s national radio observatory seen in Fig. 1.2 on page 5 — CHIME consists of two stages: A pathfinder instrument, known hereon as the CHIME Pathfinder, which is two 20x37 m cylinders and is shown in Fig. 1.2; and the final instrument, called either full CHIME or just CHIME, and is four 20x100 m cylinders. The Pathfinder was first “on sky” in November 2013, however it has only been observing in full capacity, i.e., with all of its feeds mounted and drawing power, since 2015. As of late spring 2016, full CHIME’s structure exists and is meant to be instrumented before the end of 2016. It can be seen in Fig. 1.2.

CHIME’s primary science goal is to measure the Universe’s neutral hydrogen between redshifts 0.8-2.5, mapping out the large-scale structure (LSS) and constraining dark energy’s equation of state. However, it was noticed early on that CHIME could be a powerful tool for studying the time-variable sky. Fortunately, digital radio telescopes like CHIME can run multiple experiments in parallel, since data can be siphoned off and split between different back-ends. In light of this an effort was made, successfully, to acquire funding for two new experiments to piggy-back on CHIME. One is a pulsar back-end that will monitor large numbers of sources each day, observing up to 10 pulsars at a time, 24/7. Another is an FRB back-end that will search 1024 FFT-formed beams for dispersed transients.

1.3 CHIME Science

1.3.1 21 cm Cosmology

Historically, constraining the nature of dark energy has been expensive in time and resources. Probably the most promising method has been to map out the Universe’s



Figure 1.1: Photograph of the CHIME Pathfinder, constructed in 2013. The Pathfinder was built as a testbed for analysis and instrument design, largely because CHIME is attempting a very difficult measurement that requires an unprecedented understanding of our telescope. In attempting a new technique (21 cm intensity mapping) with an unorthodox telescope design we were guaranteed to not get it perfect the first time, hence the smaller precursor instrument to “find the path”. After two years of taking data in multiple configurations, we have learned a number of lessons about calibration, cross talk, our beams, and the correlator. We also ran into unforeseen obstacles, including a mis-pointing caused by ambiguity in the definition of “north”, the pervasive effects of a standing wave between the reflector’s vertex and our focal line, and the impact of surface perturbations in the cylinders’ mesh.

matter at large scales and at many different redshifts, and measure its expansion with the baryon acoustic oscillations (BAO) (Eisenstein et al., 2005; Seo & Eisenstein, 2003). Traditional spectroscopic galaxy surveys require resolving scales (of galaxies, specifically, \sim 10s of kpc) that are much smaller than the LSS, in particular the BAO, which is hundreds of Mpc. A far more economic, albeit uncharted, approach is to map out 21 cm emission from hydrogen that traces the underlying dark matter distribution (Battye



Figure 1.2: Full CHIME shortly after the construction of the fourth and final parabolic cylinder in fall 2015. Each dish is 20 m in the east-west direction and 100 m long. Unlike the Pathfinder, the cylinders are aligned with the *celestial* North Pole and should have true declination beams. There was also great care taken creating a smooth surface, since the Pathfinder’s relatively large surface RMS lead to issues with its beams.

et al., 2004; Peterson et al., 2006). This technique was proposed as a cheaper and more efficient alternative to galaxy surveys for probing dark energy, and it was given the name “intensity mapping” (Chang et al., 2008). Since one is concerned only with \sim degree angular scales, the collective emission from thousands of galaxies can be used as a proxy for the Universe’s LSS, as it is a biased tracer of the dark matter. 21 cm cosmology therefore opens up access to a huge number of cosmological modes and is in line to take the baton from the CMB as our greatest source of cosmological information (Furlanetto et al., 2006; Morales & Wyithe, 2010; Tegmark & Zaldarriaga, 2009).

In principle intensity mapping gives us access to large volumes of the Universe, and therefore cosmic variance limited constraints on dark energy’s equation of state parameter w . However, like many high-reward, low economic-cost techniques, doing LSS with 21 cm

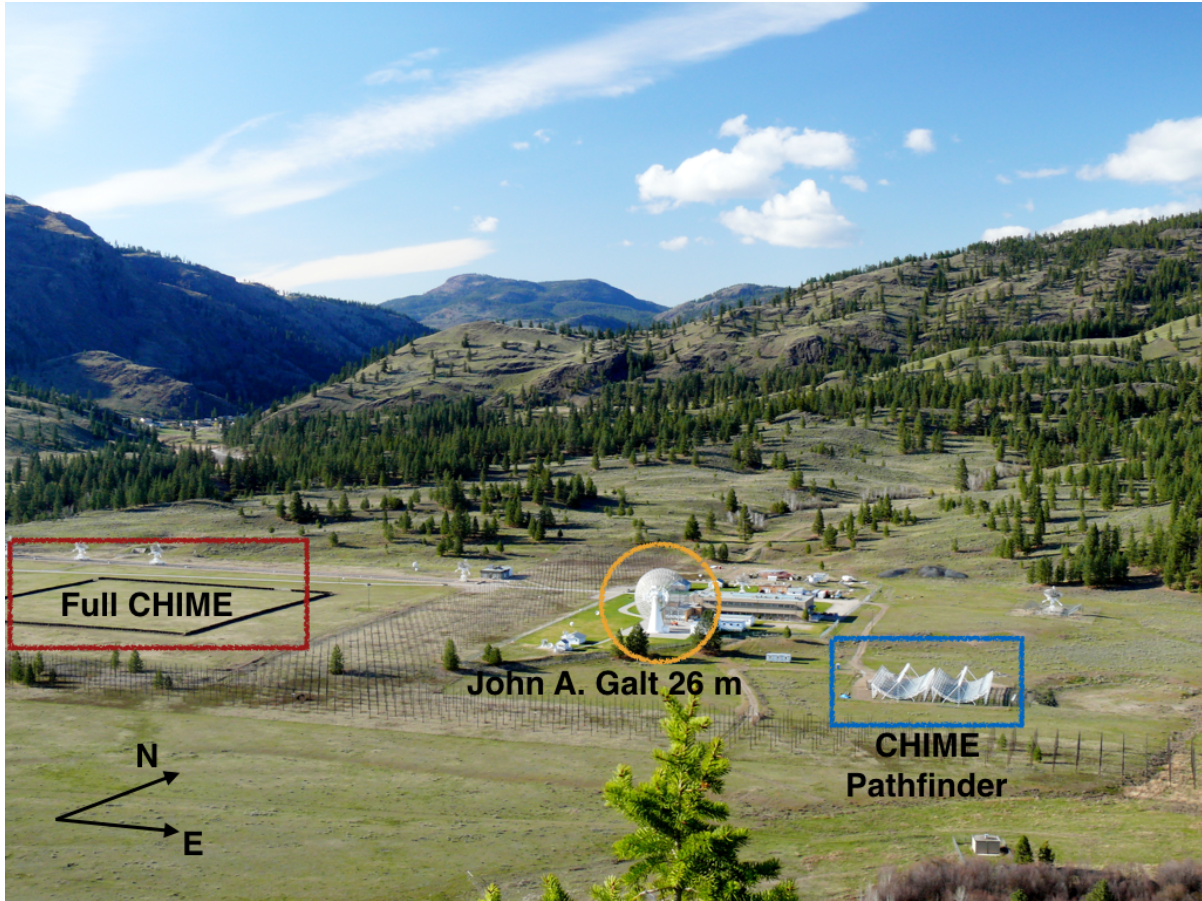


Figure 1.3: The Dominion Radio Astrophysical Observatory (DRAO) in Penticton, British Columbia. The site hosts three dishes relevant to CHIME. One is the CHIME Pathfinder, seen in the bottom right (east-most corner) of this image. Another is the John A. Galt 26 m telescope, which is a steerable equatorial telescope that is used for holographic beam mapping of both full CHIME and its pathfinder. Finally, the site of the full four-cylinder instrument, which was not constructed at the time of this photograph but is now in the west-most field.

mapping comes with a number of systematics. Terrestrial radio frequency interference (RFI) is ubiquitous, meaning long-wavelength measurements will always be contaminated by human communication in the radio. But fundamentally, intensity mapping is difficult because the redshifted HI emission that contains the cosmological information is faint. After cosmic reionization, neutral hydrogen is confined to galaxies and has a brightness

temperature of just a few hundred μK (Chang et al., 2010). Radio foregrounds below 1.4 GHz can be 10^3 - 10^5 times brighter than this cosmological 21 cm signal (Furlanetto et al., 2006; Morales & Wyithe, 2010). They include Galactic synchrotron, extragalactic point-sources, and to some extent, bremsstrahlung.

The signal of interest must therefore be extracted from underneath the loud foregrounds. This would be impossible if it were not for the spectral nature of these foregrounds: Since synchrotron radiation is the sum of a continuous distribution of large numbers of relativistic electrons with different energies, the resulting spectra are smooth and well-characterized by a power-law (Rybicki & Lightman, 1979). On the other hand, 21 cm emission is not spectrally smooth since each frequency corresponds to a different redshift and therefore a different patch of neutral hydrogen along the line of site. One can take advantage of this difference by separating the smooth and rough frequency components of the signal, and there have been numerous attempts at doing this effectively (Parsons & Backer, 2009; Wang et al., 2006; Liu & Tegmark, 2011; Shaw et al., 2015, 2014).

Shaw et al. (2015, 2014) developed a statistically optimal method known as the “m-mode formalism” for foreground removal and map-making in the presence of beam uncertainties and polarization leakage. Though it was developed with CHIME in mind, it can applied to any transit interferometer. It was found by Shaw et al. (2015) that one caveat of this method is that one’s telescope must be characterized with an unprecedented level of precision. Complex gains must be tracked with regular cadence, and one must know one’s full-polarization beams very well. In Sect. 1.4.4 we detail our attempts at this characterization on the Pathfinder.

Once CHIME is calibrated at the level where foregrounds can be removed, it will go after the redshifted 21 cm emission between $z = 0.8$ - 2.5 , corresponding to a band of 400-800 MHz. CHIME is constructed to measure angular scales on the sky that best constrain the matter power spectrum at modes corresponding to the BAO. The BAO’s

first peak appears at $1.35\text{-}3^\circ$ for redshifts 0.8-2.5. The smallest scales that need to be detected are set by the third peak. In the transverse direction on the sky, this sets our array's physical size of ~ 100 m. In the radial direction, this sets our frequency resolution. The Pathfinder is projected to be able to do interesting cosmology, though it will have to do so with only the first BAO peak due in the transverse direction because of its limited spatial resolution. These parameters are shown in Table 1.4.

1.3.2 Pulsar

CHIME's collecting area and wide bandwidth make it a highly sensitive telescope for pulsar astronomy. On top of this, its ability to record data 24 hours a day, 365 days a year, allow for pulsar monitoring that cannot be done elsewhere. Although the existing analog chain can be used for pulsar astrophysics, the required time-domain signal processing is such that a new digital back-end must be built. This will include, for example, a maser for precision timing a separate GPU cluster for brute-force beamforming and real-time pulsar processing like coherent dedispersion and folding.

Full CHIME will have the sensitivity to see every known pulsar in the northern hemisphere, every single day. This is shown in Fig. 1.3.2. The access to any pulsar for 10-15 minutes each day will enable CHIME to do a range of new astrophysics. Perhaps the most promising avenue the back-end is the potential to do long-term timing of millisecond pulsars. Pulsar timing can detect or provide interesting new limits on a window of gravitational waves that cannot be probed by experiments like LIGO. It will be included in the NANOGrav consortium and will be able to monitor the daily changes in dispersion measure, which is a significant source of error in pulsar timing arrays.

Beyond timing, CHIME will be able to go after any pulsar variation science that takes places on timescales greater than a day, and shorter than ~ 10 minutes. It could carry out scintillation studies, Faraday rotation measure monitoring, and pulsar searching.

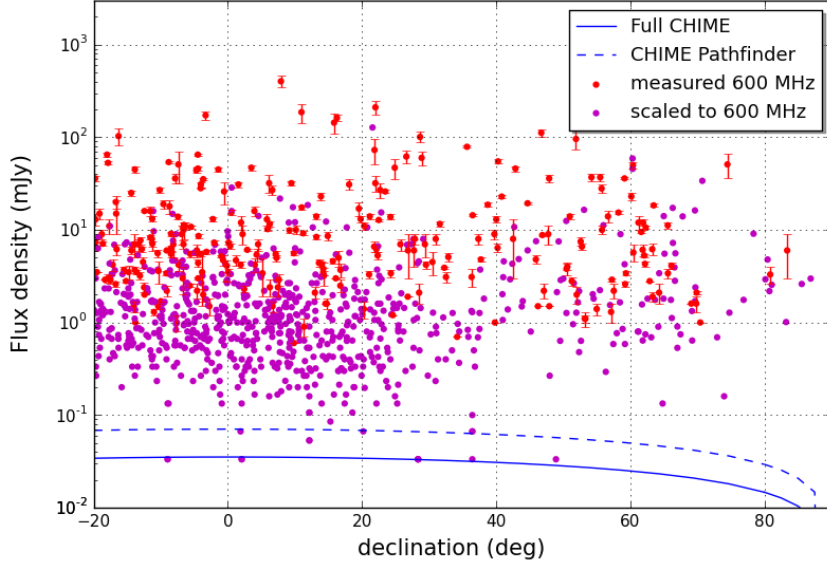


Figure 1.4: Daily sensitivity of CHIME and the Pathfinder for all known pulsars above declination of -20° . The red points have been measured directly in the middle of our band, and the magenta dots are extrapolated from other frequencies.

1.3.3 FRB Survey

The origin of fast radio bursts is presently one of the greatest mysteries in the radio sky. Although we have known about them for nearly a decade, fewer than two dozen have been discovered. CHIME, with its $\sim 100 \text{ deg}^2$ FoV could potentially detect this many in its first week on sky. That is because CHIME’s evenly spaced feeds enable us to spatially FFT the array in order to form fan-beams that populate its entire primary beam. This basic idea can be found in (Peterson et al., 2006) and was given the title “Fast Fourier Transform Telescope” in (Tegmark & Zaldarriaga, 2009). By taking advantage of a regularly gridded array, the $N \log N$ scaling of FFTs can be exploited. All N independent beams can then be searched for dispersed radio transients as long as the search is done quickly. For this, a tree-dedispersion algorithm was developed (after being rediscovered — see (Taylor, 1974)) that scales as $XX \log XX$. An example of this is shown in Fig. 1.3.3 in which the top map shows the response on the sky of a single dipole on the focal line, and the bottom map shows the result of FFT-beamforming. The beam was simulated by taking

the simple dipole beam from (Shaw et al., 2015) and propagating it onto the sky by solving the Fraunhofer diffraction problem.

Just like the cosmology and pulsar back-ends, the FRB survey will be on sky at all times. It will form 1024 Stokes I beams, excise RFI, and search a multi-parameter space in real-time for bursts. The search space includes DM, arrival time, spectral index, width, and a scattering measure. Triggers will then be stored at \sim millisecond cadence with the option of storing baseband, allowing for polarization studies and high time resolution information.

Given its large FoV and substantial collecting area, CHIME is expected to see more FRBs than any other survey. In chapter 4 we forecast the speed of CHIME FRB and find its rate to be,

$$N_{\text{CH}} \approx 7.5 \left(\frac{50 \text{ K}}{T^{\text{sys}}} \right)^{1.5} \text{ day}^{-1}, \quad (1.1)$$

with a 95% confidence interval of 2-40 per day. This means 10^{3-4} after just one year. With such a large collection of events one could do population statistics on their $N(S)$ distribution, DM statistics, scattering properties, etc. Having \sim 20-arcminute localization for hundreds or thousands of bursts could also be used to correlate with the large-scale structure. Polarization could also be an important feature, which CHIME will have the option to study. For example, one might find significant Faraday rotation is a generic property of FRBs. Large rotation measure (RM) is not explicable by the IGM alone, so the distribution of RMs could tell us about the magnetized environment near the source.

1.4 Instrument

CHIME is a novel telescope that carefully pairs its signal processing and analysis pipeline with its instrumental specifications. It is a cylindrical radio interferometer aligned in the north-south direction, and has no moving parts. As a transit telescope, it looks at the

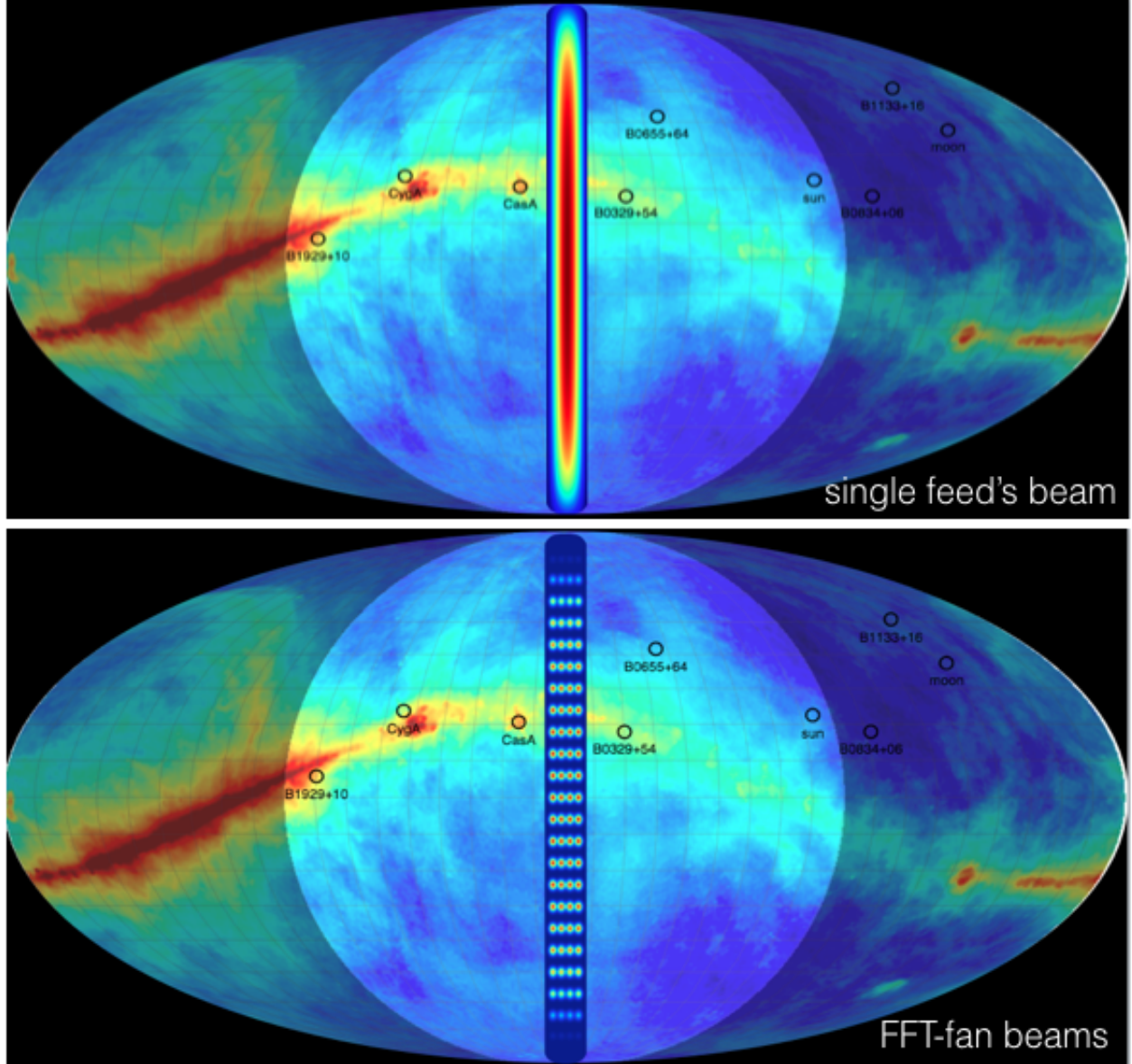


Figure 1.5: *top panel:* The simulated on-sky response of a single feed on a CHIME cylinder, plotted over the Haslam et al. (1982) map at 408 MHz in ground coordinates. The brightened circular area shows the above-horizon region at DRAO at a local sidereal time of roughly 1h30m00s. *bottom panel:* The on-sky response after FFT-beamforming of the array with feeds populated along all four CHIME cylinders. This helps visualize the number of independent modes CHIME can measure at a given time, since the final synthesized fan-beams contain the same information as the full N^2 correlation. These FFT-beams are also what will be searched in the FRB back-end. A multi-parameter search will be run in real-time on the 1024 Stokes I beams formed in the FRB back-end, with the ability to write to disk baseband information for polarization studies.

	Pathfinder	Full CHIME
Geometric area	1,480 m ²	8,000 m ²
Frequency	400-800 MHz	400-800 MHz
Redshift	2.5-0.8	2.5-0.8
Beamsize	2.5°-1.3°	0.43°-0.22°
No. cylinders	2 (20x37 m)	4 (20x100 m)
No. dual-pol antennas	128	1024
No. tracking beams	1	10
No. FFT beams	?	1024
No. freq channels	1,024	1,024 (cosm, psr), 16,384 (frb)
E-W FoV	2.5°-1.3°	2.5°-1.3°
N-S FoV	~100°	~100°
Receiver Temperature	50 K	50 K

Table 1.1: CHIME Parameters

meridian as the earth rotates and the sky passes overhead, and has an on-sky duty-cycle of 100%. Since its reflectors are parabolic cylinders, light is focused only in the east-west direction, with a transverse beam-width given by $\frac{\lambda}{D_{EW}}$, or a couple degrees. In the north-south direction the dish effectively acts as a mirror. This results in a large declination beam that can see nearly the whole north-south sky, barring the antenna’s beam and cosine projection at low-elevation. To gain north-south spatial resolution, CHIME’s focal line is populated with broad-band, dual-polarization antennas that we call “clover” feeds due to their four petals, shown in Fig. 1.4. The signals from these feeds can be interfered either in beamforming or by traditional interferometric correlation in order to obtain north-south spatial resolution.

1.4.1 Clover-feeds

The feed petals are made from printed circuit boards (PCB)(Bandura, 2014). The balun and support going up to the backplane are made from Teflon-based PCB in order to minimize loss. Electrical loss is also reduced by removing all material from along the slot transmission. The clover feeds are distributed along the focal lines in groups of four,



Figure 1.6: Photograph of eight clover feeds on the CHIME Pathfinder. They are separated by ~ 30 cm and mounted in groups of four on cassettes containing each feed’s electronics, as well as house-keeping instrumentation. The focal line is 5 m above the reflector.

mounted to steel “cassettes”, each of which contains one power source and electronics for thermometry. This focal line configuration can be seen in Fig. 1.4.

Aliasing

The feeds are separated by ~ 30 cm, constrained by their physical size and the requirements of a 400-800 MHz feed. This is problematic for the top of our band. Since we observe at 37.5-75 cm, wavelengths shorter than twice the physical separation of our feeds will not be properly Nyquist sampled. Therefore below ~ 60 cm (above ~ 500 MHz) we do not uniquely measure the electric field in the north-south direction and our signal will be aliased. In other words, without further information, a point source’s declination will be ambiguous at high frequencies at any given time. An example of this is shown with a simulated formed beam shown in Fig. 1.4.1.

1.4.2 Amplifiers

After light bounces off the reflector and couples to the clover feeds, the signal is amplified by low-noise amplifiers (LNAs) attached directly to the antennas at the focus. It has two

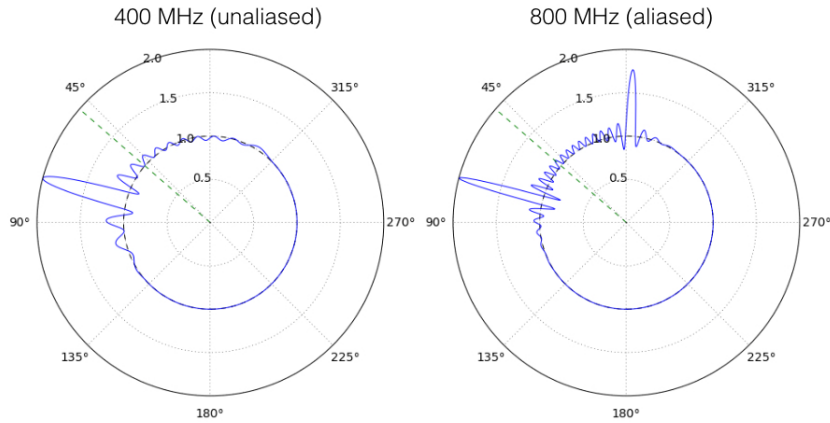


Figure 1.7: A demonstration of aliasing at short wavelengths, based on a simple simulation. In both polar plots (400 MHz left, 800 MHz on the right) a beam is formed at a $\sim 70^\circ$, effectively giving the array’s response in that direction. At high frequencies the signal is aliased: One cannot differentiate between the location on which the beam was formed and the pixel at $\sim 350^\circ$.

stages of amplification: The first is based on an Avago 54143 GaAs enhancement mode pseudomorphic high electron mobility transistor (E-pHEMT). It is followed by an Avago MGA-62563 E-pHEMT radio frequency integrated circuit (RFIC). The noise figure across most of the band is ~ 35 K (Bandura, 2014). The LNA is noise matched rather than impedance matched, resulting in a relatively large reflection coefficient.

The signal is then sent through ~ 60 m of coaxial cable down the cylinder’s central strut and into the correlator Sea Can, within which there is an RF-shielded room containing all of the correlator hardware. The Pathfinder’s 256 channels are then passed through a second stage of amplification in the filter amps.

1.4.3 Correlator

Both the Pathfinder and full CHIME have “FX” correlators, meaning the signal is first Fourier transformed and then correlated. On the Pathfinder, the signals from the 256

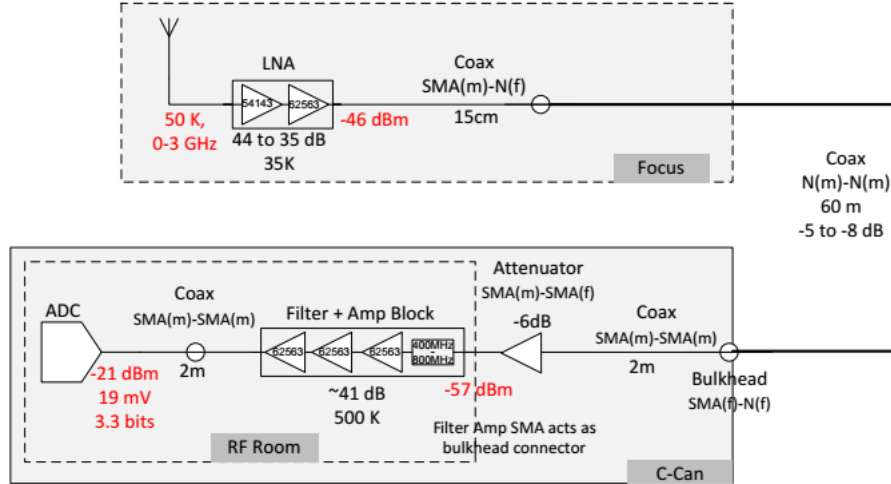


Figure 1.8: Diagram of the CHIME Pathfinder analog chain taken from (Bandura, 2014). The sky signal is amplified in the LNA block by 35-44 dB across the band, adding ~ 35 K of noise. It is then sent across roughly 60 m of LMR-400 coaxial cable to an RF-shielded room. The signal is attenuated, then bandpass filtered over the 400-800 MHz band. It is amplified again by ~ 40 dB in the FLAs before being digitized in the ADCs.

feeds are split up and sent to the F-engine where a polyphase filterbank (PFB) is applied. The PFB does the channelization and it similar to a Fourier transform, except that it mitigates channel-to-channel leakage in the presence of strong RFI. All channels must then be brought back together for the full N^2 correlation, so each of the 16 GPU nodes gets one sixteenth of all frequencies. A similar digital back-end will exist for CHIME, but scaled up, with 256 GPU nodes.

F-engine

CHIME Pathfinder's F-engine consists of 16 custom FPGA boards, each with 16 ADCs, which sample the analog signal at 800 MSps at 8 bits and channelize the data into 1024 frequency bins (Recnik et al., 2015).

X-engine

The correlation component of CHIME’s back-end is a custom GPU-based cluster of consumer-grade AMD cards (Denman et al., 2015). The Pathfinder X-engine is made of 16 nodes, each containing 2 Fury X GPUs. XX of the nodes are water-cooled and XX of the nodes are air-cooled. The cluster is one of the largest such systems in operation, correlating 32,896 input pairs and 1024 frequency channels over the 400 MHz of bandwidth. Its kernels are written in OpenCL.

1.4.4 Beams

CHIME’s design and analysis approach has forced the collaboration to wager that it will be able to understand its instrument exceedingly well. Shaw et al. (2015) showed that in order to recover a largely unbiased powerspectrum after foreground removal, beamwidths must be known to 0.1%, and complex gains must be known to 1% each minute. Their analysis was based on simulation and a simple proxy for beam characterization (namely width in one dimension), but ultimately we will have to understand the whole 2D beam at each frequency and for all antennas.

Our approach to calibration is described in (Newburgh et al., 2014). For beam-mapping, a technique known as holography is being used whereby a steerable secondary telescope tracks sources as they drift through the CHIME beams. By correlating the tracking telescope (in our case the 26 m John A. Galt antenna) with the CHIME feed, one can pull out the CHIME feed’s electric field response. This gives both the amplitude and phase of all beams on the array for an hour angle track of constant declination, and also eschews the confusion issue that comes from having such a large north-south beam. For reference, see the top panel of Fig. 1.3.3.

Cylinder rotation

Before a full-fledged holography programme could commence, we began to learn about our beams through the transits of bright point-sources. Shortly after the Pathfinder saw first light, we noticed point-sources were transiting at different times than we might expect. This phenomenon seemed to be declination-dependent, with objects north of zenith arriving late and objects south of zenith arriving early. We found this to be due to a 1.96° cylinder rotation in the positive azimuthal direction. This was caused by miscommunication with the XX about the conversion between Universal Transverse Mercator (UTM) and Geographic coordinates, i.e. the use of easting/northing with latitude/longitude.

Frequency dependence

A more difficult phenomenon to explain, which we also discovered in early point-source transits, was an ever-present ~ 30 MHz ripple in our frequency beams. 30 MHz is the frequency of a wave with length ~ 10 m, which is what one would expect from a 5 m standing wave between the vertex of our cylinder's reflector and the focal line. This standing wave was found to cause a ripple in our beam's full-width half maximum (FWHM) of order 30%, as can be seen in Fig. 1.4.4.

Frequency ripples in our beam-widths or forward gain caused by intra-reflector bounces might have been predicted, as it has been seen in other telescopes (Popping & Braun, 2008, e.g.). However, shortly after the Pathfinder began taking data steadily, we noticed a more confounding issue: Oscillation in frequency of the pointing of our beams. On top of the declination-dependent mis-pointing of our beams, we also discovered a pointing oscillation in frequency with a period of 30 MHz. Strong, sinusoidal frequency-dependent pointing seems to be a novel issue. This is shown in Fig. 1.4.4. At first this pointing wander was hard to explain, since it seemed to require and systematic east-west asymmetry. The only obvious directionality in the system was the fact that in a two-dish system,

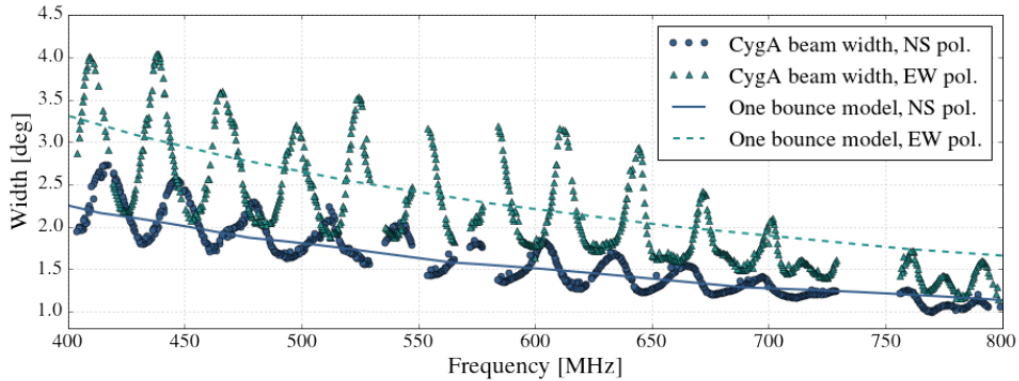


Figure 1.9: Beam full-width half maximum vs. frequency for a single dual-polarization CHIME Pathfinder antenna, based on the Gaussian fits to a Cygnus A transit. The turquoise triangles are the data for the east-west polarization and the blue circles are the north-south beam. Over-plotted in dashed and solid lines are the model. The true beam-widths show a drastic 30 MHz oscillation, resulting in nearly a 2° difference between ~ 420 MHz and ~ 445 MHz. This implies an interaction between the focal line and the reflector, whose vertex is 5 m below the feeds. The model is based on the feed’s beam, which accounts for the different in antenna beams of the two polarizations. It assumes no standing wave and no surface perturbations, which is why the expected ν^{-1} is produced without any frequency ripple.

there is a cylinder walkway on one side and not the other. However, simulations showed that a bounce between focal lines produces an effect that is several orders of magnitude too small.

It now seems that the combination of a relatively large surface root-mean square (RMS) on the Pathfinder’s reflector, along with two or more bounces between the dish and the focal line, can lead to centroid wander. The system was simulated using antenna modeling software **GRASP**, using a randomly deformed reflector and a second bounce.

1.5 Conclusion

Acknowledgements

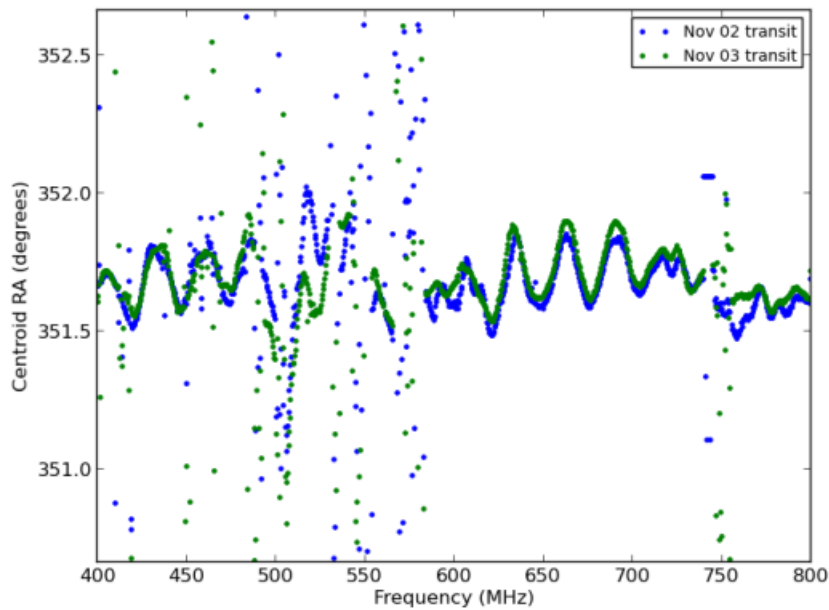


Figure 1.10: A periodic variation of the primary beam centroid for a single Pathfinder feed, measured with a transit of Cas A. Especially between 600-725 MHz, one can see a sinusoidal 30 MHz oscillation in pointing by as much as 20 arcminutes.

Chapter 2

Beamforming

2.1 Chapter Overview

In an era when electric fields can be sampled billions of times per second, radio telescopes are becoming more and more digital. While the cost of constructing large single-dish telescopes is not expected to decrease substantially, the cost of building large computing clusters is, which makes it economically and strategically sensible to point one's telescope in software, as with digital beamforming. Beamforming is particularly essential to CHIME. The pulsar back-end will rely on brute-force beamforming in order to track ten sources at a time, 24-7. The FRB experiment will FFT-beamform to generate 1024 fan-beams, in order to search them in real time for radio transients. And the cosmology experiment has always left itself the option of beamforming, whose computing cost scales as $N \log N$, as an alternative to the full N^2 correlation. This chapter outlines the basic theory behind digital beamforming, and describes the commissioning of the first beamformer on CHIME Pathfinder. This includes the synthesis of several different software packages, the implementation of an early scheduler, and an automated point-source calibration daemon that removes drifting instrumental gains in real-time. We will also detail early pulsar work and the creation of an ongoing VLBI FRB search between the

DRAO and ARO. The latter will include constraints on α .

2.2 Introduction

Beamforming is a signal processing technique that allows for spatial filtering, and has greatly benefited a diverse set of fields from radar and wireless communications to radio astronomy.

2.3 Theory and Implementation

By coherently combining the voltages of a multi-element array, sensitivity can be allocated to small regions of the sky and the array's effective forward gain can be increased. The signal from each antenna, x_n , is multiplied by a complex weight whose phases, ϕ_n , are chosen to maximally destructively interfere radio waves in all directions but the desired pointing. The signals from all antennas are then combined to give the formed-beam voltage stream, X_{BF} .

$$X_{\text{BF}} = \sum_{n=1}^N a_n e^{i\phi_n} x_n \quad (2.1)$$

Here a_n are real numbers that can be used as amplitude weightings for the antennas. If we define a more general complex weighting, $w_n \equiv a_n e^{i\phi_n}$, and switch to vector notation, Eq. 2.1 becomes,

$$X_{\text{BF}} = \mathbf{w} \mathbf{x}^T. \quad (2.2)$$

In general, X_{BF} and \mathbf{x}^T will be functions of time and frequency. This is also true for \mathbf{w} , unless one needs a static, non-tracking beam – which is the case for the CHIME Pathfinder's transient search, described in Sect. 5.5. We can write this explicitly as follows.

$$\mathbf{w}_{t\nu} = (a_1(\nu)e^{i\phi_1(\nu)}, a_2(\nu)e^{i\phi_2(\nu)}, \dots, a_N(\nu)e^{i\phi_N(\nu)}) \quad (2.3)$$

$$\mathbf{x}_{t\nu} = (x_1(t, \nu), x_2(t, \nu), \dots, x_N(t, \nu)) \quad (2.4)$$

The voltage stream is then effectively squared and integrated to give a visibility stream. In the case of CHIME, X_{BF} corresponds to a single polarization so to get the full Stokes information one must compute the north-south polarization's autocorrelation, the east-west autocorrelation, and their cross-correlation. The Stokes vector can be written as,

$$\begin{pmatrix} I \\ Q \\ U \\ V \end{pmatrix} = \begin{pmatrix} X_{\text{ew}}X_{\text{ew}}^* + X_{\text{ns}}X_{\text{ns}}^* \\ X_{\text{ew}}X_{\text{ew}}^* - X_{\text{ns}}X_{\text{ns}}^* \\ \Re(X_{\text{ew}}X_{\text{ns}}^*) \\ \Im(X_{\text{ew}}X_{\text{ns}}^*) \end{pmatrix}. \quad (2.5)$$

2.3.1 Geometric phase

We now need to calculate ϕ_n across the array. Ignoring instrumental phases for now, one can compute the geometric phases for an antenna by projecting its position vector, \mathbf{d}_n , onto the pointing vector, $\hat{\mathbf{k}}$. This gives,

$$\phi_n = \frac{2\pi}{\lambda} \mathbf{d}_n \cdot \hat{\mathbf{k}}, \quad (2.6)$$

where we have taken \mathbf{d}_n to be the baseline vector between feed n and an arbitrary reference point, and ϕ_n is the corresponding phase difference. A sketch for this is shown in Fig. 5.5.2 on page 95.

To calculate the projection $\mathbf{d}_n \cdot \hat{\mathbf{k}}$, we need to go from celestial coordinates, in this case equatorial, to geographic coordinates. This requires only a source location, an observer

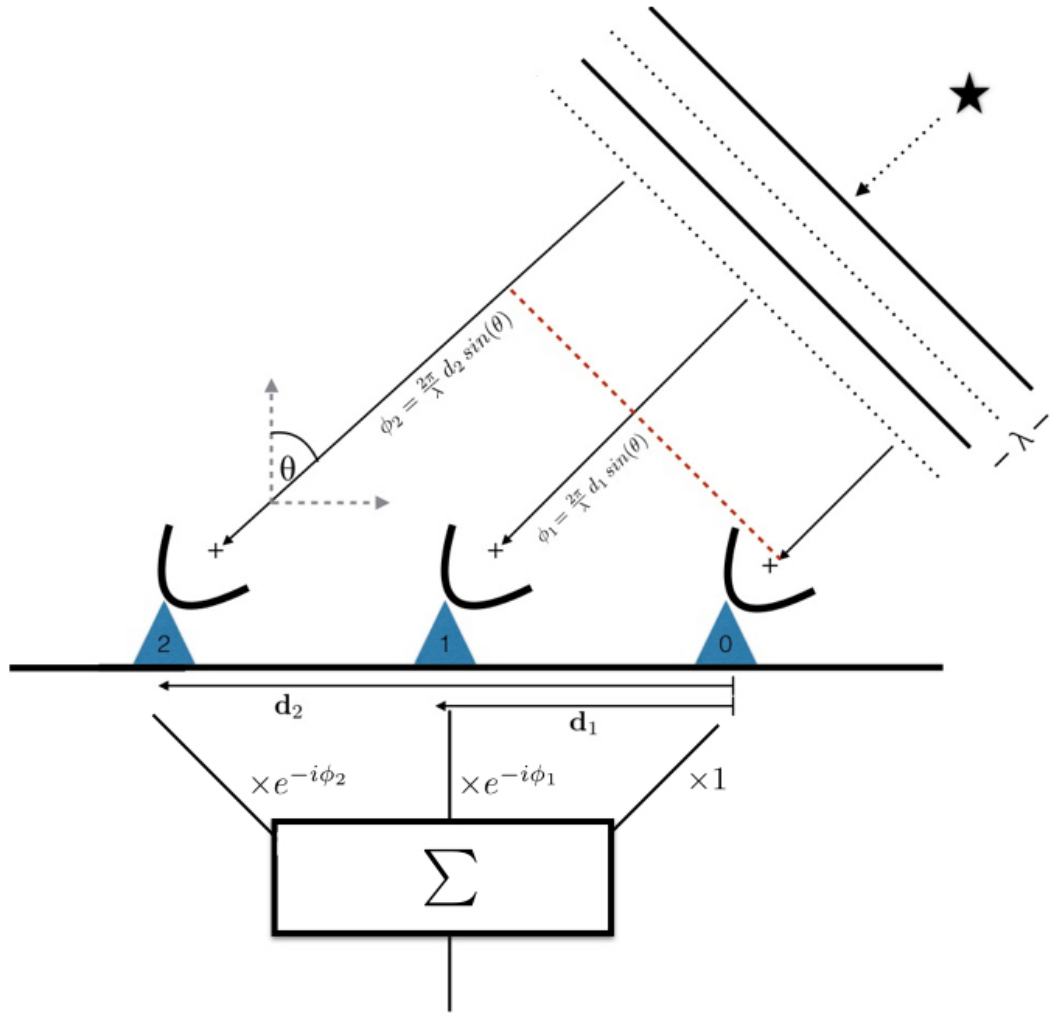


Figure 2.1: Diagrammatic example of a three-element beamformer. The wavefront from a far-field point-source arrives at each antenna at different times, but the delay is calculable given an array configuration and a direction to the object. Complex weights can be applied to each antenna's voltage time-stream to account for the geometric delay, allowing for the signals to be summed coherently.

location, and an observing time. For the latter we use local sidereal time (LST), which is the *RA* of the local meridian. This can be determined by an observer's longitude and a time, e.g. a Coordinated Universal Time (UTC). A source's hour angle is simply the difference between *LST* and its *RA*,

$$HA = LST - RA. \quad (2.7)$$

Variable	Coordinate
δ	Source declination
RA	Source right ascension
LST	Local sidereal time
HA	Source hour angle
alt	Source altitude
az	Source azimuth
lat	Telescope latitude
lon	Telescope longitude

We use the standard interferometric (u, v, w) coordinate system to describe our baseline vector, \mathbf{d}_n . This is a right-handed coordinate system where u (east-west) and v (north-south) are in the plane whose normal is the zenith, and w measures the vertical direction (Thompson et al., 1986). They are defined in numbers of wavelengths, with $u = d_{\text{ew}}/\lambda$, $v = d_{\text{ns}}/\lambda$, and $w = d_{\text{vert}}/\lambda$. Eq. 2.6 can be expanded as,

$$\phi_n = 2\pi (u, v, w) \cdot \hat{\mathbf{k}} \quad (2.8)$$

$$= 2\pi \left(u \hat{\mathbf{u}} \cdot \hat{\mathbf{k}} + v \hat{\mathbf{v}} \cdot \hat{\mathbf{k}} + w \hat{\mathbf{w}} \cdot \hat{\mathbf{k}} \right), \quad (2.9)$$

where each projection component can be obtained using spherical trigonometry. Though we do not go through the derivation here, it is given by the following product,

$$\mathbf{d}_n \cdot \hat{\mathbf{k}} = \lambda \begin{pmatrix} u, & v, & w \end{pmatrix} \cdot \begin{pmatrix} -\cos\delta \sin HA \\ \cos(lat) \sin\delta - \sin(lat) \cos\delta \cos HA \\ \sin(lat) \sin\delta + \cos(lat) \cos\delta \cos HA \end{pmatrix}. \quad (2.10)$$

These phases are not only essential to beamforming but also for the fringestopping process, which is ubiquitous in interferometric analysis and is described in Sect. 2.4.1.

2.4 Pathfinder beamformer

2.4.1 Instrumental phases

In a real experiment, if the voltages from each antenna, x_n , are summed without any adjustment from those written in Eq 2.1, one should only expect noise and not a coherent beam. This is because we have assumed the wavefront's differential time-of-arrival across the array is the same time delay seen by the correlator. In fact each signal is further delayed by multiple steps in the signal chain, often randomly. Digital phases in the electronics can be added by the LNAs and FLAs; coaxial cables, whose lengths vary by up to a meter, can rotate the signal by multiple radians. Therefore in order to coherently sum across the array and beamform, the instrumental phases must be removed. If e_n is the true electric field on the sky as seen by each feed, then the thing we measure is the on-sky signal altered by an effective gain, g_n , and a noise term, n_n .

$$x_n = g_n e_n + n_n \quad (2.11)$$

We have lumped several terms into $g_n = |g_n|e^{i\phi_{g_n}}$, which is composed of a pointing-dependent beam term and any complex gain introduced once light hits the cylinder. Since we care primarily about the phase, we can decompose $\arg(g_n)$ as,

$$\phi_{g_n} = \phi_{\text{beam}} + \phi_{\text{an}} + \phi_e + \phi_{\text{fpga}} \quad (2.12)$$

where ϕ_{beam} is the beam's phase for a given pointing, ϕ_{an} comes from the analogue chain (dual-pol feed, coax, etc.), ϕ_e is any phase introduced in the electronics, and ϕ_{fpga} are phases applied in the F-engine.

Since the instrumental phases are effectively random, the simplest way to remove them is to solve for them empirically, usually from a point-source on the sky. Using the visibility definition in Eq 2.16, one can evaluate that all-sky integral assuming the sky's

electric field is produced by a single point-source. This is tantamount to a delta function at a single direction on the sky.

$$V_{m,n}^{\text{ps}} = \int d^2\hat{\mathbf{k}} g_m(\hat{\mathbf{k}}) g_n^*(\hat{\mathbf{k}}) e_m(\hat{\mathbf{k}}) e_n^*(\hat{\mathbf{k}}) \delta(\hat{\mathbf{k}} - \hat{\mathbf{k}}_{\text{ps}}) \quad (2.13)$$

$$= g_m(\hat{\mathbf{k}}_{\text{ps}}) g_n^*(\hat{\mathbf{k}}_{\text{ps}}) e_m(\hat{\mathbf{k}}_{\text{ps}}) e_n^*(\hat{\mathbf{k}}_{\text{ps}}) \quad (2.14)$$

In these equations $\hat{\mathbf{k}}_{\text{ps}}$ is the only direction on the sky with a source in it — an approximation whose validity we will discuss below — and δ is a Kronecker delta function.

$$V_{m,n}^{\text{ps}} = \quad (2.15)$$

$$V_{m,n} = \int d^2\hat{\mathbf{k}} g_m(\hat{\mathbf{k}}) g_n^*(\hat{\mathbf{k}}) e_m(\hat{\mathbf{k}}) e_n^*(\hat{\mathbf{k}}) \quad (2.16)$$

If we explicitly write the phase information of the sky's electric field, we can use

$$e_m(\hat{\mathbf{k}}) e_n^*(\hat{\mathbf{k}}) = T(\hat{\mathbf{k}}) e^{2\pi i \hat{\mathbf{k}} \cdot \mathbf{d}_{mn}}, \quad (2.17)$$

subbing into Eq. 2.13

$$V_{m,n} = \int d^2\hat{\mathbf{k}} g_m(\hat{\mathbf{k}}) g_n^*(\hat{\mathbf{k}}) T(\hat{\mathbf{k}}) e^{2\pi i \hat{\mathbf{k}} \cdot \mathbf{d}_{mn}} \quad (2.18)$$

Therefore a single correlation can be written as an intensity multiplied by a phase factor that is determined by the source direction's projection onto that correlation's baseline. Since that phase factor is calculable via Eq. 2.10, it can be removed in a process called “fringestopping”. The data can be inspected visually quite easily, since a transiting point-source will fringe as a function of time at a rate corresponding to the projected baseline length, but should not after fringestopping is applied. This is

demonstrated with an inter-cylinder Cygnus A transit in Fig. 2.4.1.

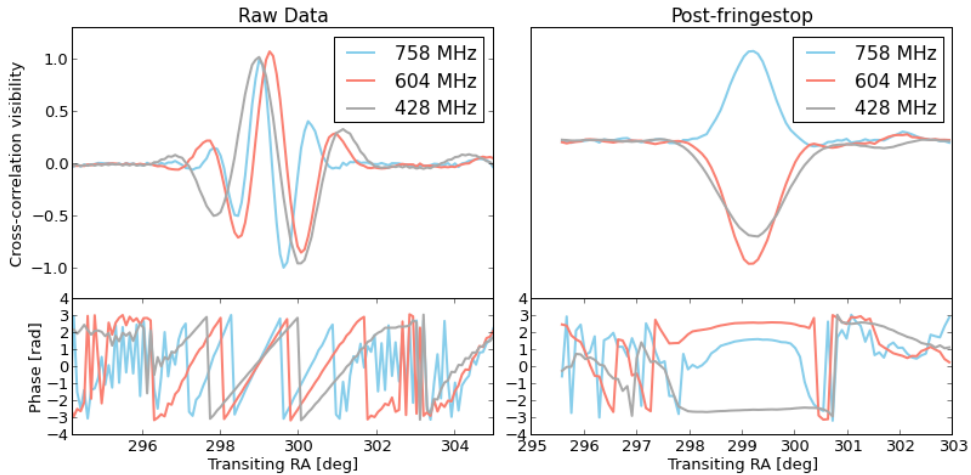


Figure 2.2: An example of the fringestopping process that is necessary for gain calibration off of a transiting point-source. Since the phase of a visibility will have a time- and frequency-dependent component, the measured correlation will fringe as the earth rotates in a chromatic way. This effect can be removed by multiplying each visibility by $e^{-i\phi_{m,n}(t,\nu)}$, as determined by Eq. 2.10. The top left panel shows the raw correlation between feeds 1 and 129 as a function of transiting RA , which are of the same polarization but on opposite cylinders, separated by 21 m. We plot three different frequencies. The panel below the top left shows the same complex visibility's phase. The slope, or fringe-rate, decreases at lower frequencies, as expected. The right panel show the same data after running it through the fringestopping pipeline. Though the resulting phases are near flat, implying that the baseline is no long fringeing, the visibilities are not purely real; this is because there are residual instrumental phases. These phases can be solved for using an eigendecomposition now that the array is phased up to a single point-source.

The visibilities we measure can be thought of as the upper triangle of an $N \times N$ complex Hermitian matrix, \mathbf{V} . This is simply the outer product of the signal vector, \mathbf{x} , with its Hermitian conjugate.

$$\mathbf{V} = \mathbf{x}\mathbf{x}^\dagger \approx \begin{pmatrix} |g_0|^2 e_0^2 & \dots & & \\ & & g_n g_m^* e_n e_m^* & \\ & \ddots & & \\ & & & |g_N|^2 e_N^2 \end{pmatrix} \quad (2.19)$$

If the sky is composed of a single point-source then this matrix will be rank one, i.e. there is only one non-zero eigenvalue. One can see this by referring to Eq. 2.17 and noting that if the data has been fringestopped, then the phase component (which is different for each correlation) goes away and the sky temperature (which is the same) can be factored out of Eq. 2.19, which becomes

$$\mathbf{V} = T(\hat{\mathbf{k}}) \mathbf{g} \mathbf{g}^\dagger. \quad (2.20)$$

Therefore by diagonalizing the correlation matrix \mathbf{V} we get a complex eigenvector corresponding to the largest eigenvalue, and that eigenvector is proportional to the gain vector \mathbf{g} . The phase of this eigenvector will be an estimate for the instrumental phases, ϕ_{g_n} , up to some unknown global offset. The goodness of this calibration depends on the validity of our assumption that the correlation matrix is rank one. We can estimate the error on the calibration solution as the ratio of the second largest eigenvalue, λ_2 , to the largest, λ_1 . For typical frequencies we get values of $\frac{\lambda_2}{\lambda_1} \sim 3\%$.

These algorithms have been implemented in a pre-beamforming pipeline written in Python. Each day a point-source transit is fringestopped and a calibration solution is solved for at each frequency. The source chosen depends on the solar time of its transit:

Since the sun is extraordinarily bright in our band it will be in our side-lobes as long as it is above the horizon, so the transit has to be at night for good calibration solutions. Historically, we have used Cygnus A in the spring and summer, Cassiopeia A in the summer and fall, and Tau A in the winter. Whatever we calibrate off of, the phases of that solution are written to pickle files that are readable by the Pathfinder's FPGAs. The FPGA then applies complex gains after channelization, which in theory should provide the beamforming kernel with voltages whose phases are purely geometric.

2.4.2 First coherent light

Although the majority of the back-end was written within a couple of months, the beamformer required substantial on-sky testing and subsequent debugging. One important debugging tool came from utilizing the equivalence of the summed-and-squared high-cadence data that was produced by the beamformer with the full N^2 integrated data. This is true because the correlation step does not erase any fundamental information about the electric field. The latter is nominally taken with ~ 21 second time samples for 32,896 correlation products coming from 256 feeds. The former is a sum over the feeds which can be integrated in time arbitrarily after squaring. Ignoring the time rebinning for a moment, we can write the squared formed beam as,

$$X_{\text{BF}} X_{\text{BF}}^* = (w_1 x_1 + w_2 x_2 + \dots + w_N x_N)(w_1 x_1 + w_2 x_2 + \dots + w_N x_N)^* \quad (2.21)$$

$$= |w_1|^2 |x_1|^2 + \dots + |w_N|^2 |x_N|^2 + \dots + w_1 w_2^* x_1 x_2^* + w_2 w_1^* x_2 x_1^* + \dots, \quad (2.22)$$

where, as before, w_n are the complex weights applied in the beamformer and x_n is a voltage stream from antenna n . This can be rewritten as the sum of the auto correlations

and twice the real part of the recorded cross-correlations.

$$X_{\text{BF}} X_{\text{BF}}^* = \sum_{n \leq N} |w_n|^2 V_{n,n} + 2 \sum_{\substack{n,m \leq N \\ n < m}} \Re e\{W_{n,m} V_{n,m}\} \quad (2.23)$$

In this equation we have let $W_{n,m} \equiv w_n w_m^*$. Since the correlation matrix is Hermitian, its top and bottom triangles are redundant and one needs only to record $\frac{1}{2}N(N+1)$ of the N^2 pairwise products. If we wrote all pairwise correlations, we would simply need to sum the correlation matrix after applying the relevant weights, i.e. summing after the Hadamard product, $\mathbf{W} \circ \mathbf{V}$. This is identical to Eq. 5.3 if both matrices are Hermitian.

Using the equivalence we have just described, one can compare the output of the beamformer to the N^2 visibilities after applying complex weights and summing the correlations. This is effectively off-line beamforming, though the cadence is too slow for the science goals of the real back-end, namely studying the time-variable sky. As a first test, we would form a stationary beam with only two feeds and let a bright point-source like Cas A drift through, producing a fringe pattern. We would then take the corresponding Cas A transit from the correlated “cosmology” acquisition, using Eq. 5.3 and giving only non-zero weights to the two relevant feeds, and check if the two fringe patterns were identical. We carried out a series of tests of escalating complexity, for example including more feeds in the sum, updating phases in real-time in order to track sources, and deliberately switching the weights with their conjugate to see if the fringe direction changed. Through these tests several bugs were discovered, including spherical trigonometry errors in the phase calculations and a disagreement between one piece of code’s definition of *LST*.

The final hurdle was more fundamental to CHIME’s architecture, though in principle it should not affect the cosmology experiment. It was found through early pulsar obser-

vations that the beamformer was only summing coherently when the instrumental phases that are removed in the FPGAs are solved for with the lower-triangle of the correlation matrix. In other words, instrumental phases were not properly removed in the correlator unless they were applied as $e^{+i\phi_{gn}}$ instead of $e^{-i\phi_{gn}}$, as one would expect. The perplexing thing was that in two years of analyzing

the visibilities output by the correlator, nobody noticed a error in the sign-convention. And indeed, when we started to look at the phase of the raw visibilities, we found the argument of an east-west baseline increases with time, which is what one expects from an upper-triangle correlator. This apparent paradox was solved by discovering *two* sign errors, one in the F-engine and one in the X-engine, that effectively cancel each other out, but only if both are applied.

Our digitizers sample at 800 MHz, taking advantage of the observing band between 400-800 MHz being in the second Nyquist zone . However, when we channelize the incoming time-stream data in the FPGAs, the complex conjugation associated with the aliased second Nyquist zone was not considered during the Fourier transform. Therefore the channelized voltages leave the F-engine with an opposite sign in the exponential. When they are correlated in the X-engine it is also done in reverse order as,

$$V_{n,m} = x_n^* x_m, \quad (2.24)$$

as opposed to the upper-triangle correlation described by Klages et al. (2015),

$$V_{n,m} = x_n x_m^*. \quad (2.25)$$

The second sign convention error does not affect the beamformed output, since that data stream is never correlated. We therefore needed to account for this for the back-end to work. An example of an early verification of the beamformer's sign convention and the first successful tracking observation is shown in Fig. 5.4.3. The collaboration has

decided to keep these sign conventions as is and make note of it going forward, rather than re-write any low-level software.

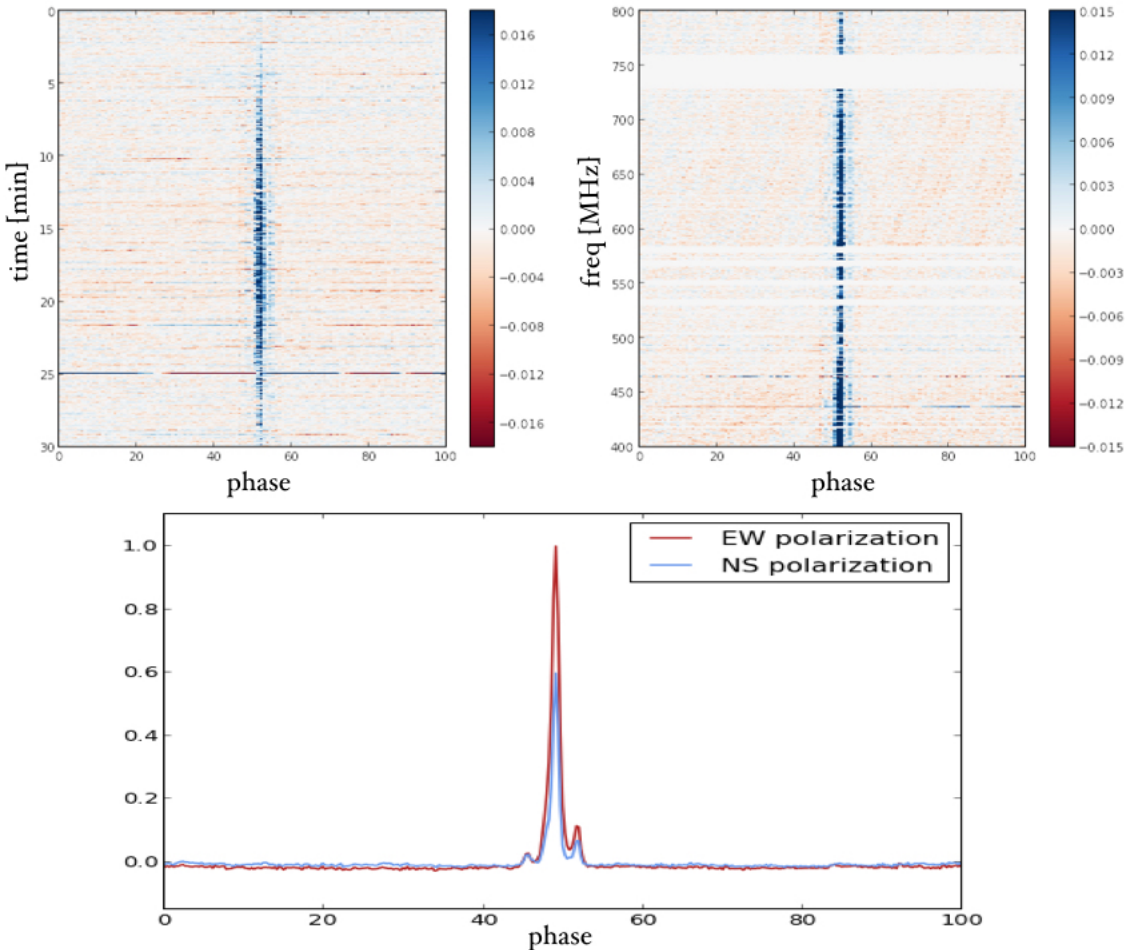


Figure 2.3: First coherent pulsar observations with CHIME. This brief observation of B0329+54 provided us with an idea of the instrument’s sensitivity and polarization response. Perhaps more significantly, it taught us that that our X-engine is a lower-triangle correlator, rather than upper-triangle like we thought, and that our F-engine *also* conjugates with the opposite sign. *top left:* waterfall plot of the pulsar’s Stokes I profile over the ~ 30 minutes when the source enters then exits our beam. *top right:* frequency vs. phase Stokes I, integrated over roughly 15 minutes. *bottom:* time- and frequency-averaged pulse profile for the two polarizations autocorrelations. The difference between the east-west and north-south beams give an estimate for Stokes Q, which includes both intrinsic polarization ($\sim 10\%$ for this source) and instrumental leakage.

2.5 FRB VLBI search

In 1967 Canada achieved an historic feat by doing the first ever successful VLBI observation. The fringes were obtained between DRAO and ARO, with a baseline of 3,074 km (Broten et al., 1967). This result was given a “Milestone” award from The Institute of Electrical and Electronics Engineers (IEEE), which was also awarded for the inception of the Internet, transmission of transatlantic radio signals, and the discovery of Maxwell’s equations (IEE, ????). We have attempted to recreate the same VLBI baseline, but instead of using the considerable spatial resolution on quasars as in 1967, we are attempting to localize FRBs.

2.5.1 Motivation

The CHIME Pathfinder is meant to have only one synthetic beam. Its purpose is primarily to act as a test-bed for the more powerful pulsar and FRB back-ends that will be attached to the full four-cylinder CHIME. However since the Pathfinder is on sky at all times and the beamformer we have built does not interrupt the ongoing cosmology acquisition, we decided to build a preliminary FRB search. We also have as many as three other telescopes onto which we can mount CHIME feeds and observe in our band: the Algonquin Radio Observatory (ARO), the John A. Galt 26m, and the Green Bank 140ft telescope. This would allow for the first ever VLBI detection of an FRB.

This is interesting for a few reasons. From a development standpoint it allows us to understand better various stages of the CHIME-FRB pipeline, including the rate of RFI false-positives, our algorithm’s search efficiency, and specs on the regularity and precision of instrumental gain removal. It will also give us a good sense of how the real CHIME beams behave on the sky. Perhaps most interestingly, we could reasonably expect to see a burst after several months of observing, hopefully in coincidence with the telescopes previously mentioned. We could therefore not only detect an FRB with sub-arcsecond

resolution, but also would the first source in our band, at 400-800 MHz, including full polarization information. While searching for fast radio bursts, we could also find RRATs and new slow pulsars, since a significant fraction of the Galaxy transits each day.

2.5.2 Implementation

We have had a working beamforming back-end on the CHIME Pathfinder since October 2015. It has been used primarily for short tracking pulsar observations, but had stability issues on timescales of \sim days, meaning we could not run it for long periods without interfering with the regular cosmology acquisition. However in the past several months a number of new features were added that allow not only long-term beamforming captures, but also transient searching.

A real-time, multithreaded acquisition code that takes in the VDIF packets coming out of the X-engine, and rearranges them to either be written to disk or search for FRBs¹. Attached to this packet reader was a tree-dedispersion search code, some of which had been used before on Green Bank 100m data and a real-time ARO search². The CHIME acquisition software `kotekan` was altered in a number of ways, fixing the long-term stability issues in the beamforming kernel. These systems were synthesized into a real-time transient search back-end that has been on sky since May 2016. It is outlined in Fig. 5.5.2 on page 95.

Since CHIME is a transit telescope with a long north-south beam, our formed beam is effectively confined to the meridian. This means we must choose an optimal declination on which to park the beam. As a sanity check, we spent ~ 10 days pointed at the declination of pulsar B0329+54, which is the brightest switching source in the northern sky in our band. It is dispersed with $26.833 \text{ pc cm}^{-3}$ and its individual pulses are bright enough to detect, meaning our tree-dedispersion algorithm ought to find its individual pulses. The search algorithm looks at time blocks of 100 seconds, searches for DMs

¹https://github.com/kmsmith137/ch_vdif_assembler

²https://github.com/kiyo-masui/burst_search

between 10-2000 pc cm⁻³ with widths between 1-100 ms, and looks for peaks above 8σ . If it finds something it “triggers” and writes out an image file containing the peak in DM / arrival time space, a dedispersed waterfall plot, a dedispersed pulse profile, and a fluence frequency spectrum. An example of the B0329+54 is shown in Fig.???. It also writes `numpy` arrays containing the squared and summed intensity data. It then moves on to the next block of 100 seconds, overlapping with the previous one by 18 seconds.

2.5.3 ARO FRB search

2.5.4 Results

As we discuss in chapter 4, there is a large uncertainty in the FRB rate between 400-800 MHz. There is even greater uncertainty in the expected rate for a telescope like the CHIME Pathfinder. This is because at the moment of this thesis all FRBs have been detected with large-collecting area, highly sensitive single-dish telescopes (GBT, Parkes, and Arecibo). Therefore in order to extrapolate the rate estimates on to the Pathfinder, which does not have much collecting area and whose beam is quite large, one needs to know the underlying flux distribution. As we will show in Eq. 4.11, the rate depends on the product of the telescope’s field-of-view (FoV) and a thermal sensitivity term. This scales $\propto A^{-1}A^\gamma$, where A is collecting area and γ is the FRB flux distribution’s power-law index, which is 3/2 if FRBs are non-cosmological and Euclidean. If $\gamma < 1$, as is expected in the cosmological FRB scenario, then small telescopes are actually advantageous over large single-pixel telescopes since the beamsize becomes more important.

With a dish like the Pathfinder the rate is roughly 10 times higher if $\gamma \approx 0.8$ (cosmological scenario) compared to the Euclidean scenario. This is because its relatively low sensitivity per steradian requires there be large numbers of very bright bursts, which one gets from a flat distribution.

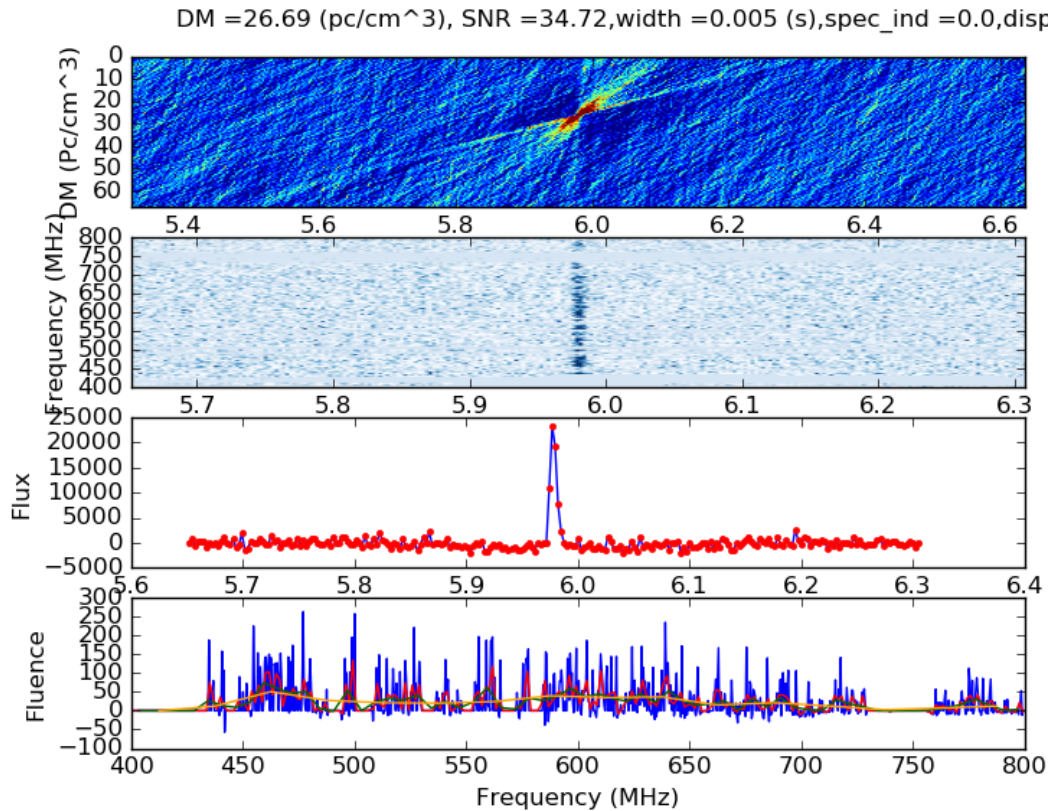


Figure 2.4: Example of a figure created after a trigger on the Pathfinder FRB search. This trigger was during the transit of pulsar B0329+54, on whose declination our synthetic beam was parked. Further information about the pulse is included at the top of the figure, including signal-to-noise ratio, width, and dispersion index. Though the beam is not well calibrated in absolute flux, this pulsar is of order 10 Jy, so this pulse might be half as bright as the original Lorimer burst (Lorimer et al., 2007a). *Top panel:* The search results in dispersion measure vs. arrival time space. The red, butterfly-like cluster of points around DM of 25 pc cm⁻³ and arrival time 6 seconds into the 100 second block, shows the detection of a single B0329+54 pulse. *Second panel:* A frequency vs. time colour map showing the dedispersed pulse. *Third panel:* Pulse profile for this trigger, averaged over frequency after masking RFI and weighting by inverse system temperature. *Bottom panel:* Fluence vs. frequency plot of the pulse.

2.5.5 False positives

Most transient searches are plagued by non-celestial sources masquerading as astronomical events. In the case of dedispersion searches on radio telescopes, these can be caused by RFI, numerical relics in the signal chain, or statistical fluctuations. At UTMOST,

Caleb et al. (2016b) found 10^2 events per hour in transit mode across all beams. Petroff et al. (2015d) found the source of an elusive but persistent set of triggers to be due to an on-site microwave oven’s magnetron shutdown phase. These “Perytons” are unique in their conspiratorial ability to look like a real burst, but they are a subset of a broader zoo of RFI-induced false triggers.

At DRAO, although the region is officially protected from radio contamination, about 15% of the CHIME band is presently lost to RFI (see the bottom left panel of Fig. 2.5.5). Recently, Rogers Communications paid several billion Canadian dollars for a 700 MHz Long-Term Evolution (LTE) band for cellphone service. Unlike the satellite television stations that we see at 500-600 MHz, the LTE band fluctuates on timescales of milliseconds to seconds, which can affect a millisecond transient search. Fig. 2.5.5 shows an example of this RFI false positive from the LTE band.

2.6 Conclusion

Acknowledgements

We thank Andre Recnik

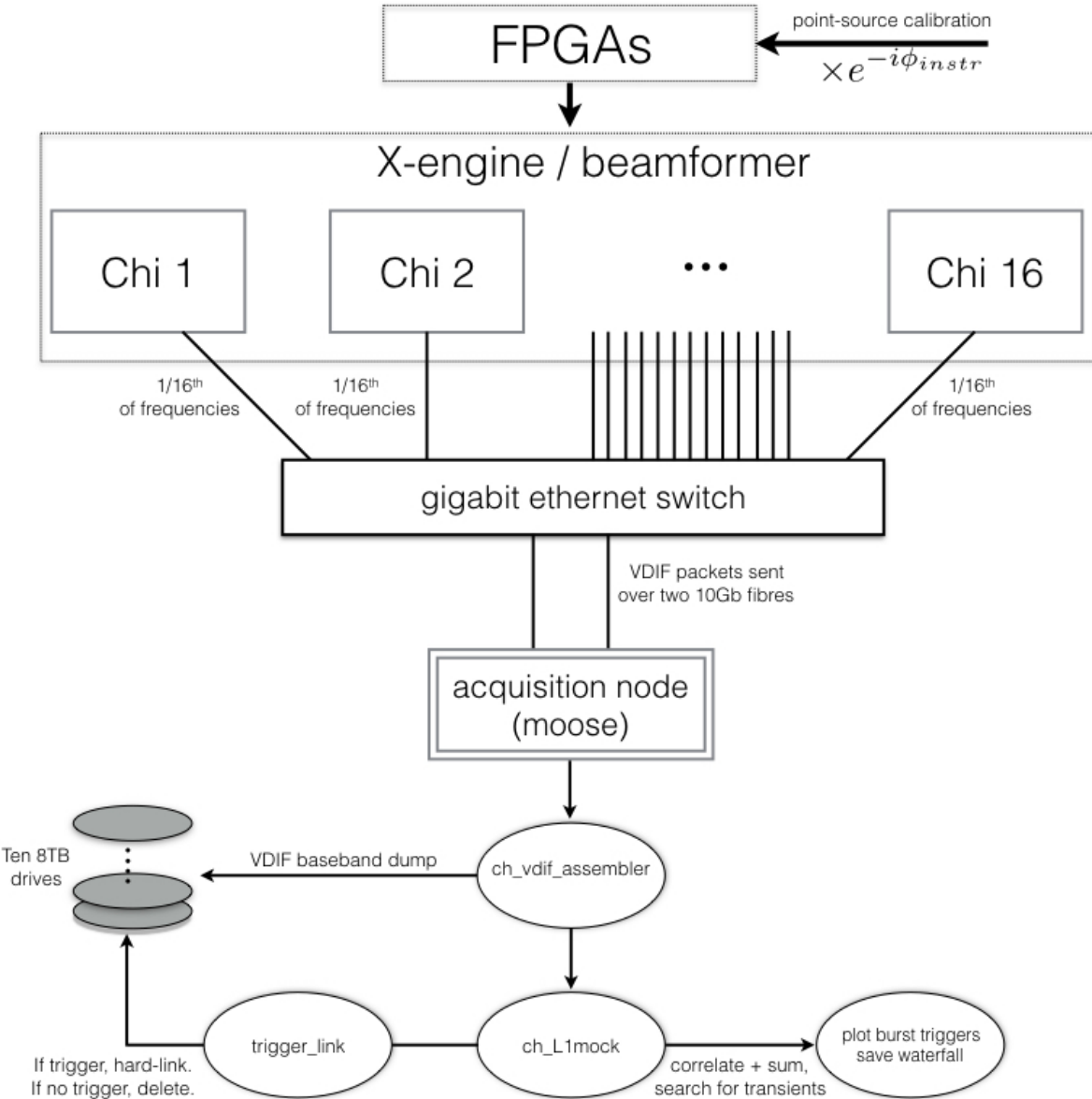


Figure 2.5: Block diagram of the beamforming back-end on CHIME Pathfinder. A calibration solution is obtained from a bright point-source transit, the phases of which are fed into the FPGAs where they are applied as a digital gain. All antenna signals are then sent the *X*-engine, comprised of 16 GPU nodes. Each node applies geometric phases then sums the voltage stream across all antennas with the same polarization. The two resultant beams are then sent to our acquisition machine `moose` as VDIF packets, where a multi-threaded capture code, `ch_vdif_assembler`. At this point the baseband data are either written to disk as scrambled baseband VDIF, or they are reorganized in time and frequency. The ordered data are searched for FRBs after squaring and integrating to \sim millisecond cadence using a tree-dedispersion algorithm. If there is a trigger, then the corresponding baseband data is hard-linked. Old files that haven't been hard-linked are deleted periodically.

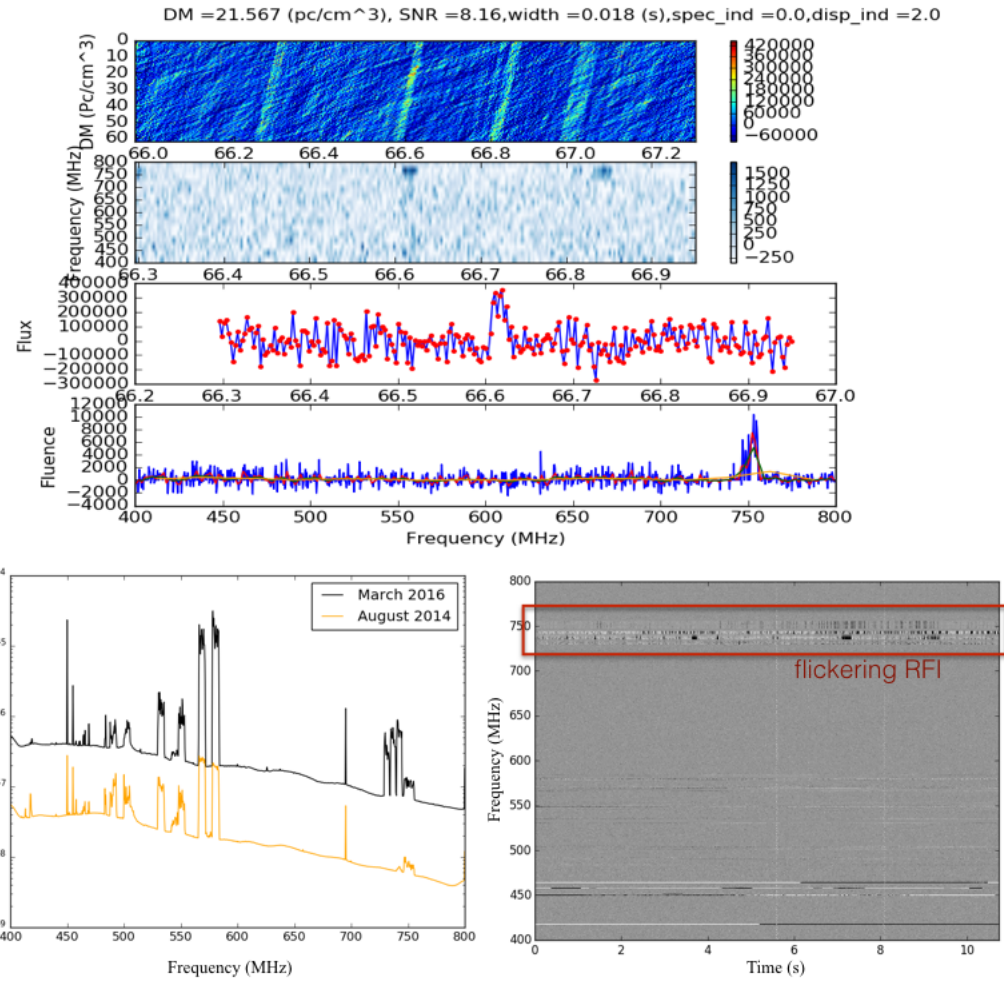


Figure 2.6: A false positive trigger caused by the flickering LTE band that, the likes of which caused $\sim 90\%$ of the alerts before it was removed. It is of course simple to reject; one can just mask out the relevant channels. However, it provides a useful example of the types of short-timescale RFI that can affect an FRB survey.

Chapter 3

Non-cosmological but Extragalactic Fast Radio Bursts

This chapter was adapted from a paper published in the Monthly Notices of the Royal Astronomical Society called “Non-Cosmological FRBs from Young Supernova Remnant Pulsars” (Connor et al., 2016f).

3.1 Chapter Overview

3.2 Introduction

3.3 Introduction

The mystery of fast radio bursts (FRBs) has garnered substantial interest from the radio community. High-energy astrophysicists have tried to model their burst source, observers would like to measure a large population of them, and cosmologists hope to use them as a probe of the intergalactic medium (IGM). However their relative scarcity (only \sim dozen have been observed so far) and their apparent transient nature mean that we still do not know their position on the sky to better than a few arcminutes, and their radial

position could be anything from terrestrial to cosmological (Kulkarni et al., 2014).

These objects are highly dispersed, with dispersion measures (DMs) ($\sim 375\text{-}1600 \text{ pc cm}^{-3}$) far exceeding the expected contribution from our own Galaxy's interstellar medium (ISM) ($10\text{-}100 \text{ pc cm}^{-3}$) and leading to the interpretation that FRBs are cosmological (Lorimer et al., 2007b; Thornton et al., 2013a). Various emission mechanisms have been proposed at a wide range of source locations, including merging white dwarfs (Kashiyama et al., 2013) and neutron stars (Totani, 2013), supergiant pulses from extragalactic neutron stars (Cordes & Wasserman, 2015), blitzars (Falcke & Rezzolla, 2014), magnetars (Popov & Postnov, 2007; Lyubarsky, 2014; Pen & Connor, 2015a), and flaring Galactic stars (Loeb et al., 2014). Though presently there are more theoretical models for FRBs than actual sources discovered, constraints on such theories are rapidly emerging. This is due to recent polarization data, multifrequency coverage, and their being observed by several telescopes at various locations on the sky (Bower et al., 2014; Petroff et al., 2015a).

On top of event rates ($\sim 10^4$ per day per sky) and high DMs, explanations of FRBs must now account for temporal scattering, and polarization states. They should predict or explain Faraday rotation and time dependence of linear polarization. The rotation measure (RM) of our Galaxy has been mapped, and the intergalactic RM is constrained to be less than 7 rad m^{-2} (Oppermann et al., 2015). The observed temporal scattering is problematic for a IGM interpretation, due to the unrealistically small length scales required in the IGM for $\sim\text{ms}$ scattering (Luan & Goldreich, 2014).

In this chapter we propose a new non-cosmological but extragalactic solution to the FRB problem: supergiant pulses from newly formed pulsars in supernova remnants (SNRs). The dense ionized environment of the SNR can provide $300\text{-}2000 \text{ pc cm}^{-3}$ of dispersion if the pulses are observed within ~ 100 years of the core-collapse supernova. In our picture the large DM and scattering all come from the same place, and generically accounts for substantial Faraday Rotation and polarization angle swings. These features

were included to account for recent polarization measurements of a new FRB (Masui et al., 2015a) which may exhibit a polarization vector swing and whose RM is $\sim 2 \times 10^2$ rad m $^{-2}$. These are not expected in a cosmological interpretation of the DM.

3.4 Supernova Remants

Of order 10^{51} ergs of kinetic energy is released during a supernova, a fraction of which is converted into thermal energy after shock heating of the ejecta plasma. Though the shock-heated ejecta atoms are fully ionized after the explosion, the density is high enough that ionized atoms can soon recombine. This phase of low-ionization comes to an end when the remnant expands into the surrounding ISM, causing a reverse shock wave that reionizes the ejecta. Though this is the basic narrative, observations (Zanardo et al., 2014) as well as simulations (Potter et al., 2014) of SN 1987a have shown the morphological and ionization properties of SNRs in the decades and centuries after the explosion are nuanced and difficult to model. That said, in general the expanding shell left behind should be able to provide enough free electrons along the line-of-sight for unusually large dispersion measures. If we assume a toy model in which a sphere expands at v_{ej} , then the radius $R(t) \approx v_{\text{ej}}t$. Therefore the DM we expect can be calculated as,

$$\text{DM} \approx \frac{x_e M_{\text{ej}}}{m_p \frac{4\pi}{3} v_{\text{ej}}^2 t^2} \quad (3.1)$$

where x_e is the ionization fraction, M_{ej} is the ejecta mass, and m_p is the mass of a proton. Assuming $\sim 10 M_\odot$ of material is ejected at $v_{\text{ej}} \sim 3 - 8 \times 10^3$ km/s and an ionization fraction of $\sim 20\%$, the dispersion measure goes from several thousand pc cm $^{-3}$ immediately after the reverse-shock ionization, to several hundred pc cm $^{-3}$ after 50-100 years Zanardo et al. (2014). We point out that while the difference between a sphere of HII, which we have assumed, and a thin shell makes a small difference for DM, it could have a large effect of plasma frequency – something we discuss in section 3.5.

In the context of SNR 1987a, Zanardo et al. (2014) found that a possible pulsar could have DMs between 100-6000 pc cm⁻³, after ~ 25 years, though no compact object has yet been observed in that remnant.

Another potentially important feature of the SNR environment is its magnetic field. The exact magnitude of any detection of Faraday rotation has implications for the possible source location. For instance in the circumnuclear picture, one would expect RMs $\sim 10^{3-5}$ rad m⁻² (Pen & Connor, 2015a), similar to that of the Milky Way's Galactic center magnetar J1745-29. In the cosmological scenario, if the Faraday rotation came from the same place as the DM - namely the intergalactic medium - then we would only expect a few rad m⁻² of RM (Oppermann et al., 2015).

The Faraday effect rotates the polarization vector by an angle $\phi = \text{RM} \lambda^2$, where

$$\text{RM} = \frac{e^3}{2\pi m^2 c^4} \int_0^L n_e(l) B_{\parallel}(l) dl. \quad (3.2)$$

We can therefore make a rough estimate of the rotation measure of a remnant pulsar with dispersion measure DM. Using Burke & Graham-Smith (2014) we get,

$$\text{RM} \approx 0.81 \text{ rad m}^{-2} \times \frac{\langle B_{\parallel} \rangle}{1 \mu\text{G}} \cdot \frac{\text{DM}}{1 \text{pc cm}^{-3}}. \quad (3.3)$$

Though there is a large uncertainty in evolution of the magnetic field strength and added uncertainty in $\langle B_{\parallel} \rangle$ given B_{\parallel} is not necessarily positive, typical values in our Galaxy are 0.2 - 1 μG . For instance the Crab and Vela have $\sim 0.92 \mu\text{G}$ and $\sim 0.56 \mu\text{G}$, respectively. This gives RMs between $\sim 80 - 1200$ rad m⁻² for a SNR pulsar with FRB-like DMs, which is consistent with (Masui et al., 2015a).

3.4.1 Event Rates

The daily FRB rate has been estimated at $3.3_{-2.5}^{+5.0} \times 10^3$ sky⁻¹ (Rane et al., 2015). If we start from the local core-collapse supernova event rate, Γ_{CC} , and include objects out to

some distance d_{\max} , we expect the following daily FRB rate,

$$\Gamma_{\text{FRB}} \sim \frac{4}{3}\pi d_{\max}^3 \times \Gamma_{\text{CC}} \times \eta \tau_{\text{ion}} \gamma_{\text{GP}} \quad (3.4)$$

where τ_{ion} is the window in years when the SNR is sufficiently dense and ionized to provide the observed DMs, γ_{GP} is the daily rate of giant pulses above $\sim 10^{36}$ ergs, and η is the number of core-collapse supernovae that leave behind a visible pulsar. From Taylor et al. (2014) we know $\Gamma_{\text{CC}} \sim 3 \times 10^{-4} \text{ day}^{-1} (h^{-1}\text{Mpc})^{-3}$, so if we take d_{\max} to be $100 h^{-1}\text{Mpc}$ and $\tau_{\text{ion}} \sim 100$ years, we require one giant pulse every 10-20 days, assuming one fifth of this SNe population leaves behind a visible pulsar. In Fig. 3.4.1 we show the event rate as a function of distance, varying two parameters: the effective high-DM window and the rate of giant pulses.

From Fig. 3.4.1 we can see even in our most conservative estimate, when the SNR only has a 25 year window and emits giant pulses once every 100 days, the volume necessary for the highest daily FRB rate is still non-cosmological. By this we mean the DM contribution from the IGM is less than $\sim 200 \text{ pc cm}^{-3}$. If the SNR FRBs are within a hundred $h^{-1}\text{Mpc}$ then DM_{IGM} is less than $\sim 10\%$ of the total dispersion of a typical burst.

If FRBs really are giant pulses then they should repeat stochastically, and while none of the radio follow-ups for observed sources has seen an FRB repeat, this could be because they have not observed for long enough. We point out that FRB 140514, the first burst observed in real-time, was found during a follow up observation of FRB 110220 and the two were found within a beam-width of one another. FRB 140514 had a lower DM than 110220 by 380 cm pc^{-3} , and though Petroff et al. (2015a) show that it was not very unlikely that one would find a new FRB given their integration time, if it were the same source our model could explain the discrepancy. Indeed, a reanalysis by Maoz et al. (2015) found that the two bursts were far more likely to be the same repeating source than had been previously claimed. Given FRB 110220 would have been emitted over

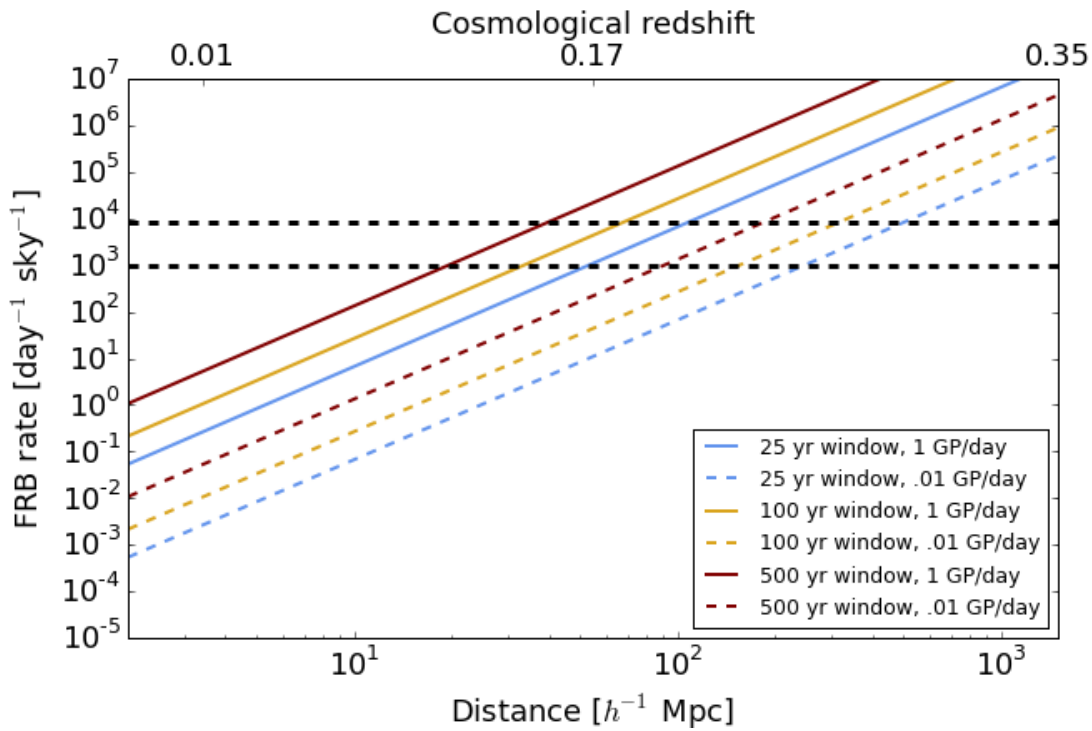


Figure 3.1: Daily FRB rate per sky based on local core-collapse supernova event rate, plotted against distance. We assume early in the pulsar's life there is a window, either 25, 100, or 500 years when the SNR can provide a large enough electron column density to explain the high DMs of the observed bursts. We also include a rate of giant pulses of either one per day or one per hundred days. We have assumed 20% of core-collapse supernovae leave behind a visible pulsar. The horizontal black lines are the 99% confidence bounds for the FRB rate found by Rane et al. (2015).

three years earlier, we would expect its DM generically to be higher, but the amount would depend on the inner structure of the SNR and its expansion speed. We discuss repetition further in section 3.5.

3.4.2 Young SNR Pulsars

About a dozen pulsars in our Galaxy are known to emit extremely energetic, short duration radio pulses which can be many orders of magnitude brighter than the pulsar’s regular emission. Some of these objects exhibit a rare tail of *supergiant* pulses, whose brightness temperatures exceed the Planck temperature, $\gtrsim 10^{32}$ K (Cordes et al., 2004), which we will take as a working definition of *supergiant*. Indeed the largest known brightness temperature, T_b , in the universe came from a giant pulse from the Crab, with $T_b \sim 2 \times 10^{41}$ K (Taylor et al., 2014). Though there are only ~ 100 hours of published giant pulse data from the Crab, it is known that the supergiant pulse tail does not obey the standard power-law fall off in amplitude (Mickaliger et al., 2012).

Given the relatively high frequency of core-collapse supernovae in the local universe, the young rapidly rotating pulsars such events leave behind could emit giant pulses bright enough to be observed at hundreds of megaparsecs. These supergiant pulses would require 10^{36-37} ergs of output, assuming and observed flux density of 0.3-5 Jy and ~ 500 MHz of bandwidth over 1 ms. Though this is \sim billions of times brighter than an average pulse, it is negligible compared to a pulsar’s total rotational energy, $E_{\text{rot}} \sim 10^{49-50}$ ergs and even the pulsar’s spin-down luminosity. We also point out that given its relative proximity, this model requires a couple orders of magnitude less energy than cosmological FRBs, located beyond a Gpc.

The polarization properties of giant pulses are also consistent with those of observed FRBs. Giant pulses are known to be highly polarized, switching between strong Stokes V and purely linearly polarized states often in an unpredictable way. The only published FRB prior to Masui et al. (2015a), with full-pol information was FRB 140514 and was

Location	Model	Galactic scintillation	Faraday rotation	$\frac{d\ln N_{\text{FRB}}}{d\ln S_\nu}$	Counterpart	DM range (pc cm $^{-3}$)	Pol angle swing
Cosmological ($\gtrsim 1h^{-1}\text{Gpc}$)	Blitzars	×	$\lesssim 7 \text{ rad m}^{-2}$?	gravitational waves	300-2500	×
	Merging COs	×	$\lesssim 7 \text{ rad m}^{-2}$?	type Ia SNe, X-ray, γ -ray	300-2500	×
	Primordial BHs	×	$\lesssim 7 \text{ rad m}^{-2}$?	$\sim \text{TeV}$	300-2500	×
	Magnetar flare	×	$\lesssim 7 \text{ rad m}^{-2}$?	$\sim \text{ms TeV}$ burst	300-2500	✓
Extragalactic, local ($\lesssim 200h^{-1}\text{Mpc}$)	Edge-on disk	✓	50-500 rad m $^{-2}$	-3/2	?	10-2000	?
	Nuclear magnetar	✓	$10^{3-5} \text{ rad m}^{-2}$	-3/2	none	10-3000	✓
	SNR pulsar	✓	$20-10^3 \text{ rad m}^{-2}$	-3/2	archival CC SNe or nearby galaxy	10^2-10^4	✓
Galactic ($\lesssim 100 \text{ kpc}$)	flaring MS stars	✓	RM_{gal}	-3/2	main sequence star	$\gtrsim 300$	×
Terrestrial ($\lesssim 10^5 \text{ km}$)	RFI	×	$\lesssim \text{RM}_{\text{ion}}$	$\begin{cases} -1/2 \text{ if } 2D \\ -3/2 \text{ if } 3D \end{cases}$	none	?	×

Table 3.1: This table summarizes a number of FRB models by classifying them as cosmological, extragalactic but non-cosmological, Galactic, and terrestrial. The seven columns are potential observables of FRBs and each row gives their consequence for a given model (Blitzars (Falcke & Rezzolla, 2014), compact object mergers (Mickaliger et al., 2012; Totani, 2013), exploding primordial blackholes (Barrau et al., 2014), bursts from magnetars (Lyubarsky, 2014), edge-on disk galaxies (Xu & Han, 2015), circumnuclear magnetars (Pen & Connor, 2015a), supernova remnant pulsars, stellar flares (Loeb et al., 2014), and terrestrial RFI (Hippke et al., 2015)). For the latter, we subdivide the RFI into planar RFI (2D) coming from the earth's surface, and 3D RFI coming from objects like satellites. Since scintillation only affects unresolved images, cosmological sources that are not scattered near the source will not scintillate in our Galaxy, while non-cosmological sources whose screens are intrinsic will. For Faraday rotation and scintillation we assume the RM and SM comes from the same place as the DM, e.g. the IGM for cosmological sources, though such models could introduce a more local Faraday effect or a scattering screen. Even though all models have to explain the observed $375\text{-}1600 \text{ pc cm}^{-3}$, some models predict a wider range of DM. For instance, in the circumnuclear magnetar or edge-on disk disk scenarios there ought to be bursts at relatively low DM that simply have not been identified as FRBs. In our supernova remnant model DMs should be very large early in the pulsar's life, though this window is short and therefore such high DM bursts would be rare.

found to have $\sim 20\%$ circular polarization and no detectable linear polarization (Petroff et al., 2015a). If FRBs were coming from a pulsar-like emission mechanism, one might see nearly pure Stokes V or linear-pol states. Another consequence of pulsar-like emission is that FRBs could exhibit polarization angle swings over the burst duration, which may have been observed by Masui et al. (2015a). Unfortunately, to date all other published FRBs were detected with systems that recorded only Stokes I.

3.5 Predictions

In table 1 we summarize the observational consequences of ours and several other models as best we can. As one might expect, the most striking differences in predictions has to do with the distance of FRBs, for example the cosmological FRB models differ mainly in their expected counterpart and not much else.

The young SNR pulsar model makes several predictions that will be addressed with more data, particularly with full polarization observations and large field-of-view surveys. The latter will provide a large sample of FRBs whose flux and DM statistics can give us information about their location. Since in the SNR FRB picture most of the DM is intrinsic, the sources do not need to be at cosmological distances. This means the flux distribution is given by a Euclidean universe that is only weakly dependent on DM, $N(>S) \propto S^{-3/2}$, assuming the bursts are standard candle-like. Wide-field surveys like CHIME (Bandura, 2014) (whose FRB back-end will observe steadily for several years), UTMOST¹, or HIRAX could observe as many as $\sim 10^{3-4}$ per year, which would allow for detailed population statistics. An instrument like CHIME will not only give us large numbers of DMs and fluxes, but will also allow us to measure various polarization properties and frequency scintillation.

Since we have proposed that FRBs come from young pulsars in SNRs, it is possible that the corresponding supernova was observed in recent decades in the optical. If the

¹<http://www.caastro.org/news/2014-utmost>

pulsars were younger than \sim 60 years old they could be localised at the \sim arcsecond level and matched against catalogued type II supernovae, though we would need a large sample of FRBs given the incompleteness of recorded supernovae. With current data the location of FRBs has been too poorly constrained to say anything meaningful about overlap with historic SNe or coincident galaxies; out to \sim 150 h^{-1} Mpc there are a number of galaxies in a Parkes beam and therefore one would expect as many supernovae anyway in the last century, even though it would unlikely have been observed. However better localisation or a cross-correlation between a large sample of FRBs and nearby galaxies could help support the non-cosmological extragalactic FRB hypothesis.

We also point out that while FRBs seem not to repeat regularly, it is not known that they never repeat. Though the statistics of giant pulses from local pulsars are mostly Poisson (Sallmen et al., 1999), it is possible that the supergiant pulses we require from very young SNR pulsars are not. If their statistics were of a Poisson process then there are already limits on the repeat rate, given the \sim 100 hours of follow up, however if their statistics were more like earthquakes, the brightest pulses could burst intermittently and turn off for extended periods. It is possible that FRBs could repeat every 5-500 days. If they were to repeat, it is possible that their DMs, RMs, and scattering properties could change noticeably on months/years timescales. Unlike standard pulsars whose RMs and DMs are constant to a couple decimal places, young SNR pulsars like the Crab and Vela have shown significant - and sometimes correlated - variation in such properties (Rankin et al., 1988). As discussed in section 3.4.1, FRB 140514 had a DM that was several hundred pc cm $^{-3}$ smaller than FRB 110220 and the two were found within a beam-width of one another. Though this could have just been a spatial coincidence of two separate objects, our SNR FRB model could account for such a change in DM while other models (cosmological, edge-on galaxy, etc.) cannot.

We also predict that such repeated bursts could have vastly different polarization states, similar to the giant pulses from pulsars in the Galaxy. Another consequence of

polarized pulsar-like emission would be a polarization angle swing. Given the FRBs would be rotating, the angle of the linear polarization vector could change throughout the pulse – a phenomenon that is seen in many galactic pulsars, often repeatably (Becker et al., 2006). Therefore models that explain FRBs as rapidly rotating compact objects could predict a swing in the polarization angle throughout the burst.

Depending on the relationship between the giant pulse rate and SNR age and environment, there may exist a short window in the pulsar’s life when DMs are larger than could be achieved in the IGM at redshifts $z \lesssim 2.5$. Naïvely we would expect the average pulse energy to decay with time along with its period. It would be therefore possible, albeit rare, that an FRB have a DM of $\sim 10^4$ pc cm $^{-3}$. In general we expect the distribution of DMs to be peaked somewhere around the observed FRBs (500-800 pc cm $^{-3}$), but with weight at intermediate DMs when the ejecta has significantly expanded and at very high DMs. In several non-cosmological FRB models there should be a number of low-DM FRBs (Pen & Connor, 2015a; Xu & Han, 2015), which must be explained away with non-identification bias. However in our picture we do not expect the pulsar to emit supergiant pulses indefinitely and therefore we do not expect to be able to see these objects when the SNR has expanded and the DMs would be moderate. In the Katz (2015) treatment of the SNR FRB it is assumed that the supergiant pulse rate is time-independent, a scenario that the observed $\frac{d\log N}{d\log DM}$ has already cast doubt on. But since the DM distribution depends on birth spin rate and the dependence of luminosity with period, both of which are unknown, we do not attempt to predict it concretely. The Crab would need to emit giant pulses in excess of several GJy to be seen at the distances we are proposing - which is several orders of magnitude brighter than what has been observed - and we postulate that is because it is too old.

Beyond the varying DM distributions produced by the location, density, and time dependence of the dispersing electrons, their plasma frequency can give interesting constraints on the nature of FRBs. Since

$$\omega_p = \sqrt{\frac{n_e e^2}{m_e \epsilon_0}} \quad (3.5)$$

we expect FRBs dispersed by the diffuse IGM to have very low plasma frequencies while Galactic models, e.g. flaring stars, should predict large ω_p . This can be verified in precise measurements of the pulse arrival time as a function of frequency. If $k^2 c^2 = \omega^2 - \omega_p^2$, then the λ^2 arrival time dependence is only true in the limit where $\omega \gg \omega_p$. Therefore plasma frequency can be used to test FRB models by looking for deviations in the data. This probe was also pointed out by Katz (2015), who shows the dispersion index for $\Delta t \propto \nu^\alpha$ differs from -2 by $\frac{6\pi n_e e^2}{m_e \omega^2}$. In the SNR model a \sim 50 year SNR expanding at $\sim 3,000$ km s $^{-1}$ would have a plasma frequency of $\lesssim 10$ MHz and an arrival delay within 4×10^{-5} of -2.0 at 1.4 GHz, which is consistent with present measurements.

Another interesting path for studying extragalactic radio bursts, cosmological or otherwise, is scintillation. Only objects of small angular size scintillate, which is why stars twinkle and planets do not: turbulent cells in the ionosphere can resolve planets but not stars. The same is true for extragalactic objects scintillating in the Milky Way, where objects larger than $\sim 10^{-7}$ arc seconds do not scintillate at \sim GHz. This is why so few quasars scintillate (Dennett-Thorpe & de Bruyn, 2002).

While several explanations for this scintillation exist (Narayan, 1992; Pen & Levin, 2014), we are concerned with the observational effects and not the physics. Using Thompson et al. (1986) we can estimate the angular size of an extragalactic object,

$$\theta \approx \left(\frac{2c\tau (R_{\text{obj}} - R_{\text{sn}})}{R_{\text{sn}} R_{\text{obj}}} \right)^{1/2} \quad (3.6)$$

where R_{obj} is the distance to the source, R_{sn} is the distance to the screen, and τ is the scattering timescale. For the case of FRBs we take τ to be ~ 10 ms. In the cosmological

case, if the ms scattering were from an extended galactic disk along the line of sight (see McQuinn (2014)) halfway between us and the source, then the angular broadening of an object at 2 Gpc is ~ 150 microarcseconds. If the screen were within 1 kpc of the same object then the broadening is ~ 80 nanoarcseconds. Therefore scintillation from our own Galaxy should only occur for cosmological FRBs whose millisecond scattering is close to the source. For an SNR FRB the screen would have to be within a few hundred parsecs of the object, which we generically expect. We include this feature in table 1 where each column is estimated based on the medium that is causing the high dispersion measure, e.g. the IGM for cosmological models.

3.6 Conclusions

Evidence is emerging suggesting FRBs are not only extraterrestrial but extragalactic. Though the simplest interpretation of their high DMs is a cosmological one, we find this model less compelling in the light of past scattering measurements and potential Faraday rotation and pol-angle swing in a new FRB (Masui et al., 2015a). In this chapter we offered a more nearby solution. We have gone through a model in which FRBs are really supergiant pulses from extragalactic supernova remnant pulsars, within a couple hundred megaparsecs. The SNR environment is sufficiently dense and ionized to provide DMs $\gtrsim 500\text{pc cm}^{-3}$ as well as RMs $\gtrsim 50 \text{ rad m}^{-2}$, only the first of which could be replicated by the IGM.

The environment could also provide $\sim\text{ms}$ scattering at 1 GHz, as has been observed in Galactic SNR pulsars. That makes this picture self-contained in the sense that the young remnant environment can account for the dispersion and scattering measure seen in FRBs. It predicts a higher Faraday rotation than the IGM, but not as high as galactic centers. The repetition rate is related to the distance, and could be from days to years. By extrapolating Crab-like giant pulses back to the pulsar’s first century or so, we have

proposed that such objects can emit extremely energetic bursts sporadically. If these are similar to giant pulses from Galactic pulsars, they could be highly polarized, either linearly or circularly, and if they were to repeat their polarization state may change drastically. Given the object's rotating nature, polarization angles would be likely to swing during the pulse. The distinct polarization properties have been seen in at least one burst and may end up being generic properties of FRBs (Masui et al., 2015a).

3.7 Acknowledgements

We thank NSERC for support. We also thank Bryan Gaensler, Niels Oppermann, Giovanna Zanardo, and Chris Matzner for helpful discussions.

Chapter 4

Fast Radio Burst Statistics

This chapter was adapted from three separate papers published in the Monthly Notices of the Royal Astronomical Society that explored the statistics of FRBs. In (Connor et al., 2016c), or “FRB repetition and non-Poissonian statistics”, it was argued that FRBs may repeat with unusual statistics. Connor et al. (2016a), or “Constraints on the FRB rate at 700-900 MHz”, provided detailed constraints on the FRB rate below L-band, and in “The Euclidean distribution of Fast Radio Bursts” we discussed the best way of calculating $N(> S)$ (Oppermann et al., 2016).

4.1 Chapter Overview

In this chapter we discuss a number of statistical issues related to FRBs. Although the Lorimer burst was discovered in 2007, in 2013 there were still fewer than half a dozen detected events. That meant inference about the nature of FRBs based on their statistics was difficult, and early statistical claims seemed to us to over-reach. For example, Petroff et al. (2014) claimed that the absence of events in the lower-latitude components of the High Time Resolution Universe Survey (HTRU) compared to the higher-latitude region was significant at the level of 99.5%, based on four FRBs the high-lat region. Furthermore, this dearth at low latitudes was reportedly significant enough to require

something beyond heightened scattering and effective system temperature in the Galactic plane. This prompted explanations for why there might be so many more off the plane than near it (Macquart & Johnston, 2015). However, we found the discrepancy to be less severe by a factor of a few, and that even with five more events in the high-lat component of HTRU there is still less than a 2σ disagreement. This work is discussed in Sect. 4.5, as adapted from (Connor et al., 2016d).

We have also attempted to urge the community not to jump the gun on the nature and location of FRBs. Before FRB 121102, by far the most popular class of explanations for FRBs was the cosmological cataclysmic one. This is the scenario in which the IGM accounts for nearly all of the burst's DM, and the pulse is caused by a one-off event, like merging compact objects. Keane et al. (2016a), for example, interpreted diminishing radio emission from a galaxy at $z \approx 0.5$ (giving the DM they would expect), as an FRB host galaxy and afterglow from coalescing neutron stars. This claimed was later questioned by Williams & Berger (2016), who suggested this was AGN variability, and not a transient. Before the discovery of FRB 121102's repeat bursts, we suggested that the limits on repetition might be weakened if they repeated with non-Poissonian statistics, and that the repeating scenario ought not be ruled out (Connor et al., 2016f,d). We discuss this work in Sect. 4.3.

Another statistical approach to probing the location of fast radio bursts is to use their flux distribution $N(> S)$. We find in Sect. 4.6 that given the detected events at the time of this writing, the distribution of FRBs is consistent with a Euclidean one. A recent paper (Vedantham et al., 2016) has attempted to model the Parkes beam in order to infer information about the true brightness of bursts it has seen, and we will discuss this briefly in the conclusions.

Finally, calculating and discussing the event rate of FRBs requires some statistical care. In Sect. 4.4 we make the first estimate of the burst rate below 1.4 GHz. We also discuss the problems related to quoting an all-sky rate above a strict fluence threshold,

and instead offer a more direct method of predicting a rate for a given telescope. This work was first published in (Connor et al., 2016a).

4.2 Introduction

4.3 Rethinking the constraints on repetition

Though no source has been shown with certainty to repeat, the limits on repeatability of FRBs are still weak. Several models generically predict repetition, whether periodic or stochastic. Galactic flaring stars (Maoz et al., 2015), radio-bursting magnetars (Popov & Postnov, 2007; Pen & Connor, 2015b), and pulsar planet systems (Mottez & Zarka, 2014) all predict repetition with varying rates and burst distributions.

In Connor et al. (2015) it was suggested that supergiant pulses from very young pulsars in supernova remnants of nearby galaxies could explain the high DMs, Faraday rotation, scintillation, and polarization properties of the observed FRBs. We proposed that if the repetition of supergiant pulses were non-Poissonian (with a pink or red distribution) then one might expect several bursts in a short period of time. It is also worth mentioning that the statistics and repeat rates of FRBs could vary from source to source – even if they come from a single class of progenitors – so a long follow-up on an individual burst may not provide global constraints. In this chapter we will refer to stationary Poisson processes (expectation value, $\mu(t)$, is constant in time) as “Poissonian”. When we discuss non-Poissonian statistics we will be focusing on stochastic processes that are correlated on varying timescales. For example we will not discuss periodic signals, which are not Poissonian but have already been studied (Petroff et al., 2015c).

4.3.1 Flicker noise

Pink noise is ubiquitous in physical systems, showing up in geology and meteorology, a number of astrophysical sources including quasars and the sun, human biology, nearly all electronic devices, finance, and even music and speech (Press, 1978; Voss & Clarke, 1975). Though there is no agreed-upon mathematical explanation for this phenomenon (Milotti, 2002), fluctuations are empirically known to be inversely proportional to frequency for a variety of dynamical systems. This can be written as

$$S(f) = \frac{C}{f^\gamma} \quad \text{if } f_{\min} \leq f \leq f_{\max}, \quad (4.1)$$

where $S(f)$ is the spectral density (i.e. power spectrum), γ is typically between 0.5-2, and f_{\min} and f_{\max} are frequency cutoffs beyond which the power law does not hold. In this chapter we will describe these distributions as having flicker noise.

In the case of a time-domain astronomical source, this results in uniformity on short timescales, i.e. a burst of clustered events followed by extended periods of quiescence. If FRBs were to exhibit such flicker noise then their repetition would not only be non-periodic, but would also have a time-varying pulse rate and, more importantly, variance. Therefore the number of events seen in a follow-up observation would depend strongly on the time passed since the initial event.

In Petroff et al. (2015c) the fields of eight FRBs discovered between 2009 and 2013 were followed up from April to October of 2014, for an average of 11.4 hours per field. During this follow-up programme FRB 140514 was found in the same beam as FRB 110220, however the authors argue that it is likely a new source due to its lower DM. After its discovery, the field of 140514 was monitored five more times, starting 41 days later on 2014-06-24, without seeing anything. Under the assumption that 140514 was a new FRB that only showed up in the same field coincidentally and that the repeat rate is constant, Petroff et al. (2015c) rule out repetition with a period $P \leq 8.6$ hours and

reject $8.6 < P < 21$ hours with 90% confidence. However it is possible that one or both of those premises is invalid, so it is useful to explore the possibility of non-stationary repeat rate statistics and repeating FRBs with variable DM.

If the statistics of the FRB’s repeat rate were non-Poissonian and initial bursts from FRBs were to have aftershocks similar to earthquakes, then the non-immediate follow-up observations impose far weaker repeat rate limits than has been suggested. We constructed a mock follow-up observation of the eight FRBs whose fields were observed in Petroff et al. (2015c). We then asked how many bursts are seen to repeat if we do an immediate follow-up vs. a follow-up several years after the initial event at times corresponding to the actual observations carried out.

We run a simple Monte Carlo simulation with one sample per hour and a probability of 0.5 that a given sample has a burst in it. The repeat rate of once per two hours is chosen arbitrarily and should not affect the comparison. To get the $1/f^\gamma$ distribution we take an uncorrelated Gaussian time stream centred on 0 and move to Fourier space, then multiply by $f^{\gamma/2}$, which gives a power spectrum with the desired shape. We then inverse Fourier transform back to get the pink or red time stream. We then take samples with a positive value to contain a pulse and samples with a negative value to contain none.. In the stationary Poisson case, the rate of bursts in the immediate follow-up is the same as the multi-year follow-up since all times are statistically equivalent. However with flicker noise the variance is strongly time-dependent. If we imagine an object that repeated on average once per two hours, then if those pulses were Poisson-distributed the probability of seeing zero bursts in 11.4 hours or longer is ~ 0.007 . With pink noise one expects this roughly 20% of the time, since the system prefers either to be in “on” or “off” mode. If the average repeat period were more like 5-20 hours, then we would often see nothing in a multi-day follow-up observation that took place weeks or years after the initial event.

This is consistent with what Petroff et al. (2015c) saw, though the conclusions differ depending on the assumed statistics. In Fig. 4.1 we show a sample from this simulation

for three repeat distributions. The right panel shows how, if an FRB’s burst rate has long-term correlations ($1/f^\gamma$), the likelihood of a repeat is greatly increased if the follow-up observation is immediately after the initial event, rather than months or years after.

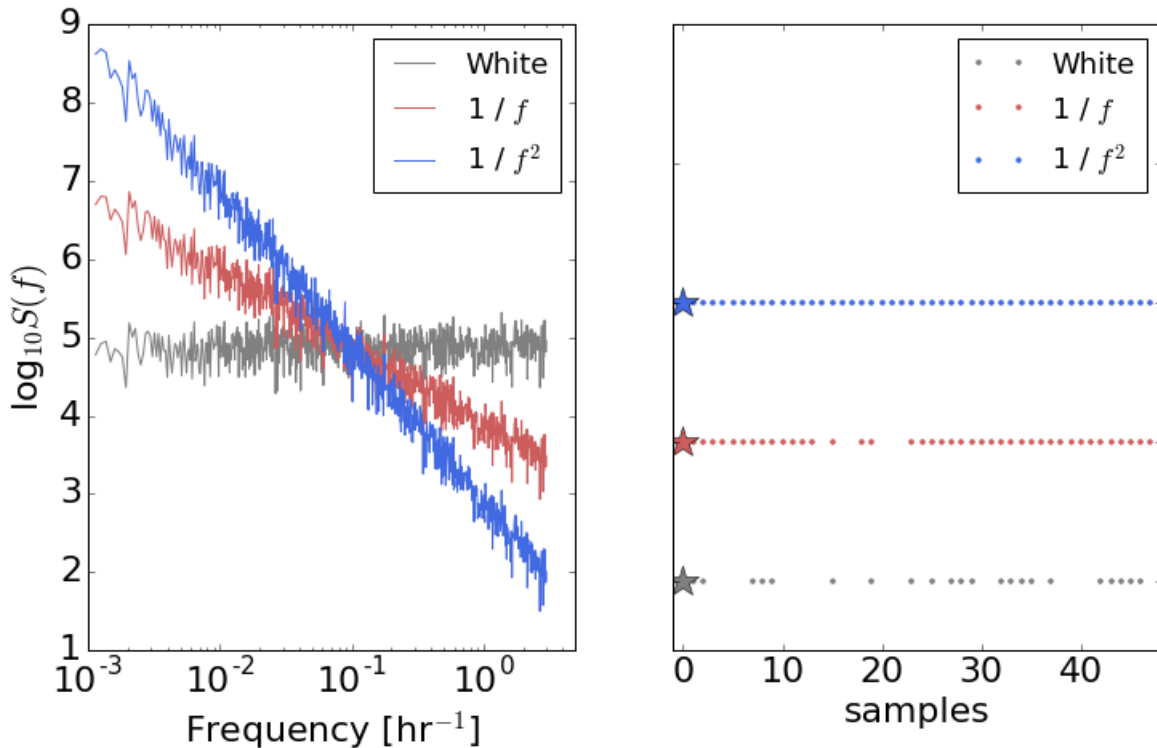


Figure 4.1: Realization of our mock follow-up Monte Carlo. *Left panel:* Power spectrum for pulse arrival times of a single FRB. Grey shows a flat spectrum, corresponding to the often assumed Poissonian repetition rate. The red and blue spectra show flicker noise, with pink ($1/f$) noise and Brownian ($1/f^2$) noise respectively. *Right panel:* We found the first “event” in our Monte Carlo (represented by a star) for the three different spectra and plotted their behaviour in the subsequent 48 hours of follow-up. Though the average probability over the whole simulation is 0.5 for each distribution, when we zoom in on this short period the strong time-like correlations in the $1/f^\gamma$ cases means there are many repetitions: they are in an “on” state at this time.

4.3.2 FRBs 110220 and 140514

Using the event rate of roughly $10^4 \text{ sky}^{-1} \text{ day}^{-1}$ from Thornton et al. (2013a), it was originally reported that the probability of seeing a new FRB in the field of 110220 during

the 85 hours of follow-up was 0.32 (Petroff et al., 2015a). It was then pointed out by Maoz et al. (2015) that this underestimated the coincidence by an order of magnitude, since they estimated the rate in any one of the 13 beams, while the new event occurred in the identical beam. The probability also dropped due to the updated daily event rate, given the Thornton et al. (2013a) estimate is now thought likely to be too high. In general we expect the true rate of FRBs to be lower than what is reported due to non-publication bias: If archival data are searched and nothing is found, it is less likely to be published than if something is found. That said, using the rate calculated by Rane et al. (2015) and following the procedure of Maoz et al. (2015), we find the likelihood of finding a new burst to be between 0.25-2.5%.

Given the relatively low probability of finding a new FRB in the same field and since there are models that predict burst repetition with variable DMs (Connor et al., 2015; Maoz et al., 2015) one can ask the question: If one FRB out of eight is found to repeat during 110 hours of follow-up (including extra time spent on 140514), what are the limits on the average repeat period? Another way of asking this question is what is the probability of some number of repetitions during the 110 hours, given a repeat rate. The answer to this question depends strongly on the power spectrum's shape. For the sake of example, if the average repeat rate is once per two hours, then the probability of one repeat or fewer in the Poisson case is effectively zero. With a pink distribution it is closer to 5%, even though the expected number would be 55. This is shown in Fig. 4.2, in which we plot the probability of seeing zero or one repeat burst (the two options for FRB 140514), given some average repetition period, P . We generate the pink distribution in the same way described in Section 4.3.1, using one-hour samples and a long-wavelength cutoff at 1.2 million hours. Though it was taken arbitrarily, the probability of seeing no bursts should depend only weakly on this cutoff. Since the variance scales logarithmically with this number, there is only roughly a factor of three difference in total power between our choice and $f_{\min} \sim$ an inverse Hubble time. While we

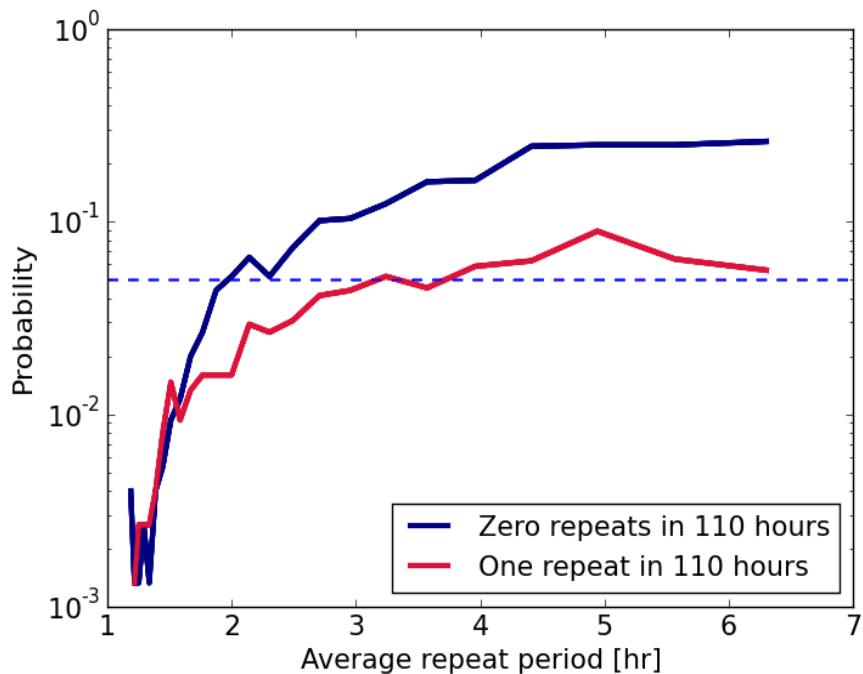


Figure 4.2: The probability of seeing zero (blue curve) or one (red curve) repeat burst in 110 hours of follow-up, assuming a $1/f$ distribution. The curves are derived from a simple Monte Carlo in which a pink distribution was generated with one sample per hour, and we asked how many bursts were seen in 110 samples. Thousands of 110-hour realizations were then averaged for each repeat period, P . Even with an average repeat rate of once every two hours, there is still a 5% chance (indicated by the dashed line) of seeing one or fewer bursts, despite the expected value of 55.

remain agnostic about the relationship between 140514 and 110220, with non-Poissonian repetition it is possible to have a relatively high repeat rate and to see either one or zero repeat bursts in several days of observation.

4.3.3 Repetition and total number of sources

If FRBs were found to repeat, their statistics and the average frequency of their repetition should affect the search strategy of upcoming surveys. For instance, if it were found that FRBs repeated, on average, five times a day, then the number of unique sources would be five times smaller than the per-sky daily event rate. This means the daily rate $3.3_{-2.5}^{+5.0} \times 10^3$ sky $^{-1}$ estimated by Rane et al. (2015) would be produced by only ~ 160 -1600 sources. In

this scenario there is no FRB in most pixels on the sky, which means one could integrate on most patches forever without seeing an event. An example of this strategy is the VLA millisecond search, in which $\sim 40\%$ of the time was spent at a single pointing, and almost three quarters of the time was spent at just three locations (Law et al., 2015). It is possible that pointing-to-pointing event rate variance contributed to their not seeing anything.

We therefore warn that deep surveys are at a disadvantage to those that sweep large regions of the sky (CHIME (Bandura, 2014), UTMOST¹, HIRAX) because the non-repeating scenario is unaffected; whereas shallow observations should not hurt the detection rate, no matter what their repetition. Ideally, a survey needs only to spend a few dispersion delay times on each beam before moving on.

4.4 FRB 110523 and sub-L-band statistics

To date, estimating the all-sky rate of FRBs has proven difficult, even at 1.4 GHz where most have been found (Lorimer et al., 2007b; Keane et al., 2012; Thornton et al., 2013a; Petroff et al., 2015a; Champion et al., 2015a; Spitler et al., 2014a). This is in part because of their unknown flux distribution and location within the radio telescope beam, as well as the low number of observed events. It is further exacerbated by the different specifications of the surveys that find them, whose disparate search algorithms, fluence completenesses, and sensitivity can affect their detection rate. Extrapolating to other frequencies is also difficult since spectral indices and the extent of scattering are still unknown.

Thornton et al. (2013a) searched about 25% of the High Time Resolution Universe (HTRU) survey data and found four FRBs. They estimated an all-sky daily rate of $1.0_{-0.5}^{+0.6} \times 10^4$ above ~ 3 Jy ms from 23 days of data and using a 0.55 deg^2 beam. The rate based on HTRU has since come down ($6_{-3}^{+4} \times 10^3 \text{ sky}^{-1} \text{ day}^{-1}$) with the discovery of

¹<http://www.caastro.org/news/2014-utmost>

five more FRBs in three times as much data (Champion et al., 2015a). Keane & Petroff (2015) also found a rate that was lower than the initial estimate, calculating ~ 2500 sky $^{-1}$ day $^{-1}$ after accounting for completeness factors like fluence sensitivity. Though the error bars are still significant, there is some convergence on the rate, and it now seems likely that there are thousands of such events each day at 1.4 GHz.

Event rate estimates at 1.4 GHz are converging, but strong rate constraints have not yet been made in other bands. The non-detection by UTMOST (an upgrade to the Molonglo Observatory Synthesis Telescope) (Caleb et al., 2016c) placed a 2σ upper limit on the number of bright events (10^3 events per sky per day above 11 Jy ms) after searching 467 hours at a fraction of its eventual sensitivity. FRB 110523 remains the only published event not found around 1.4 GHz. It was found near 800 MHz, where scattering or the intrinsic spectral index might have rendered this lower-frequency FRB unobservable. Kulkarni et al. (2015) argued that the steep blue spectrum seen in FRB 121102 (Spitler et al., 2014a) was indicative of free-free absorption, the optical depth of which scales as $\lambda^{2.1}$ and would make metre-wave bursts difficult to see. A greater concern comes from scattering. Sources broadened by scattering to ~ 10 ms at 1.4 GHz would be ~ 100 ms at 800 MHz, and a couple of seconds at 400 MHz, due to the λ^4 scaling of the scattering width.

Some surveys that could have great impact on FRB science are threatened by strong scattering. ALERT hopes to localize dozens of bursts with LOFAR after finding them with the large field-of-view (FoV) APERTIF (van Leeuwen, 2014; Verheijen et al., 2008), UTMOST will have ~ 8 deg 2 of sky coverage 24/7 at 843 MHz (Caleb et al., 2016c), and HIRAX², Tianlai³ and CHIME (400-800 MHz) could see 10^{2-4} per year, with the ability to write full polarization information (Bandura, 2014). However, their success depends on whether or not the rate of detectable FRBs is comparable to that at higher frequencies.

²<http://www.acru.ukzn.ac.za/~hirax/>

³<http://tianlai.bao.ac.cn/>

4.4.1 Implications for the flux distribution

FRB 110523 was found by searching data from the Green Bank Hydrogen Intensity Mapping (GBTIM hereon) survey (Chang et al., 2010; Masui et al., 2015b; Switzer et al., 2013). These data were taken with 1.024 ms cadence between 700-900 MHz using the GBT linearly-polarized prime-focus 800 MHz receiver, along with the GBT Ultimate Pulsar Processing Instrument (GUPPI) digital back-end. An effective DM range of 20-2000 pc cm⁻³ was then searched for FRBs. At each DM, the data were convolved with all possible lengths of top-hat windows up to 100 ms to search for peaks. The peaks were then compared to the root mean square (RMS) of the convolved time-stream, the ratio of which is what we will refer to as signal-to-noise ratio (SNR). The survey duration was 660 hours.

In order to test the observed FRB flux distribution, $N(F)$, we can apply a standard log(N)-log(F) test. We will consider only power-law distributions of form $N(>F) \propto F^{-\gamma}$. In a Euclidean Universe a population of sources that are uniformly distributed in space should have $N(>F) \propto F^{-3/2}$. This makes intuitive sense, since number counts ought to increase like the cube of distance, while the flux falls off as inverse squared distance.

With no FRBs found between the search algorithm’s detection threshold, 8σ , and 32σ , where FRB 110523 was found, we can test if this has any implications for the true flux distribution. The question we are trying to answer is “Having seen a single event, what is the probability that it has SNR greater than s for a given value of γ ?” . This is given by the ratio of integrals,

$$\beta \equiv \frac{\int_{s_{\min}}^{s_{\max}} N(s) ds}{\int_{s_{\min}}^{\infty} N(s) ds}, \quad (4.2)$$

which reduces to $\beta = \left(\frac{s_{\max}}{s_{\min}}\right)^{-\gamma}$ for $\gamma \neq 0$ and integrands of the form $N(s) \propto s^{-\gamma-1}$. This statistic is equivalent to the V/V_{\max} test that has been used to probe the underlying spatial distribution of quasars (Schmidt, 1968a) as well as gamma-ray bursts (Ogasaka

et al., 1991). Calculating β as a function of γ shows that steep distributions with $\gamma > 2.2$ are ruled out with 95% confidence by this single detection alone.

This is mathematically equivalent to the single-burst solution to a more general approach similar to the biased coin-flip scenario outlined by Connor et al. (2016e). If M_{high} FRBs are observed above a threshold SNR of s_{thresh} , with M_{tot} above s_{min} , and p is the relative probability of detecting an FRB in the high-SNR region, then

$$P(M_{\text{high}} | M_{\text{tot}}, p) = \binom{M_{\text{tot}}}{M_{\text{high}}} p^{M_{\text{high}}} (1-p)^{M_{\text{tot}} - M_{\text{high}}}, \quad (4.3)$$

where p is just $\beta(\gamma)$. Clearly this reduces to the previous result in the case where $M_{\text{high}} = M_{\text{tot}} = 1$.

4.4.2 How to discuss event rate

The simplest constraints one can make, given a set of observations, will be an expected event rate for a future survey with identical parameters. Transferring that rate to another survey or onto the sky requires care, and in both cases uncertainties are introduced that are hard to quantify. For this reason we start by calculating a rate for GBTIM in Sect. 4.4.3, which predicts how many FRBs are expected if an identical survey were to take place again. After that we discuss the implications for other comparable surveys, which should be fairly robust against things like burst-width sensitivity and the choice of fluence thresholds. In Sect. 4.4.5 we provide an all-sky rate, with several caveats, and discuss the meaning of such a value.

4.4.3 Burst rate

The rate of FRBs implied by 110523 will be independent of its observed brightness. The relevant quantity is the survey sensitivity, so s_{min} is the only flux scale that should show up in our rate estimate. For a true rate μ_0 above s_{min} , we would expect the number of

bursts, M , in a given survey above some SNR, s , to be

$$M_s = \mu_0 \Omega T_{\text{int}} \frac{N(>s)}{N(>s_{\min})}, \quad (4.4)$$

where Ω is the telescope's FoV and T_{int} is the time on sky. We use the rate above some SNR so that we can easily scale it to a rate prediction for a different survey without making any implicit assumption about the distribution of FRBs in flux, fluence, or duration. Similar to Eq. (4.2), this becomes

$$M_s = \mu_0 \Omega T_{\text{int}} \frac{s^{-\gamma}}{s_{\min}^{-\gamma}} \quad \text{for } \gamma > 0. \quad (4.5)$$

However, since we will not try to estimate an all-sky daily rate until Sect. 4.4.5, for now we will take T_{int} and Ω to be in units of the GBTIM on-sky time and beam-size. Therefore M_s should be thought of as the number of FRBs one would expect if the GBTIM were repeated.

Frequentist rate limits

If we regard the sky rate μ_0 as fixed, we can immediately write down the probability of observing M_{tot} FRBs above a SNR of s . It is simply given by the Poissonian distribution

$$P(M_{\text{tot}}|\mu_0) = \frac{M_{s_{\min}}^{M_{\text{tot}}} e^{-M_{s_{\min}}}}{M_{\text{tot}}!}, \quad (4.6)$$

where $M_{s_{\min}}$ is given by Eq. (4.5) for $s = s_{\min}$. Now we can ask which values of M_s make the observed value of $M_{\text{tot}} = 1$ unlikely. Choosing a threshold value of 5%, we can—in this sense—rule out expected event counts $M_{s_{\min}}$ outside of the range from 0.05-4.50 events per GBTIM-like survey, with a maximum likelihood value at 1.

Bayesian rate limits

From a Bayesian viewpoint, we want to look at the posterior for the expected number of detections, $M_{s_{\min}}$ rather than the likelihood. For simplicity we choose a flat prior on $M_{s_{\min}}$, which means that the posterior is again

$$\mathcal{P}(M_{s_{\min}} | M_{\text{tot}}) = \frac{M_{s_{\min}}^{M_{\text{tot}}} e^{-M_{s_{\min}}}}{M_{\text{tot}}!}. \quad (4.7)$$

Note that, although the posterior has the same functional form as the likelihood, it is to be read as a density in $M_{s_{\min}}$ rather than a probability for M_{tot} . Now we can calculate another 95% confidence interval, defined as the smallest interval I with the property $\int_I d\mu_0 \mathcal{P}(\mu_0 | M_{\text{tot}}) = 0.95$. We find for this 95% confidence interval $I = [0.24, 5.57]$ events for a GBTIM-like survey. From hereon we will quote the rate error bars based on the posterior. The posterior for μ_0 , which is the same as Eq. (4.7) multiplied by ΩT_{int} , is shown in Fig. 4.3.

4.4.4 Implications for other surveys

Though only one event was observed in the 660 hours of archival data, the fact that any burst was detectable in this band is significant. Some of the most important upcoming surveys for FRB science will observe below 1.4 GHz. UTMOST (Caleb et al., 2016c) will be on the sky 24/7 with an $\sim 8 \text{ deg}^2$ FoV and $18,000 \text{ m}^2$ of collecting area, observing at 843 MHz. ALERT hopes to localize dozens of FRBs by first detecting them with the large-FoV APERTIF (van Leeuwen, 2014; Verheijen et al., 2008) and then following up with roughly arcsecond resolution when they arrive several minutes later at LOFAR. Another survey for which FRB 110523’s discovery is relevant is CHIME, observing at 400–800 MHz. If the event rate in this band is comparable to the one at higher frequencies, then its large FoV and uninterrupted observing will make it by far the fastest FRB survey.

Since the rate of detection depends on an interplay of the underlying FRB flux and

scattering distributions with a survey’s thermal sensitivity, fluence completeness, and observing frequencies, the comparison of two surveys with similar specifications is by far the safest bet. CHIME has $\sim 8,000 \text{ m}^2$ of collecting area compared to GBT’s $\sim 7,850 \text{ m}^2$ and has 100 MHz of overlap with GBTIM. UTMOST will observe within the GBTIM band with similar sensitivity per steradian. Though others (Burke-Spolaor & Bannister, 2014a) have provided models for calculating inter-survey sensitivity based on sky pointing and temporal broadening, we compare only similar telescopes and adopt the simplest possible comparison based on known features of each instrument. Given how little is known about scattering properties and spectral indices, we provide only a skeleton model below; a more detailed calculation is beyond the scope of this paper.

A survey, Σ , that is similar to the GBTIM experiment will see N_Σ events per day based on the one detected burst in ~ 27.5 days at GBT. This is given by

$$N_\Sigma = \frac{1}{27.5} \left(\frac{G_\Sigma}{G_{\text{GBT}}} \frac{\langle T_{\text{GBT}}^{\text{sys}} \rangle}{\langle T_\Sigma^{\text{sys}} \rangle} \sqrt{\frac{B_\Sigma}{B_{\text{GBT}}}} \right)^\gamma \left(\frac{\Omega_\Sigma}{\Omega_{\text{GBT}}} \right) \text{ day}^{-1} \quad (4.8)$$

where B gives the survey’s bandwidth, G is the gain, and $\langle T^{\text{sys}} \rangle$ gives the pointing-averaged system temperature. For GBT we take the effective solid angle based on the full-width half max (FWHM) in power, giving $\Omega_{\text{GBT}} \sim 0.055 \text{ deg}^2$. We use 26.5 K for the sky-averaged system temperature, and a gain of 2 K Jy^{-1} .

As discussed above, in assessing the impact FRB 110523’s detection on other surveys, we want to avoid venturing into the unknown. For this reason we consider only the 100 MHz of overlap between CHIME and GBTIM, since that region is known to have a non-zero rate of observable FRBs. For things like beam size, we take the maximum possible FoV based on CHIME’s optics and let others adjust the effective solid angle accordingly; though the CHIME collaboration may search only a subset of their primary beam in order to optimize other aspects of their FRB survey, we will estimate the rate based on

a full beam.

We model CHIME’s primary beam at 750 MHz based on Shaw et al. (2015). A simple dipole beam in the aperture plane is propagated onto the sky by treating the reflector along the cylinder (north-south direction) as a mirror, and by solving the Fraunhofer diffraction problem in the east-west direction. As with GBT, we use only the beam within the half-max contour. This gives $\Omega_{\text{CH}} \sim 86 \text{ deg}^2$ in the middle of its band compared to $\Omega_{\text{GBT}} \sim 0.055 \text{ deg}^2$. Though this gives a ratio of ~ 1600 between the two telescope’s beam sizes, we remind the reader that this is an approximate solid-angle upper-limit for CHIME between 700-800 MHz. We then estimate its aperture efficiency as 50%, compared with 72% at GBT⁴, whose feed horn maximally illuminates its dish while minimizing ground spill, something that is difficult with CHIME’s dipole antennas. This makes $G_{\text{CH}} = 1.38 \text{ K Jy}^{-1}$. Finally, keeping with 26.5 K for GBT’s system temperature as before and using CHIME’s design system temperature of 50K (Bandura, 2014), we can write the maximum-likelihood value for the CHIME rate as

$$N_{\text{CH}} \approx 7.5 \left(\frac{50 \text{ K}}{T^{\text{sys}}} \right)^{1.5} \text{ day}^{-1} \quad (4.9)$$

assuming a Euclidean distribution. This means with a 50 K system temperature, CHIME could see between 2-40 (95%) bursts per day if it searches its whole FoV, based on the known non-zero rate above 700 MHz. With a more conservative sky-averaged system temperature $T^{\text{sys}} = 100 \text{ K}$, CHIME might expect between one every couple of hours and one every two days.

Caleb et al. (2016c) estimate the daily rate of UTMOST in a similar way, directly comparing their sensitivity with that of Parkes at 1.4 GHz. They estimate that they will see a burst once every several days. However, with our constraints on the rate between 700-900 MHz, we can recompute UTMOST’s detection rate based on the same band, once it reaches final sensitivity. We use $G = 3.6 \text{ K Jy}^{-1}$, $T^{\text{sys}} = 70 \text{ K}$, $B = 31.25 \text{ MHz}$,

⁴<https://science.nrao.edu/facilities/gbt/proposing/GBTpg.pdf>

and a factor of $1/\sqrt{2}$ for its single polarization, based on Caleb et al. (2016c). This gives $4.2_{-3.2}^{+19.6} \times 10^{-1}$ day $^{-1}$, or between a couple per day and one every couple of weeks. This is consistent with Caleb et al. (2016c).

Finally, we estimate rates for three smaller telescopes related to CHIME. We use $\gamma = 3/2$ and only the 100 MHz of overlap bandwidth with GBTIM, as before. CHIME’s Pathfinder, which is made of two 20×37 metre cylinders, has been commissioned over the last two years and now has a working beamforming back-end. If the single formed beam were on sky searching for FRBs at all times, one might expect to detect 0.4 – 9 per year, taking its beam to be $\Omega_{\text{PF}} = 0.62 \text{ deg}^2$ and $G_{\text{PF}} = 0.26 \text{ K Jy}^{-1}$. The 26 m John A. Galt Telescope, just ~ 150 m from the CHIME Pathfinder at the Dominion Radio Astrophysical Observatory (DRAO), could detect 0.1 – 3 each year, with $\Omega_{26} = 0.78 \text{ deg}^2$ and $G_{26} = 0.09 \text{ K Jy}^{-1}$. Another telescope to which a simple FRB back-end could be attached is the 46 m Algonquin Radio Observatory (ARO). This might yield 0.2 – 4.5 per year, using $\Omega_{\text{ARO}} = 0.25 \text{ deg}^2$ and $G_{\text{ARO}} = 0.29 \text{ K Jy}^{-1}$. Though none of these telescopes makes for a very fast survey, the cost of searching is quite small, and a coincident detection between DRAO and ARO could provide a sub-arcsecond localization.

4.4.5 All-sky daily rate

The standard method for estimating an all-sky rate given a set of observations is to first calculate the rate, μ_0 , for that survey — usually the observed number of FRBs divided by the beam size and the time on sky — and then to scale that based on the survey’s sensitivity threshold and a flux distribution index, γ . This threshold has typically been in fluence, a physically motivated quantity for FRBs, and is given by

$$H_{\min} = \frac{s_{\min} \langle T^{\text{sys}} \rangle \tau}{G \sqrt{m \tau B}}, \quad (4.10)$$

where $\langle T^{\text{sys}} \rangle$ is the pointing-averaged system temperature, as before, s_{\min} is the SNR threshold used in the search algorithm, G is the gain at beam centre, B is the bandwidth, m gives the number of polarizations, and τ is some timescale. If one then wants to quote the rate above, say, 3 Jy ms, then the rate becomes $\mu \times \left(\frac{H_{\min}}{3 \text{ Jy ms}} \right)^\gamma$.

One problem with this method is that it is not entirely obvious how to choose τ , and several groups have approached it differently. Keane & Petroff (2015) discuss some of these effects and decided to use the value at which their survey becomes fluence complete, 2 Jy ms, based on the maximum width to which they are sensitive. Rane et al. (2016) use sampling time, which is the minimum possible effective burst width. This will maximise the reported search sensitivity because it uses the lowest possible fluence limit, and therefore generically lowers the final rate estimate after scaling to a common fluence. A more exact approach is to quote the rate above some fluence curve $H \propto \sqrt{\tau}$ between τ_{\min} and τ_{\max} corresponding to the actual SNR threshold if white noise is assumed. This is similar to what Champion et al. (2015a) do, who quote their rate above a fluence range.

Since the primary goal of this paper is to compare between surveys, we do not attempt to derive a strict fluence threshold for GBTIM and to scale our all-sky rate based on it. Until the fluence and width distributions for FRBs are known along with a search algorithm's width response, the all-sky rate quoted for some incomplete region of fluence space is not overly useful. Instead, we calculate the rate above our true threshold, which is $s_{\min} = 8$ for DMs between 20-2000 pc cm $^{-3}$ and widths between one and two hundred milliseconds. A useful estimate of the rate is given by the maximum of Eq. (4.7), $\mu_0 = \frac{1}{\Omega T_{\text{int}}} \left(\frac{s}{s_{\min}} \right)^\gamma$, for $s = s_{\min}$. The all-sky rate for GBTIM above 8σ is then $2.7^{+12.4}_{-2.1} \times 10^4 \text{ sky}^{-1} \text{ day}^{-1}$, between 700-900 MHz. We plot the corresponding posterior in Fig. 4.3.

Though this value seems high, GBTIM is a sensitive survey, with $F_{\min} = 97 \text{ mJy}$ for a 3 ms pulse. Without making any concrete statements about our sensitivity in fluence space, we can get an idea of how this rate compares to the estimates from other surveys based only on thermal sensitivity. We can use the rate inferred from the 9 HTRU FRBs

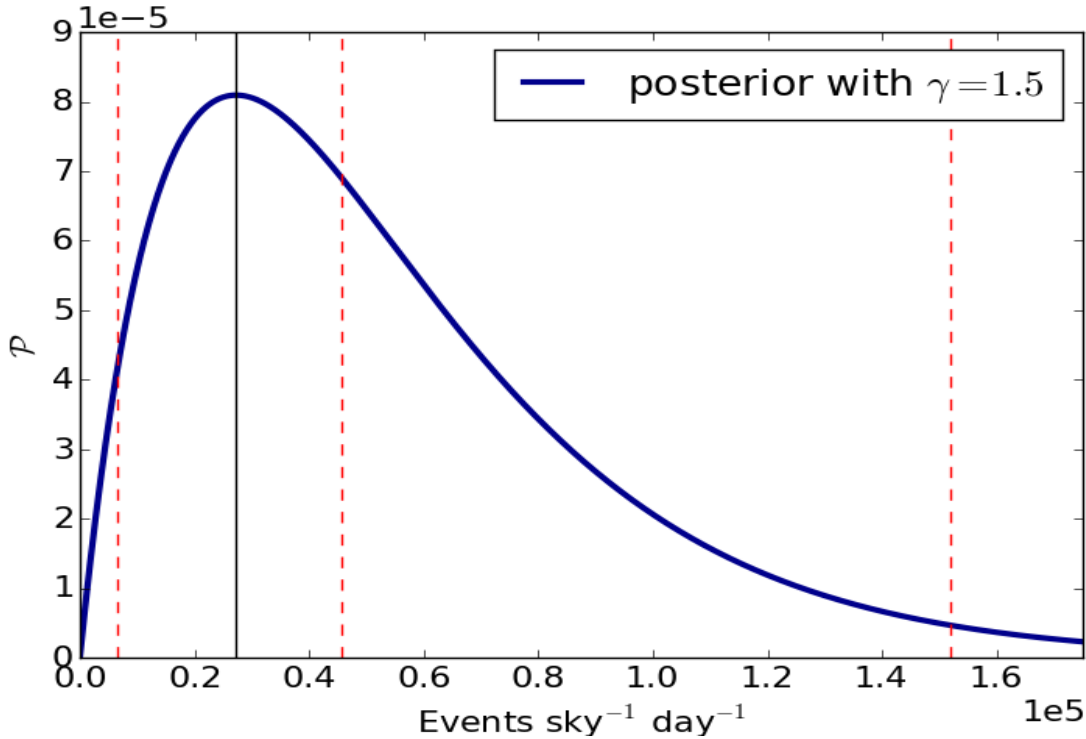


Figure 4.3: Posterior distribution for the all-sky daily rate based on seeing one burst in 27.5 days of data with a 0.055 deg^2 beam. This posterior is meant to be interpreted as the number of FRBs one would see if GBTIM-like surveys were able to observe the whole sky for a day, i.e. we have not scaled the rate based on fluence sensitivity for reasons described in Sect. 4.4.5. The maximum a posteriori value is denoted by the black vertical line, which is at $\sim 2.7 \times 10^4 \text{ sky}^{-1} \text{ day}^{-1}$. The two outside blue lines enclose 95% of the curve and the middle blue line denotes the median.

as a baseline (Champion et al., 2015a). If we assume the width completeness of various surveys is roughly similar, we can tether our rate to the HTRU one, and calculate a sensitivity ratio, r_s . Comparing Parkes and GBT, this will be

$$r_s = \frac{\langle T_{\text{H}}^{\text{sys}} \rangle}{\langle T_{\text{GBT}}^{\text{sys}} \rangle} \frac{G_{\text{GBT}}}{G_{\text{H}}} \sqrt{\frac{B_{\text{GBT}}}{B_{\text{H}}} \frac{s_{\text{min}}^{\text{H}}}{s_{\text{min}}^{\text{GBT}}}}. \quad (4.11)$$

Using $s_{\text{min}}^{\text{H}} = 10$, an average on-axis gain of $G_{\text{H}} = 0.64 \text{ K Jy}^{-1}$, $B_{\text{H}} = 340 \text{ MHz}$, and a 23 K system temperature (Keith et al., 2010a), we find $r = 2.60$. Our rate can then be multiplied by $r^{-\gamma}$, which gives $6.4_{-5.0}^{+29.5} \times 10^3 \text{ sky}^{-1} \text{ day}^{-1}$, assuming a Euclidean distribution.

This is an extrapolation of our rate estimate at 700-900 MHz to 1.4 GHz. It corresponds to the number of FRBs that HTRU should be detecting if the intrinsic rates of FRBs in the two frequency bands were the same. This extrapolated rate is indeed consistent with the rate observed by HTRU, which shows that the rate of FRBs detectable at low frequencies is not significantly lower than at 1.4 GHz, which was not previously obvious due to the threat of scattering and steep blue power-laws (Kulkarni et al., 2015). This result makes the aforementioned upcoming low-frequency surveys especially promising for FRB science.

This is also consistent with the non-detection upper-limit set by Caleb et al. (2016c), who found the rate to be below $10^3 \text{ sky}^{-1} \text{ day}^{-1}$ for one-millisecond 11 Jy bursts at the 2σ level. This was based on two surveys, one with 467 hours on sky, and another with 225 hours on sky at roughly twice the sensitivity. Comparing their time-weighted thermal sensitivity with GBTIM, we get $r_s \approx 10^2$, making our 95% upper-limit a few hundred per sky per day.

4.5 Latitudinal dependence

There is now evidence that the FRB rate is nonuniform on the sky, with fewer detectable events at low Galactic latitudes (Burke & Graham-Smith, 2014). However the statistical significance of this finding may be overestimated. Petroff et al. (2014) compute the probability of the disparity between the number of bursts seen in the high- and intermediate-latitude ($|b| < 15^\circ$) components of the High Time Resolution Universe survey (HTRU). They calculate the probability of seeing $N = 0$ in the intermediate latitude survey and $M = 4$ in the high-latitude, despite having searched 88% more data in the former, and they rule out the uniform sky hypothesis with 99.5% certainty. We would point out that in general $P(N|M)$ describes a very specific outcome, and it would be more appropriate to include all outcomes equally or more unlikely. That number might

also be multiplied by two, since if the survey found four intermediate-latitude FRBs and zero high-lat ones, we would ask the same question.

But a simpler approach to this problem would be analogous to a series of coin flips. If a coin were flipped four times, the probability of seeing all heads is 1/16, or 6.25%. This is a factor of six higher than the analogous analysis of Petroff et al. (2014). We can test the null hypothesis that the coin is fair, and using the binomial statistic would conclude that the outcome is consistent with a fair coin at 95% confidence, differing from the conclusion of Petroff et al. (2014). In the FRB case the Universe is flipping a coin each time a new burst appears, with some bias factor due to things like different integration times. HTRU has since reported five more bursts in the high Galactic region, but using a dataset that spent ~ 2.5 times more time at high latitudes. Below we try and quantify the likelihood of this.

If one wants to compare two statistical hypotheses, then the claims of each should be treated as true and their likelihood discrepancy should be computed. In the case of testing the abundance of FRBs at high latitudes, the sky should be partitioned into high and low regions a priori (e.g., the predefined high-latitude HTRU and its complement). The rate in both regions is then taken to be the same, and the likelihood of a given spatial distribution of observed sources can be calculated. This situation is naturally described by a biased binomial distribution with a fixed number of events. Suppose a total of K FRBs are observed in a given survey. We can ask the question, what is the probability of seeing M events in the high region and $(K - M)$ events in the lower region? This probability can be calculated as

$$P(M|K,p) = \binom{K}{M} p^M (1-p)^{K-M}, \quad (4.12)$$

where p is the probability that an event happens to show up in the high region. In a survey where more time is spent on one part of the sky than the other, $p = \alpha/(\alpha + 1)$, where α is the ratio of time spent in the high-latitude region vs. the intermediate region.

In the case of the HTRU survey, $K = 9$ and since none were found in the low-latitude region, $M = 9$. Roughly 2500 hours were spent searching the upper region and ~ 1000 hours were spent at $|b| < 15^\circ$, giving $\alpha = 2.5$. Using Equation 4.12, this outcome is only $\sim 5\%$ unlikely.

The problem is given a quasi-Bayesian treatment by Petroff et al. (2014), which gives the following.

$$P(N|M) = \alpha^N(1+\alpha)^{-(1+M+N)} \frac{(M+N)!}{M!N!} \quad (4.13)$$

This gives a probability of $\sim 3.5\%$, using all nine FRBs. This method is Bayesian in the sense that they marginalize over the unknown rate and calculate a likelihood, but they then calculate a confidence and do not look at a posterior.

The most obvious difference between the approach we have offered (biased coin-flip) and the quasi-Bayesian method is that we take $M + N$ to be fixed. It follows to ask whether or not we *should* regard the total number of FRBs as “given”? We believe the answer is yes, since this is one of the few quantities that we have actually measured, along with M and N . What we are really trying to infer is how much larger μ_{high} is than μ_{low} , so these rates should not be marginalized over.

To consider only the likelihood can give misleading results. For example, as more and more FRBs are detected, the likelihood of the particular observed values for N and M will become smaller and smaller, due to the sheer number of possible tuples (N, M) . To decide whether or not there is evidence for FRBs to occur with a higher probability at high latitudes, we can instead use the formalism of Bayesian model selection. This formalism does not aim to rule out a particular model, it only compares the validity of two models. For this, we formulate two specific models, Model 1 in which we assume that $p_1 = \alpha/(1+\alpha)$ as above (i.e. uniform rate across the sky), and Model 2 in which we regard p as a free parameter, equipped with a flat prior between 0 and 1. The model selection will then be based on the comparison of the posterior probabilities for the two

models,

$$\frac{P(\text{Model 1}|M, K)}{P(\text{Model 2}|M, K)} = \frac{P(M|\text{Model 1}, K)}{P(M|\text{Model 2}, K)}, \quad (4.14)$$

where we have assumed equal prior weights for the two models. Using the binomial likelihood, Eq. (4.12), and marginalizing over the unknown probability p in the case of Model 2, this ratio is easily calculated to be

$$\frac{P(M|\text{Model 1}, K)}{P(M|\text{Model 2}, K)} = (K+1) \binom{K}{M} p_1^M (1-p_1)^{K-M}. \quad (4.15)$$

For the observations discussed above with $M = K = 9$ and $\alpha = 2.5$, we find a ratio of 0.48, so there is no strong preference for either of the two models.

4.6 Is the distribution Euclidean?

In the simple constant-density Euclidean model, the power-law behaviour of Eq. (??) is not only valid for the flux densities, but also for any other observable that depends linearly on flux density. One example would be the fluence

$$\begin{aligned} F &= \int dt S(t) \\ &= S \tau, \end{aligned} \quad (4.16)$$

where τ is the duration of a burst and S is the average flux density within the interval of length τ . Another example is the observed signal-to-noise ratio, which depends on the flux density of the burst, its duration, and of course on properties of the telescope and the survey. In many cases it can be approximated as

$$s \approx K S \tau^{1/2}, \quad (4.17)$$

where we include all instrumental properties in the constant K (e.g., Caleb et al., 2016a). The detection of an FRB is always subject to a sensitivity cutoff in signal-to-noise, and not in flux density or fluence. This makes the statistics of flux density and fluence more complicated than the statistics of the signal-to-noise ratio s and we choose to cast all equations in terms of s . Note that, as is common in the field, we use the term signal-to-noise ratio to mean the amplitude of the FRB signal plus noise, divided by the standard deviation of the noise, which can be approximately determined empirically for each search window length τ .

We derive the necessary statistical methodology in the following section, discuss the data that we use and show our results in Sect. 4.8. We conclude with a discussion in Sect. ??.

4.7 Methodology

4.7.1 Likelihood for the observed signal-to-noise ratios

Clearly some information on the parameter α is contained in the distribution of observed signal-to-noise ratios. If we assume a value for α and suppose that a survey with a given signal-to-noise threshold s_{\min} detects an FRB, then the likelihood for its signal-to-noise ratio to be s is, according to Eq. (??),

$$\mathcal{P}(s|s_{\min}, \alpha) = \begin{cases} \frac{\alpha}{s_{\min}} \left(\frac{s}{s_{\min}}\right)^{-(\alpha+1)} & \text{if } s \geq s_{\min} \\ 0 & \text{else} \end{cases}. \quad (4.18)$$

If the survey detects n independent FRBs then the joint likelihood for their signal-to-noise ratios is simply the product of the individual ones.

For N different surveys, each detecting n_1, \dots, n_N FRBs, the situation is the same, except that we have to take into account that each survey has a different detection threshold s_{\min} . If we denote the observed signal-to-noise value of the i -th FRB in the

I -th survey as $s_{I,i}$, the $(n_1 + \dots + n_N)$ -dimensional vector of all these observed values as \vec{s} , the N -dimensional vector of all threshold signal-to-noise values as \vec{s}_{\min} , and the N -dimensional vector of the numbers of detections in each survey as \vec{n} , the complete likelihood becomes

$$\mathcal{P}(\vec{s}|\vec{n}, \vec{s}_{\min}, \alpha) = \prod_{I=1}^N \prod_{i=1}^{n_I} \mathcal{P}(s_{I,i}|s_{\min,I}, \alpha). \quad (4.19)$$

This is easily calculated and we will do so in Sect. 4.8. In the following we will refrain from mentioning \vec{s}_{\min} explicitly in the notation of probabilities and imply that all survey properties are always fixed.

Note that the combination $(s/s_{\min})^{-\alpha}$ for $\alpha = 3/2$ corresponds to the ratio of the volume interior to the FRB and the volume in which this particular FRB could have been detected by the survey, V/V_{\max} , for a constant source density in three-dimensional Euclidean space. The likelihood we are using here to constrain α is thus closely related to the V/V_{\max} -test used in many contexts to check for deviations from a constant density for a source population (e.g., Schmidt, 1968b).

4.7.2 Likelihood for the number of observed FRBs

In addition to the information contained in the signal-to-noise ratios of the observed bursts, some information is also contained in the numbers of bursts detected by different surveys. For any one survey, the number of detected FRBs puts constraints on the rate of FRBs occurring above the detection threshold of that survey. This rate can be rescaled to a different survey with a different detection threshold and confronted with the observed number of bursts for that survey. However, the rescaling depends on the parameter α and thus the number of bursts detected by two or more surveys puts constraints on α .

To include these constraints in our analysis we introduce the FRB rate explicitly as an unknown parameter. Since the rate observable by a given survey depends on various properties of the survey, we define the rate r_0 occurring above the detection

threshold of a hypothetical survey described by a system temperature $T_{\text{sys},0} = 1 \text{ K}$, a gain $G_0 = 1 \text{ K Jy}^{-1}$, $n_{\text{p},0} = 2$ observed polarizations, a bandwidth $B_0 = 1 \text{ MHz}$, and a signal-to-noise threshold $s_{\min,0} = 1$. As explained by Connor et al. (2016b), the FRB rate above the detection threshold of the I -th survey is then a rescaled version of this rate, namely

$$\begin{aligned} r_I &= r_0 \left(\frac{T_{\text{sys},I}}{T_{\text{sys},0}} \frac{G_0}{G_I} \sqrt{\frac{n_{\text{p},0} B_0}{n_{\text{p},I} B_I}} \frac{s_{\min,I}}{s_{\min,0}} \right)^{-\alpha} \\ &= r_0 \left(\frac{T_{\text{sys},I}}{G_I} \sqrt{\frac{2 \text{ MHz}}{n_{\text{p},I} B_I}} s_{\min,I} \text{ Jy} \right)^{-\alpha}. \end{aligned} \quad (4.20)$$

The expected number of FRBs detected by the I -th survey will then be

$$M_I = r_I \Omega_I T_I, \quad (4.21)$$

where Ω_I is the angular size of the survey's field of view and T_I is the time spent surveying. The likelihood for the actual number of FRBs observed in this survey is then a Poissonian distribution with this expectation value,

$$P(n_I | r_0, \alpha) = \frac{M_I^{n_I}}{n_I!} e^{-M_I}. \quad (4.22)$$

For N surveys the complete likelihood again becomes a product of the likelihoods for the individual surveys,

$$P(\vec{n} | r_0, \alpha) = \prod_{I=1}^N P(n_I | r_0, \alpha), \quad (4.23)$$

and can be used to put constraints on the distribution of flux densities via the parameter α , as well as on the overall rate of FRBs, here parameterized as the rate above the detection threshold of our hypothetical survey, r_0 .

4.7.3 Posterior

To get the complete set of constraints on the distribution of flux densities, both from the observed signal-to-noise ratios and from the detection numbers of different surveys, we combine the results of Sects. 4.7.1 and 4.7.2. We write the joint likelihood for the number of observed FRBs and their signal-to-noise ratios as

$$\begin{aligned}\mathcal{P}(\vec{s}, \vec{n}|r_0, \alpha) &= \mathcal{P}(\vec{s}|\vec{n}, r_0, \alpha) P(\vec{n}|r_0, \alpha) \\ &= \mathcal{P}(\vec{s}|\vec{n}, \alpha) P(\vec{n}|r_0, \alpha).\end{aligned}\quad (4.24)$$

If we assume flat priors for r_0 and for $\alpha > 0$, this likelihood is proportional to the joint posterior for the parameter α and the rate r_0 .

The likelihood for observed fluxes within a survey obviously only gives us constraints if the survey has in fact detected at least one FRB. Note, however, that we can in principle include surveys without FRB detection by setting

$$\mathcal{P}(\vec{s}|n = 0, s_{\min}, \alpha) = 1 \quad (4.25)$$

and thus still use them to constrain the parameter α via their implications on the FRB rate above their detection thresholds. Similarly, the numbers of FRBs detected by different surveys only have implications for the parameter α if we assume that the surveys observe the same source population, described by the same rate r_0 . This assumption will in general be violated if different surveys have different frequency coverage or different observational strategies. Specifically, the observations of a deep and narrow survey will in general not be described by the same statistics as those of a shallow and wide survey, as explained by Connor et al. (2016d). Care is thus warranted when comparing detection numbers of qualitatively different surveys. Such an attempt will require more parameters

or simply setting

$$P(n|r_0, \alpha) = 1 \quad (4.26)$$

for all surveys that are not expected to be described by r_0 .

4.8 Data and results

We make use of 15 observed FRBs from seven surveys. For definiteness, we list all values used in our calculation in Tables 4.1 and 4.2. For the likelihood of the numbers of detected FRBs, we only make use of two dedicated pulsar surveys with well-defined characteristics, namely the High Time Resolution Universe Pulsar Survey (HTRU; Keith et al. 2010b) at the Parkes telescope and the Pulsar ALFA survey (PALFA; Cordes et al. 2006) at the Arecibo Observatory. We choose these two surveys because for most other discovered FRBs it is hard to estimate the surveying period T that has been searched for FRBs, especially in the case of non-detections. The survey of Masui et al. (2015c) is similarly well-defined, but sensitive to different frequencies. We assume our parameter r_0 to describe the rate at frequencies around 1.4 GHz and do not want to make any assumption about the relation between this rate and the rate at 800 MHz, which is the central frequency of Masui et al. (2015c).

Even for HTRU and PALFA, the parameters needed in Eq. (4.20) are defined somewhat ambiguously. To avoid building complicated models of the telescopes and surveys, we generally opt for simple choices that can be made consistently for both surveys. Specifically, this means that we do not include any estimate of the sky temperature due to the Milky Way in the values we assume for the system temperature T_{sys} . For the gain G we use the arithmetic mean of the gains corresponding to the beam centres of the multi-beam receivers. The bandwidth B does not include frequencies deemed unusable by the surveying team and the angular size of the field of view Ω is intended to approximate the area within the half-maximum beam power. The resulting numerical values are listed in

Table 4.1: Parameters assumed for the FRB surveys. See Sect. 4.7.2 for the meaning of the symbols.

survey ¹	s_{\min}	T_{sys}/K	$G/(\text{K/Jy})$	n_p	B/MHz	$\Omega/(\text{deg}^2)$	T/h	n
HTRU [1]	10	23	0.64	2	340	13×0.043	3650	9
PALFA [2]	7	30	8.5	2	300	7×0.0027	886	1

¹ [1] Champion et al. 2015b; Thornton et al. 2013b; Keith et al. 2010b; [2] Spitler et al. 2014b; Cordes et al. 2006

Table 4.1. Other reasonable choices for these parameters will typically lead to deviations on the order of 10%. Note that the exact definition of each parameter does not impact the results as long as the same definition is used for all surveys that are being compared.

For the constraint on α coming from the likelihood for the observed signal-to-noise ratios, we can use all detected FRBs, as long as there is a well-defined signal-to-noise cutoff s_{\min} . Since we are investigating the population of sources, we are not including repeated bursts from the same object (Spitler et al., 2016). We also exclude the single burst detections by Lorimer et al. (2007a) and Keane et al. (2011), since no definitive value of s_{\min} can be determined. We list the values of s and s_{\min} that we use in Table 4.2.

After calculating the two-dimensional posterior for α and r_0 , we derive the final constraint on α by marginalising over r_0 and vice versa. These posterior distributions are shown in Fig. 4.4.

4.9 Conclusions

The search for FRBs with multiple surveys that have disparate sensitivities, frequency coverage, and survey strategy (not to mention non-publication bias) has made it difficult even to estimate a daily sky rate. That combined with the relatively low number of total FRBs observed has meant that dealing with their statistics can be non-trivial. In the case of repetition, we remind the reader that several non-cataclysmic models for FRBs are expected to repeat. In the case of supergiant pulses from pulsars, SGR radio flares,

Table 4.2: Parameters of each individual FRB used in our calculation. The signal-to-noise ratios s are taken from the FRBcat website¹ (Petroff et al., 2016).

name	s	s_{\min}	survey ²
FRB090625	30	10	[1]
FRB110220	49	10	[1]
FRB110626	11	10	[1]
FRB110703	16	10	[1]
FRB120127	11	10	[1]
FRB121002	16	10	[1]
FRB130626	21	10	[1]
FRB130628	29	10	[1]
FRB130729	14	10	[1]
FRB121102	14	7	[2]
FRB010125	17	7	[3]
FRB131104	30	8	[4]
FRB140514	16	10	[5]
FRB150418	39	10	[6]
FRB110523	42	8	[7]

¹ <http://www.astronomy.swin.edu.au/pulsar/frbcat/>

² [1] Champion et al. 2015b; Thornton et al. 2013b; Keith et al. 2010b; [2] Spitler et al. 2014b; Scholz et al. 2016; [3] Burke-Spolaor & Bannister 2014b; [4] Ravi et al. 2015; [5] Petroff et al. 2015b; [6] Keane et al. 2016b; [7] Masui et al. 2015c; Connor et al. 2016b

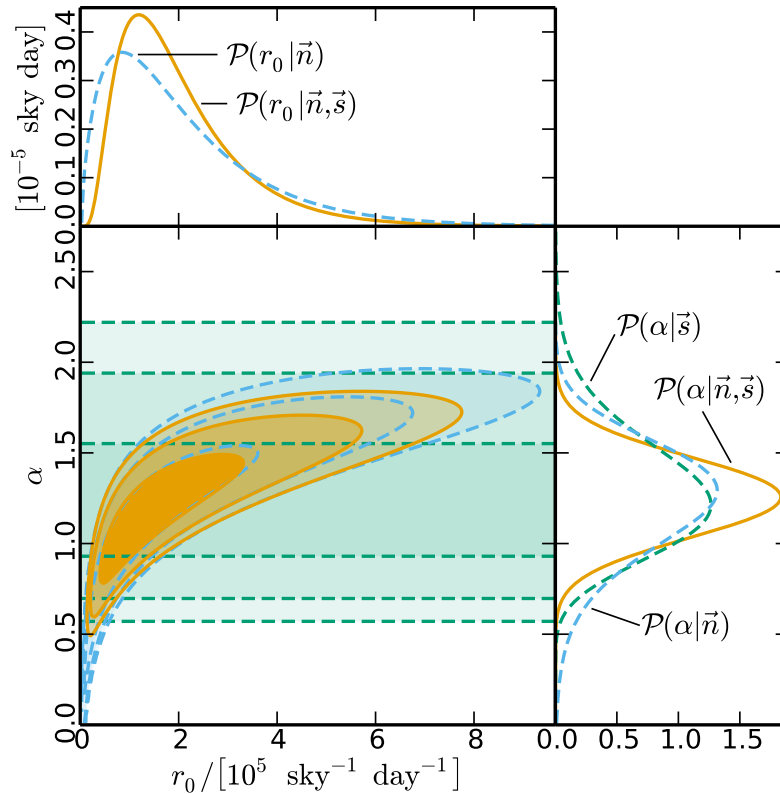


Figure 4.4: Posterior distribution for the parameter α describing the distribution of FRB flux densities and the FRB rate r_0 . The bottom left panel shows the two-dimensional posterior for both parameters, the smaller panels show the marginalised posteriors for each parameter individually. We show separate curves and contours for the constraints coming from the signal-to-noise ratios \vec{s} (green dashed), from the detection numbers \vec{n} (blue dashed), and their combination (orange solid). The contour lines show the 68%, 95%, and 99% confidence regions.

or even Galactic flare stars, it is possible that this repetition would be non-stationary and might exhibit strong correlations in time. We have shown that if the repetition had some associated flicker noise and its power spectrum were $1/f^\gamma$, then one should expect the repetition rate to be higher immediately after the initial FRB detection. Therefore follow-up observations to archival discoveries that take place years or months after the first event would not provide strong upper limits. This would also mean that if no burst is found in a given beam after some integration time, then it is unlikely that one will occur in the following integration, and therefore a new pointing should be searched. In

other words, shallow fast surveys would be favourable.

In Section 4.5 we offered a simple way of quantifying the latitudinal dependence of FRBs with a binomial distribution. This is akin to a biased coin flip, in which we ask “what is the probability of M bursts being found in one region and N bursts in its complement, given α times more time was spent in the former”. Like Rane et al. (2015) we argue that the jury is still out on the severity of the latitudinal dependence. With current data the preference for FRBs to be discovered outside of the plane seems consistent with sky-temperature effects and increased scattering, or even pure chance. Whether or not more sophisticated explanations (e.g., Macquart & Johnston 2015) are required remains to be seen. We also provided a Bayesian framework for model comparison, which can be used in the limit where large numbers of FRBs have been detected.

4.10 Conclusions

FRB 110523 is the only FRB to be observed below 1.4 GHz. Its detection is encouraging because there are several upcoming surveys below a GHz whose impact on FRB science is hard to overestimate, so long as the transients are detectable at low frequencies. In the next several years CHIME, HIRAX, Tianlai, UTMOST, and ALERT could increase the number of detected FRBs by orders of magnitude, provide polarization information and repetition statistics, and localize them. In this paper we have provided the first detailed bounded constraints on the FRB rate below 1.4 GHz.

We have shown two ways of estimating the rate given the detection of FRB 110523, one based on a frequentist hypothesis test, and the other done in a Bayesian framework. These give the same maximum-likelihood value, but somewhat different 95% confidence intervals. We have then used the GBTIM estimate to forecast rates for CHIME and UTMOST, explicitly only comparing surveys with similar specifications. We find CHIME could detect between 2 and 40 per day, given by $\approx 7.5 \left(\frac{50\text{K}}{T_{\text{sys}}}\right)^{1.5} \text{ day}^{-1}$, making it the

fastest upcoming survey. UTMOST, which observes in a band inside GBTIM’s and whose sensitivity per steradian should eventually be comparable, could see between a couple per day and one every two weeks. We also found that CHIME Pathfinder’s single formed beam, the nearby 26 m John A. Galt Telescope, and the 46 m ARO might see a couple FRBs each year, providing sub-arcsecond localisation through VLBI.

The difficulties of estimating an all-sky rate above a single fluence value was discussed. We showed how an on-sky rate not attached to a specific survey is not only hard to predict but also hard to interpret. For that reason we estimated a rate above the true threshold for GBTIM — an SNR of 8 — which gave us $2.7_{-2.1}^{+12.4} \times 10^4 \text{ sky}^{-1} \text{ day}^{-1}$. The fluences to which GBTIM was sensitive are those above the curve $0.17\sqrt{(\tau/\text{ms})} \text{ Jy ms}$ for pulse widths between 1-100 ms. To test the agreement between this rate and those found by other surveys, we scaled based only on thermal sensitivity. If we extrapolate from this daily rate to a survey with the sensitivity of HTRU, we find $6.4_{-5.0}^{+29.5} \times 10^3 \text{ sky}^{-1} \text{ day}^{-1}$, which is consistent with (Champion et al., 2015a).

We also investigated the flux distribution index, γ , and found that steep distributions with $\gamma > 2.2$ are ruled out.

Chapter 5

Pulse Microstructure

5.1 Chapter Overview

5.2 Introduction

Within a decade of the discovery of pulsar BXX+XX it had become clear that there was great variation between individual pulses. Each pulsar's folded and integrated profile is highly reproducible and specific to that pulsar, however the pulses of which they are comprised are diverse in a multitude of ways (Lyne & Graham-Smith, 1998). Variation of polarization fraction and mode, intensity fluctuations of sub-pulses, and variable arrival times are examples of the pulse-to-pulse dynamics. Nulling and pulse drifting are also common, and still these ostensibly stochastic phenomena result in recognizable folded profiles.

On the shortest timescales microstructure appears in a number of pulsars (?Lange et al., 1998). This usually involves intensity variation on sub-millisecond timescales, and can exhibit periodic oscillatory fluctuations, and broadband features. **DESCRIBE IN MORE DETAIL** Although the micropulses have been seen in a number of slow pulsars at several different frequencies, there is no agreed upon explanation for their origin in the

magnetosphere. **INSERT EXPLANATION OF CURRENT THEORIES HERE**

5.3 Theory and Implementation

5.4 B0329+54 Individual Pulses

5.4.1 Observations

The data for our B0329+54 single-pulse analysis were taken at the Algonquin Radio Observatory (ARO). The refurbished 46 m antenna was mounted with a 400-800 MHz CHIME four-leaf clover feed. We attached to it a custom back-end made from CHIME hardware and software that can write voltage data to disk with ~ 390 kHz spectral resolution and $2.56 \mu\text{s}$ temporal resolution, which we refer to as “baseband”. Though the data is channelized with a polyphase filter bank (PFB), this process is invertible and we are able to de-channelize in order to coherently dedisperse.

We observed the pulsar for roughly XX hours on 1 August 2014, for more than 10^4 pulses.

5.4.2 Data analysis

We use a VLBI pulsar analysis code-base called `scintellometry`, which was built for correlating baseband data from different telescopes with disparate data formats. Since it deals primarily with voltage data, it is able to coherently dedisperse.

5.4.3 First coherent light

Although the majority of the back-end was written within a couple of months, the beam-former required substantial on-sky testing and subsequent debugging. One important debugging tool came from utilizing the equivalence of the summed-and-squared high-

cadence data that was produced by the beamformer with the full N^2 integrated data. This is true because the correlation step does not erase any fundamental information about the electric field. The latter is nominally taken with ~ 21 second time samples for 32,896 correlation products coming from 256 feeds. The former is a sum over the feeds which can be integrated in time arbitrarily after squaring. Ignoring the time rebinning for a moment, we can write the squared formed beam as,

$$X_{\text{BF}} X_{\text{BF}}^* = (w_1 x_1 + w_2 x_2 + \dots + w_N x_N)(w_1 x_1 + w_2 x_2 + \dots + w_N x_N)^* \quad (5.1)$$

$$= |w_1|^2 |x_1|^2 + \dots + |w_N|^2 |x_N|^2 + \dots + w_1 w_2^* x_1 x_2^* + w_2 w_1^* x_2 x_1^* + \dots, \quad (5.2)$$

where, as before, w_n are the complex weights applied in the beamformer and x_n is a voltage stream from antenna n . This can be rewritten as the sum of the auto correlations and twice the real part of the recorded cross-correlations.

$$X_{\text{BF}} X_{\text{BF}}^* = \sum_{n \leq N} |w_n|^2 V_{n,n} + 2 \sum_{\substack{n,m \leq N \\ n < m}} \Re e\{W_{n,m} V_{n,m}\} \quad (5.3)$$

In this equation we have let $W_{n,m} \equiv w_n w_m^*$. Since the correlation matrix is Hermitian, its top and bottom triangles are redundant and one needs only to record $\frac{1}{2}N(N+1)$ of the N^2 pairwise products. If we wrote all pairwise correlations, we would simply need to sum the correlation matrix after applying the relevant weights, i.e. summing after the Hadamard product, $\mathbf{W} \circ \mathbf{V}$. This is identical to Eq. 5.3 if both matrices are Hermitian.

Using the equivalence we have just described, one can compare the output of the

beamformer to the N^2 visibilities after applying complex weights and summing the correlations. This is effectively off-line beamforming, though the cadence is too slow for the science goals of the real back-end, namely studying the time-variable sky. As a first test, we would form a stationary beam with only two feeds and let a bright point-source like Cas A drift through, producing a fringe pattern. We would then take the corresponding Cas A transit from the correlated “cosmology” acquisition, using Eq. 5.3 and giving only non-zero weights to the two relevant feeds, and check if the two fringe patterns were identical. We carried out a series of tests of escalating complexity, for example including more feeds in the sum, updating phases in real-time in order to track sources, and deliberately switching the weights with their conjugate to see if the fringe direction changed. Through these tests several bugs were discovered, including spherical trigonometry errors in the phase calculations and a disagreement between one piece of code’s definition of *LST*.

The final hurdle was more fundamental to CHIME’s architecture, though in principle it should not affect the cosmology experiment. It was found through early pulsar observations that the beamformer was only summing coherently when the instrumental phases that are removed in the FPGAs are solved for with the lower-triangle of the correlation matrix. In other words, instrumental phases were not properly removed in the correlator unless they were applied as $e^{+i\phi_{gn}}$ instead of $e^{-i\phi_{gn}}$, as one would expect. The perplexing thing was that in two years of analyzing

the visibilities output by the correlator, nobody noticed a error in the sign-convention. And indeed, when we started to look at the phase of the raw visibilities, we found the argument of an east-west baseline increases with time, which is what one expects from an upper-triangle correlator. This apparent paradox was solved by discovering *two* sign errors, one in the F-engine and one in the X-engine, that effectively cancel each other out, but only if both are applied.

Our digitizers sample at 800 MHz, taking advantage of the observing band between

400-800 MHz being in the second Nyquist zone . However, when we channelize the incoming time-stream data in the FPGAs, the complex conjugation associated with the aliased second Nyquist zone was not considered during the Fourier transform. Therefore the channelized voltages leave the F-engine with an opposite sign in the exponential. When they are correlated in the X-engine it is also done in reverse order as,

$$V_{n,m} = x_n^* x_m, \quad (5.4)$$

as opposed to the upper-triangle correlation described by Klages et al. (2015),

$$V_{n,m} = x_n x_m^*. \quad (5.5)$$

The second sign convention error does not affect the beamformed output, since that data stream is never correlated. We therefore needed to account for this for the back-end to work. An example of an early verification of the beamformer’s sign convention and the first successful tracking observation is shown in Fig. 5.4.3. The collaboration has decided to keep these sign conventions as is and make note of it going forward, rather than re-write any low-level software.

5.5 FRB VLBI search

In 1967 Canada achieved an historic feat by doing the first ever successful VLBI observation. The fringes were obtained between DRAO and ARO, with a baseline of 3,074 km (Broten et al., 1967). This result was given a “Milestone” award from The Institute of Electrical and Electronics Engineers (IEEE), which was also awarded for the inception of the Internet, transmission of transatlantic radio signals, and the discovery of Maxwell’s equations (IEE, ????). We have attempted to recreate the same VLBI baseline, but instead of using the considerable spatial resolution on quasars as in 1967, we are attempting

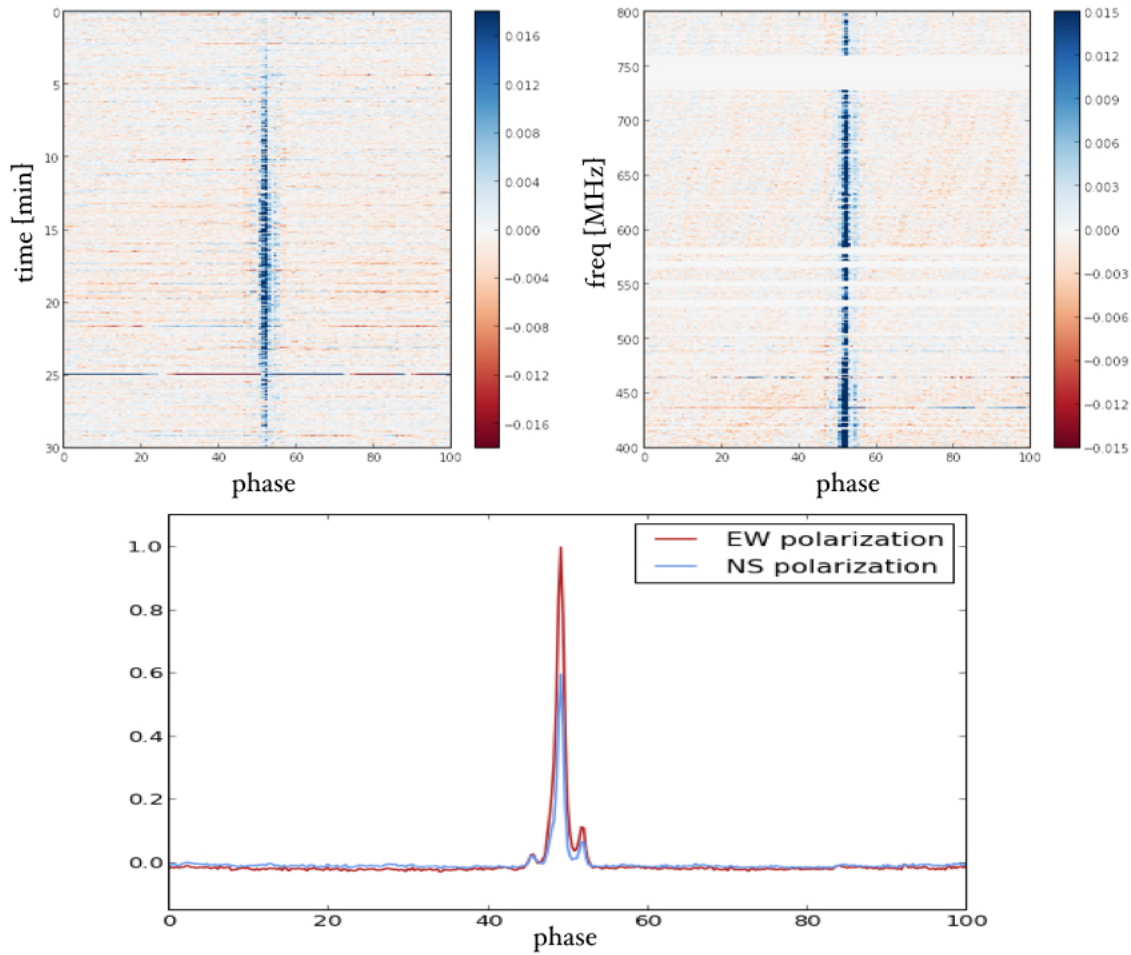


Figure 5.1: First coherent pulsar observations with CHIME. This brief observation of B0329+54 provided us with an idea of the instrument’s sensitivity and polarization response. Perhaps more significantly, it taught us that that our X-engine is a lower-triangle correlator, rather than upper-triangle like we thought, and that our F-engine *also* conjugates with the opposite sign. *top left:* waterfall plot of the pulsar’s Stokes I profile over the ~ 30 minutes when the source enters then exits our beam. *top right:* frequency vs. phase Stokes I, integrated over roughly 15 minutes. *bottom:* time- and frequency-averaged pulse profile for the two polarizations autocorrelations. The difference between the east-west and north-south beams give an estimate for Stokes Q, which includes both intrinsic polarization ($\sim 10\%$ for this source) and instrumental leakage.

to localize FRBs.

5.5.1 Motivation

The CHIME Pathfinder is meant to have only one synthetic beam. Its purpose is primarily to act as a test-bed for the more powerful pulsar and FRB back-ends that will be attached to the full four-cylinder CHIME. However since the Pathfinder is on sky at all times and the beamformer we have built does not interrupt the ongoing cosmology acquisition, we decided to build a preliminary FRB search. We also have as many as three other telescopes onto which we can mount CHIME feeds and observe in our band: the Algonquin Radio Observatory (ARO), the John A. Galt 26m, and the Green Bank 140ft telescope. This would allow for the first ever VLBI detection of an FRB.

This is interesting for a few reasons. From a development standpoint it allows us to understand better various stages of the CHIME-FRB pipeline, including the rate of RFI false-positives, our algorithm's search efficiency, and specs on the regularity and precision of instrumental gain removal. It will also give us a good sense of how the real CHIME beams behave on the sky. Perhaps most interestingly, we could reasonably expect to see a burst after several months of observing, hopefully in coincidence with the telescopes previously mentioned. We could therefore not only detect an FRB with sub-arcsecond resolution, but also would the first source in our band, at 400-800 MHz, including full polarization information. While searching for fast radio bursts, we could also find RRATs and new slow pulsars, since a significant fraction of the Galaxy transits each day.

5.5.2 Implementation

We have had a working beamforming back-end on the CHIME Pathfinder since October 2015. It has been used primarily for short tracking pulsar observations, but had stability issues on timescales of \sim days, meaning we could not run it for long periods without interfering with the regular cosmology acquisition. However in the past several months a number of new features were added that allow not only long-term beamforming captures, but also transient searching.

A real-time, multithreaded acquisition code that takes in the VDIF packets coming out of the X-engine, and rearranges them to either be written to disk or search for FRBs¹. Attached to this packet reader was a tree-dedispersion search code, some of which had been used before on Green Bank 100m data and a real-time ARO search². The CHIME acquisition software `kotekan` was altered in a number of ways, fixing the long-term stability issues in the beamforming kernel. These systems were synthesized into a real-time transient search back-end that has been on sky since May 2016. It is outlined in Fig. 5.5.2 on page 95.

Since CHIME is a transit telescope with a long north-south beam, our formed beam is effectively confined to the meridian. This means we must choose an optimal declination on which to park the beam. As a sanity check, we spent ~ 10 days pointed at the declination of pulsar B0329+54, which is the brightest switching source in the northern sky in our band. It is dispersed with $26.833 \text{ pc cm}^{-3}$ and its individual pulses are bright enough to detect, meaning our tree-dedispersion algorithm ought to find its individual pulses. During the ten or so minutes that the source is in our beam each day, the algorithm looks at time blocks of 100 seconds, searches for DMs between 10-2000 pc cm^{-3} with widths between 1-100 ms, and looks for peaks above 8σ . If it finds something it “triggers” and writes out an image file containing the peak in DM / arrival time space, a dedispersed waterfall plot, a dedispersed pulse profile, and a fluence frequency spectrum. An example of the B0329+54 is shown in Fig.???. It also writes `numpy` arrays containing the squared and summed intensity data. It then moves on to the next block of 100 seconds, overlapping with the previous one by 18 seconds.

5.5.3 Results

As we discuss in chapter 4, there is a large uncertainty in the FRB rate between 400-800 MHz. There is even greater uncertainty in the expected rate for a telescope like

¹https://github.com/kmsmith137/ch_vdif_assembler

²https://github.com/kiyo-masui/burst_search

the CHIME Pathfinder. This is because at this time all FRBs have been detected with large-collecting area, highly sensitive single-dish telescopes (GBT, Parkes, and Arecibo). Therefore in order to extrapolate the rate estimates on to the Pathfinder, which does not have much collecting area and whose beam is quite large, one needs to know the underlying flux distribution. As we will show in Eq. 4.11, the rate depends on the product of the telescope's field-of-view (FoV) and a thermal sensitivity term. This scales $\propto A^{-1}A^\gamma$, where A is collecting area and γ is the FRB flux distribution's power-law index, which is $3/2$ if FRBs are non-cosmological and Euclidean. If $\gamma < 1$, as is expected in the cosmological FRB scenario, then small telescopes are actually advantageous over large single-pixel telescopes since the beamsize becomes more important.

With a dish like the Pathfinder the rate is roughly 10 times higher if $\gamma \approx 0.8$ (cosmological scenario) compared to the Euclidean scenario. This is because its relatively low sensitivity per steradian requires there be large numbers of very bright bursts, which one gets from a flat distribution.

5.6 Conclusion

Acknowledgements

We thank Andre Recnik

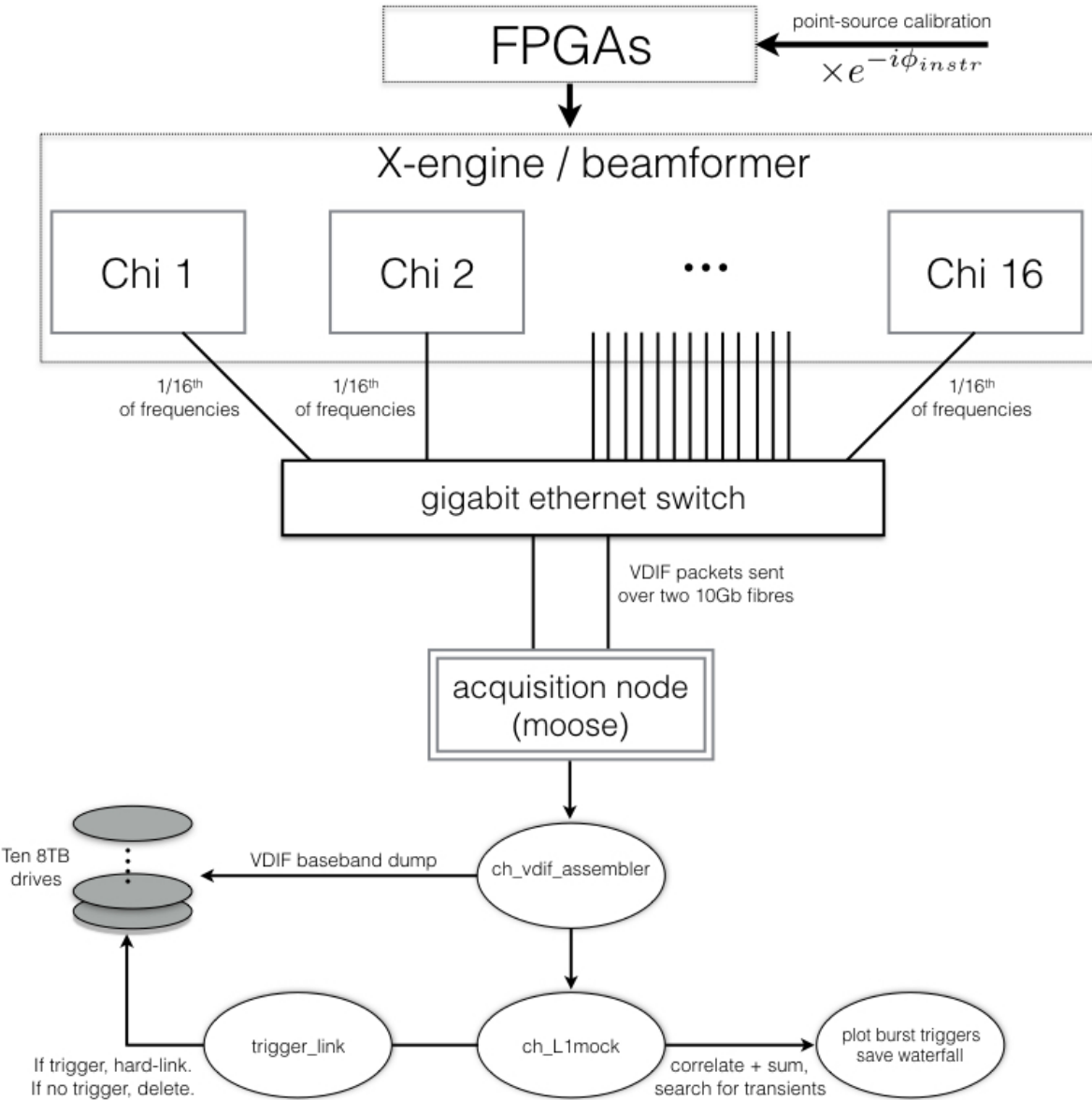


Figure 5.2: Block diagram of the beamforming back-end on CHIME Pathfinder. A calibration solution is obtained from a bright point-source transit, the phases of which are fed into the FPGAs where they are applied as a digital gain. All antenna signals are then sent the *X*-engine, comprised of 16 GPU nodes. Each node applies geometric phases then sums the voltage stream across all antennas with the same polarization. The two resultant beams are then sent to our acquisition machine `moose` as VDIF packets, where a multi-threaded capture code, `ch_vdif_assembler`. At this point the baseband data are either written to disk as scrambled baseband VDIF, or they are reorganized in time and frequency. The ordered data are searched for FRBs after squaring and integrating to \sim millisecond cadence using a tree-dedispersion algorithm. If there is a trigger, then the corresponding baseband data is hard-linked. Old files that haven't been hard-linked are deleted periodically.

Chapter 6

Conclusions and Outlook

Bibliography

????, IEEE Milestone award, [Bandura, K. e. a. 2014, in Society of Photo-Optical Instrumentation Engineers \(SPIE\) Conference Series, Vol. 9145, Society of Photo-Optical Instrumentation Engineers \(SPIE\) Conference Series, 22](http://ethw.org/Milestones>List_of_IEEE_Milestones, accessed: 2016-06-13</p></div><div data-bbox=)

Barrau, A., Rovelli, C., & Vidotto, F. 2014, Phys. Rev. D, 90, 127503

Battye, R. A., Davies, R. D., & Weller, J. 2004, MNRAS, 355, 1339

Becker, W., Kramer, M., Jessner, A., et al. 2006, ApJ, 645, 1421

Bower, G. C., Deller, A., Demorest, P., et al. 2014, ApJ, 780, L2

Brotén, N. W., Locke, J. L., Legg, T. H., McLeish, C. W., & Richards, R. S. 1967, Nature, 215, 38

Burke, B. F., & Graham-Smith, F. 2014, An Introduction to Radio Astronomy

Burke-Spolaor, S., & Bannister, K. W. 2014a, ApJ, 792, 19

—. 2014b, ApJ, 792, 19

Caleb, M., Flynn, C., Bailes, M., et al. 2016a, MNRAS, 458, 708

—. 2016b, MNRAS, 458, 718

- . 2016c, ArXiv e-prints 1601.02444, arXiv:1601.02444
- Champion, D. J., Petroff, E., Kramer, M., et al. 2015a, ArXiv e-prints 1511.07746, arXiv:1511.07746
- . 2015b, ArXiv e-prints, arXiv:1511.07746
- Chang, T.-C., Pen, U.-L., Bandura, K., & Peterson, J. B. 2010, Nature, 466, 463
- Chang, T.-C., Pen, U.-L., Peterson, J. B., & McDonald, P. 2008, Physical Review Letters, 100, 091303
- Connor, L., Lin, H.-H., Masui, K., et al. 2016a, MNRAS, 460, 1054
- . 2016b, ArXiv e-prints, arXiv:1602.07292
- Connor, L., Pen, U.-L., & Oppermann, N. 2016c, MNRAS, 458, L89
- . 2016d, MNRAS, 458, L89
- . 2016e, MNRAS, arXiv:1601.04051
- Connor, L., Sievers, J., & Pen, U.-L. 2015, ArXiv e-prints, arXiv:1505.05535
- . 2016f, MNRAS, 458, L19
- Cordes, J. M., Bhat, N. D. R., Hankins, T. H., McLaughlin, M. A., & Kern, J. 2004, ApJ, 612, 375
- Cordes, J. M., & Wasserman, I. 2015, ArXiv e-prints 1501.00753, arXiv:1501.00753
- Cordes, J. M., Freire, P. C. C., Lorimer, D. R., et al. 2006, ApJ, 637, 446
- Denman, N., Amiri, M., Bandura, K., et al. 2015, ArXiv e-prints, arXiv:1503.06202
- Dennett-Thorpe, J., & de Bruyn, A. G. 2002, Nature, 415, 57

- Eisenstein, D. J., Zehavi, I., Hogg, D. W., et al. 2005, ApJ, 633, 560
- Falcke, H., & Rezzolla, L. 2014, A&A, 562, A137
- Furlanetto, S. R., Oh, S. P., & Briggs, F. H. 2006, Phys. Rep., 433, 181
- Haslam, C. G. T., Salter, C. J., Stoffel, H., & Wilson, W. E. 1982, A&AS, 47, 1
- Hippke, M., Domainko, W. F., & Learned, J. G. 2015, ArXiv e-prints 1503.05245, arXiv:1503.05245
- Kashiyama, K., Ioka, K., & Mészáros, P. 2013, ApJ, 776, L39
- Katz, J. I. 2015, ArXiv e-prints 1505.06220, arXiv:1505.06220
- Keane, E. F., Kramer, M., Lyne, A. G., Stappers, B. W., & McLaughlin, M. A. 2011, MNRAS, 415, 3065
- Keane, E. F., & Petroff, E. 2015, MNRAS, 447, 2852
- Keane, E. F., Stappers, B. W., Kramer, M., & Lyne, A. G. 2012, MNRAS, 425, L71
- Keane, E. F., Johnston, S., Bhandari, S., et al. 2016a, Nature, 530, 453
- . 2016b, Nature, 530, 453
- Keith, M. J., Jameson, A., van Straten, W., et al. 2010a, MNRAS, 409, 619
- . 2010b, MNRAS, 409, 619
- Klages, P., Bandura, K., Denman, N., et al. 2015, ArXiv e-prints, arXiv:1503.06203
- Kulkarni, S. R., Ofek, E. O., & Neill, J. D. 2015, ArXiv e-prints 1511.09137, arXiv:1511.09137
- Kulkarni, S. R., Ofek, E. O., Neill, J. D., Zheng, Z., & Juric, M. 2014, ApJ, 797, 70

- Lange, C., Kramer, M., Wielebinski, R., & Jessner, A. 1998, A&A, 332, 111
- Law, C. J., Bower, G. C., Burke-Spolaor, S., et al. 2015, ApJ, 807, 16
- Liu, A., & Tegmark, M. 2011, Phys. Rev. D, 83, 103006
- Loeb, A., Shvartzvald, Y., & Maoz, D. 2014, MNRAS, 439, L46
- Lorimer, D. R., Bailes, M., McLaughlin, M. A., Narkevic, D. J., & Crawford, F. 2007a, Science, 318, 777
- . 2007b, Science, 318, 777
- Luan, J., & Goldreich, P. 2014, ApJ, 785, L26
- Lyne, A. G., & Graham-Smith, F. 1998, Pulsar astronomy
- Lyubarsky, Y. 2014, MNRAS, 442, L9
- Macquart, J.-P., & Johnston, S. 2015, MNRAS, 451, 3278
- Maoz, D., Loeb, A., Shvartzvald, Y., et al. 2015, ArXiv e-prints 1507.01002, arXiv:1507.01002
- Masui, K., Lin, H.-H., Sievers, J., et al. 2015a, ArXiv e-prints, arXiv:1512.00529
- . 2015b, Nature, 528, 523
- . 2015c, Nature, 528, 523
- McQuinn, M. 2014, ApJ, 780, L33
- Mickaliger, M. B., McLaughlin, M. A., Lorimer, D. R., et al. 2012, ApJ, 760, 64
- Milotti, E. 2002, ArXiv Physics e-prints, physics/0204033
- Morales, M. F., & Wyithe, J. S. B. 2010, ARA&A, 48, 127

- Mottez, F., & Zarka, P. 2014, A&A, 569, A86
- Narayan, R. 1992, Royal Society of London Philosophical Transactions Series A, 341, 151
- Newburgh, L. B., Addison, G. E., Amiri, M., et al. 2014, in Proc. SPIE, Vol. 9145, Ground-based and Airborne Telescopes V, 91454V
- Ogasaka, Y., Murakami, T., Nishimura, J., Yoshida, A., & Fenimore, E. E. 1991, ApJ, 383, L61
- Oppermann, N., Connor, L., & Pen, U.-L. 2016, ArXiv e-prints, arXiv:1604.03909
- Oppermann, N., Junklewitz, H., Greiner, M., et al. 2015, A&A, 575, A118
- Parsons, A. R., & Backer, D. C. 2009, AJ, 138, 219
- Pen, U.-L., & Connor, L. 2015a, ArXiv e-prints 1501.01341, arXiv:1501.01341
- . 2015b, ApJ, 807, 179
- Pen, U.-L., & Levin, Y. 2014, MNRAS, 442, 3338
- Peterson, J. B., Bandura, K., & Pen, U. L. 2006, ArXiv Astrophysics e-prints, astro-ph/0606104
- Petroff, E., van Straten, W., Johnston, S., et al. 2014, ApJ, 789, L26
- Petroff, E., Bailes, M., Barr, E. D., et al. 2015a, MNRAS, 447, 246
- . 2015b, MNRAS, 447, 246
- Petroff, E., Johnston, S., Keane, E. F., et al. 2015c, MNRAS, 454, 457
- Petroff, E., Keane, E. F., Barr, E. D., et al. 2015d, MNRAS, 451, 3933
- Petroff, E., Barr, E. D., Jameson, A., et al. 2016, ArXiv e-prints, arXiv:1601.03547

- Popov, S. B., & Postnov, K. A. 2007, ArXiv e-prints, arXiv:0710.2006
- Popping, A., & Braun, R. 2008, A&A, 479, 903
- Potter, T. M., Staveley-Smith, L., Reville, B., et al. 2014, ApJ, 794, 174
- Press, W. H. 1978, Comments on Astrophysics, 7, 103
- Rane, A., Lorimer, D. R., Bates, S. D., et al. 2015, ArXiv e-prints 1505.00834, arXiv:1505.00834
- . 2016, MNRAS, 455, 2207
- Rankin, J. M., Campbell, D. B., Isaacman, R. B., & Payne, R. R. 1988, A&A, 202, 166
- Ravi, V., Shannon, R. M., & Jameson, A. 2015, ApJ, 799, L5
- Reznik, A., Bandura, K., Denman, N., et al. 2015, ArXiv e-prints, arXiv:1503.06189
- Rybicki, G. B., & Lightman, A. P. 1979, Radiative processes in astrophysics
- Sallmen, S., Backer, D. C., Hankins, T. H., Moffett, D., & Lundgren, S. 1999, ApJ, 517, 460
- Schmidt, M. 1968a, ApJ, 151, 393
- . 1968b, ApJ, 151, 393
- Scholz, P., Spitler, L. G., Hessels, J. W. T., et al. 2016, ArXiv e-prints, arXiv:1603.08880
- Seo, H.-J., & Eisenstein, D. J. 2003, ApJ, 598, 720
- Shaw, J. R., Sigurdson, K., Pen, U.-L., Stebbins, A., & Sitwell, M. 2014, ApJ, 781, 57
- Shaw, J. R., Sigurdson, K., Sitwell, M., Stebbins, A., & Pen, U.-L. 2015, Phys. Rev. D, 91, 083514

- Spitler, L. G., Cordes, J. M., Hessels, J. W. T., et al. 2014a, ApJ, 790, 101
- . 2014b, ApJ, 790, 101
- Spitler, L. G., Scholz, P., Hessels, J. W. T., et al. 2016, Nature, 531, 202
- Switzer, E. R., Masui, K. W., Bandura, K., et al. 2013, MNRAS, 434, L46
- Taylor, J. H. 1974, A&AS, 15, 367
- Taylor, M., Cinabro, D., Dilday, B., et al. 2014, ApJ, 792, 135
- Tegmark, M., & Zaldarriaga, M. 2009, Phys. Rev. D, 79, 083530
- Thompson, A. R., Moran, J. M., & Swenson, G. W. 1986, Interferometry and synthesis in radio astronomy
- Thornton, D., Stappers, B., Bailes, M., et al. 2013a, Science, 341, 53
- . 2013b, Science, 341, 53
- Totani, T. 2013, PASJ, 65, L12
- van Leeuwen, J. 2014, in The Third Hot-wiring the Transient Universe Workshop, ed. P. R. Wozniak, M. J. Graham, A. A. Mahabal, & R. Seaman, 79–79
- Vedantham, H. K., Ravi, V., Hallinan, G., & Shannon, R. 2016, ArXiv e-prints, arXiv:1606.06795
- Verheijen, M. A. W., Oosterloo, T. A., van Cappellen, W. A., et al. 2008, in American Institute of Physics Conference Series, Vol. 1035, The Evolution of Galaxies Through the Neutral Hydrogen Window, ed. R. Minchin & E. Momjian, 265–271
- Voss, R. F., & Clarke, J. 1975, Nature, 258, 317
- Wang, X., Tegmark, M., Santos, M. G., & Knox, L. 2006, ApJ, 650, 529

Williams, P. K. G., & Berger, E. 2016, ApJ, 821, L22

Xu, J., & Han, J. L. 2015, ArXiv e-prints 1504.00200, arXiv:1504.00200

Zanardo et al. 2014, ApJ, 796, 82